Spring 5-10-2017

Insights on magmatic addition beneath the mid-Atlantic Coastal Plain from crustal seismic refraction data

Thomas W. Luckie
University of New Mexico

Thomas W. Luckie

Candidate

Department of Earth & Planetary Sciences

Department

This thesis is approved and it is acceptable in quality and form for publication:

Approved by the Thesis Committee:

Dr. Lindsay Lowe Worthington, Chairperson

Dr. Brandon Schmandt

Dr. Mousumi Roy

INSIGHTS ON MAGMATIC ADDITION BENEATH THE MID-ATLANTIC COASTAL PLAIN FROM CRUSTAL SEISMIC REFRACTION DATA

by

THOMAS W. LUCKIE

BS, GEOLOGY, COLORADO STATE UNIVERSITY, 2014

THESIS

Submitted in partial fulfillment of the

requirements for the degree of

Master of Science

Earth and Planetary Sciences

University of New Mexico

Albuquerque, New Mexico

May 2017

Dedication

To Sarah,

For your love, understanding, and support.

And to my family,

For your love, guidance, and encouragement.

Thank you.

Insights on magmatic addition beneath the mid-Atlantic Coastal Plain from crustal seismic refraction data

by

Thomas W. Luckie

BS, Geology, Colorado State University, 2014

MS, Earth and Planetary Sciences, University of New Mexico, 2017

ABSTRACT

Magmatic addition can lead to intraplate crustal growth through plume-generated voluminous underplating of mafic material, particularly during early syn-rift processes. In addition, magmatism facilitates crustal growth and rift development by assisting extensional tectonic forces. Therefore, understanding the relationship between magmatism and rifting may help explain both these processes. In the summer of 2015 the GeoPRISMS Eastern North American Margin (ENAM) Community Seismic Experiment collected two margin-dip active source seismic refraction profiles in eastern North Carolina and southeastern Virginia using five onshore explosive shots on a northern profile and six on a southern profile (see figure). Analysis of these data resulted in 2-D P-wave velocity models of each onshore profile that reveal a crustal thickness between 36-43 km and a high velocity (7.0-7.3 km/s) layer between 5-11 km thick at the base of the crust. We interpret this feature as representing mafic magmatic

addition, likely equivalent to the high velocity lower crust layer previously observed offshore at the transition between rifted continental crust and oceanic crust. Additionally, we observe slightly elevated velocities throughout the crust, which we interpret as metamorphic alteration in the mid- and upper-crust in response to magmatic addition from below. This magmatic addition could be related to Jurassic-aged syn-rift magmatism along the ENAM and/or to the voluminous Central Atlantic Magmatic Province (CAMP), and suggests that rift-related ENAM magmatism may be more voluminous than previously thought.

Table of Contents

1 Introduction

Intraplate magmatism in the form of plumes and basaltic underplating, which may be episodic, in large igneous provinces is one of several processes which may lead to intraplate crustal growth and extension (Rudnick, 1995). Additionally, extensional tectonic forces alone are often not sufficient to explain how continental lithosphere ruptures to form oceanic lithosphere, with the required force to initially rift thick lithosphere estimated to be up to an order of magnitude greater than available tectonic forces (Bott et al., 1991; Buck, 2004). As more rift systems are discovered to be magmatic, a correlation between intraplate magmatism and rift development appears to emerge, as seen in the East African Rift (Thybo et al., 2000, Calais et al., 2008), the eastern Black Sea (Shillington et al., 2009), and the Eastern North American and West African conjugate margins (Holbrook & Kelemen, 1993).

Magmatic intrusions have been shown to accommodate and facilitate extension of strong continental crust due to less force being required to emplace magma than to form new faults in strong continental crust (Buck, 2004; Calais et al., 2008), suggesting the importance of magmatic addition in the lower crust in the early stages of rift initiation and development (Thybo & Artemieva, 2013). Previously, the East African Rift system has shown evidence for the ponding of magmatic material at the base of the crust (Thybo et al., 2000) attributed to magmatic underplating as well as the emplacement of rift-facilitating dikes (Calais et al., 2008), assisting extension of this young rift (Thybo & Artemieva, 2013). Many margins show signs of magmatism during pre- and early syn-

rift stages and, as more data are collected, many margins previously considered to be nonvolcanic show signs of significant magmatism and volcanism early in rifting stages.

The Eastern North American Margin (ENAM), once considered a nonvolcanic passive margin (Steckler and Watts, 1981), has shown to have a significantly large amount of offshore magmatic intrusions and underplating during early rifting stages (Holbrook & Kelemen, 1993). This offshore magmatic addition is seismically characterized as a high P-wave velocity (>7.0 km/s) layer at the base of the oceanic crust (e.g.: Holbrook et al., 1992a; Sheridan et al., 1993; Holbrook et al., 1994). Few recent crustal scale seismic surveys have been conducted onshore along the ENAM resulting in a lack of crustal scale velocity models. But evidence from reflection imaging suggests that magmatic material may be present onshore and west of the oceanic-continental transition near the base of the continental crust beneath the mid-Atlantic section of the ENAM (Pratt et al., 1988). This finding may indicate that a voluminous magmatic event occurred during early rifting stages, emplacing a magmatic layer that is now present both onshore and offshore along the ENAM. However, without crustal scale velocity information along the ENAM, the extent of potential magmatic addition beneath the early rifted segments remains unconstrained.

The breakup of Pangea and formation of the ENAM is generally characterized by two phases: Triassic extension and Jurassic rifting (Condie, 1989; Thomas, 2006). Triassic extension occurred inboard of the ENAM, forming significant basins localized at reactivated Paleozoic faults in the study area, but did not develop into rifting (Condie, 1989; Swanson, 1986; Thomas, 2006; Figure 1). These basins are filled with Triassic

sedimentary rock overlain by Jurassic volcanic rock associated with a voluminous volcanic and magmatic event during rifting. Pre-existing weaknesses facilitated this early rifting, as indicated by the reactivated thrust faults, but this Triassic axis of extension did not develop into rifting. This failed extension shifted to the east during the early Jurassic, where successful rifting occurred along the modern continental margin offshore the ENAM (Condie, 1989; Thomas, 2006). This dichotomy between failed Triassic extension and successful Jurassic rifting raises questions of why the extension axis shifted to the east rather than continue extending along its previous Triassic axis during the Jurassic.

During this transition from failed-Triassic rifting to successful Jurassic-rifting at 200 Ma, the Central Atlantic Magmatic Provence (CAMP), a large igneous province, was emplaced along the ENAM (Hames et al., 2000; Figure 2). Potential CAMP-related features include dike intrusions along the ENAM, surface volcanics filling the Triassic basins, and a wedge of Jurassic-aged volcanics and underplating offshore the ENAM (Holbrook & Kelemen, 1993; Sheridan et al., 1993; Hames et al., 2000). These magmatic features have also been observed offshore the conjugate West African Margin, and may be related to the CAMP event (Contrucci et al., 2004). However, evidence suggests that amagmatic extension occurred in the southern portion of the ENAM study area supported by a lack of Jurassic surface volcanics (Schlische, 2003). How much extension occurred because of these Triassic basins and the role of magmatism and CAMP during the pre- and early syn-rift phases remains uncertain.

Additionally, the ENAM has experienced lithospheric delamination throughout the Cenozoic, resulting in decompression melting in the upper mantle and the emplacement of Cenozoic-aged dikes to the west of the study area (Biryol et al., 2016). This leads to two possible origins of magmatism along the ENAM: either rifting, related or unrelated to CAMP, or delamination. If there are no correlations between magmatism and Triassic basins this would indicate that magmatism is possibly Jurassic in age, with magmatism facilitating the rifting of strong crust at 200 Ma by accommodating extension. Additionally, if the magmatism occurred in the Jurassic, this would suggest that the magmatic addition is associated with the voluminous Jurassic-aged CAMP event. Alternatively, no correlations between crustal structure and magmatic addition could indicate magmatism is related to Cenozoic delamination if it appears that magmatic addition did not facilitate Mesozoic extension and rifting. However, if the magmatic addition is localized beneath Triassic basins, this would suggest that magmatism along the ENAM was emplaced during Triassic extension and is unrelated to CAMP. In this case, magmatism would appear to be inconsequential in facilitating extension of the ENAM in the Triassic.

Understanding the distribution of magmatism during rift initiation and evolution as preserved in mature continental margins can help explore the connection between magmatism, extension, and intracrustal growth throughout the continental breakup cycle. The ENAM preserves evidence from the earliest phases of rift initiation and evolution, allowing researchers to determine to what extent the role of magmatism plays in influencing extensional forces to rupture continental crust and form oceanic crust.

The work presented in this thesis seeks to explore the role of magmatism in pre- and syn-rift extension along the ENAM, and to determine whether magmatism was involved during extension in the Triassic through the construction of two crustal-scale P-wave velocity models across the mid-Atlantic coastal plain. Additionally, the role of preexisting structures in relation to magmatism in facilitating extension and rifting are considered. Finally, a relationship between this magmatic addition and CAMP, as well as the potential role CAMP may have in rift initiation, is explored.

I use active source seismic refraction data collected onshore as part of the Eastern North American Margin (ENAM) Community Seismic Experiment (CSE) from the summer of 2015 (Figures 3 & 4). The ENAM CSE collected two onshore seismic profiles in eastern North Carolina and southeastern Virginia to investigate rift initiation and evolution processes. My velocity models show a high P-wave velocity (>7 km/s) layer at the base of the crust, which has never been previously observed onshore in this region, which suggests that magmatism played an important role in facilitating successful rifting along the ENAM.

2 Geologic and tectonic setting

The ENAM is composed of several terranes accreted to Laurentia in the Mesoproterozoic (Whitmeyer & Karlstrom, 2007; Schlische, 2003). Generally, the ENAM is bounded by the Piedmont physiographic province to the west, which is underlain by the Carolina and Blue Ridge Terranes, and the offshore Blake Spur Magnetic Anomaly to the east. This study focuses on the mid-Atlantic region of the ENAM, specifically eastern North Carolina and southeastern Virginia. Previous studies from the region

have also imaged the Blue Ridge Terrane (e.g., Pratt et al., 1988). Both the Blue Ridge and Carolina terranes are primarily composed of metaigneous rocks (Whitmeyer & Karlstrom, 2007; Hibbard et al., 2002).

2.1 Terrane accretion and formation of Pangea

The Blue Ridge Terrane accreted to the eastern margin of Laurentia during the middle stage of the Grenville orogenic cycle in the Mesoproterozoic (1.3-1.0 Ga; Whitmeyer & Karlstrom, 2007). This continent-continent collision and tectonic period represents the final assembly of the super-continent Rodinia (Dalziel, 1991). Late syntectonic intrusions in the Blue Ridge Terrane which occurred 1.08-1.07 Ga (Carrigan et al., 2003; Aleinikoff et al., 2000) as well as volcanism represented by metavolcanic supracrustal rocks (Carrigan et al., 2003) are observed in North Carolina. Low-grade metaigneous and metasedimentary rocks of the Carolina Terrane have a range of ages from 630 to 458 Ma (Secor et al., 1983; Hibbard et al., 2002), with the terrane accreting to the eastern margin of Laurentia ca. 450 Ma (Vick et al, 1987). The central Piedmont shear zone, a late Paleozoic ductile thrust fault, lies along the western limit of the Carolina Terrane and represents the docking of the Carolina Terrane against Laurentia (Hibbard et al., 2002). The Piedmont physiographic province is underlain by these terranes.

The breakup of Rodinia along the Iapetan margin of southeastern Laurentia occurred in multiple phases (Thomas, 2011). The oldest phase, called the Blue Ridge rift, is bounded by episodes of synrift magmatism as old as 750 Ma and synrift igneous rocks as young as 572 to 564 Ma (Aleinikoff et al., 1995; Walsh and Aleinikoff, 1999).

The transition from active-rift-margin to passive-margin is represented by a sequence of basal sandstone overlying carbonates—this sedimentary succession overlies the synrift igneous rocks, and have been dated to the beginning of Cambrian time (540 Ma) along the Blue Ridge rift (Thomas, 2011). This rifting resulted in the formation of the Iapetus Ocean and the separation of Laurentia from Rodinia by 530 Ma (Thomas, 2006).

The formation of Pangea is marked by three orogenic events (Thomas, 2006): Taconic (Ordovician to Silurian) which possibly included terrane accretion that modified the shape of the margin, Acadian (Devonian to Mississippian), and Alleghanian (Mississippian to Permian). These orogenic events concluded with the closure of the Iapetus Ocean and formation of Pangea by 325 to 260 Ma (Hatcher, 2010).

2.2 Extension and formation of the Atlantic Ocean

Grabens in central North Carolina dated to the early Jurassic are associated with the early extension of Pangea and the opening of the modern Atlantic Ocean (Thomas, 2006), with rifting initiating 200 Ma (Condie, 1989). It is important to note that the rifted Atlantic margin of North America crosses sutures associated with the formation of Pangea, and does not follow fault segments associated with the previous Iapetan rifting (Thomas, 2006). Jurassic aged volcanism, which formed a wedge of igneous rock beneath the offshore Baltimore Trough, occurred along the margin during mid- to late-stage rifting (Sheridan et al., 1993). This magmatic event, similar to events observed along other passive margins, including the conjugate West African Margin, is considered by previous studies to be the potential source for magmatic underplating observed beneath the margin offshore. As continental rifting developed into continental

drift, sediments of the Coastal Plain physiographic province collected along the ENAM forming the modern continental margin.

2.3 Magmatism and CAMP

Inboard Triassic extension along the ENAM developed into offshore Jurassic rifting along the modern continental shelf. During this transition from failed Triassic extension to successful Jurassic rifting at 200 Ma, the Central Atlantic Magmatic Provence (CAMP), a large igneous province, was emplaced along the ENAM (Hames et al., 2000; Figure 2). Jurassic rifting is associated with an offshore zone of magma-rich transitional crust offshore coincident with the East Coast Magnetic Anomaly (ECMA) (Holbrook et al., 1992a; Holbrook et al., 1992b). This magma-rich transitional crust is also observed along the conjugate West African margin (Contrucci et al., 2004). This magmatic feature is characterized by seaward dipping reflectors (SDRs) resulting from wedges of volcanic rock observed seismically in the upper crust (Holbrook & Kelemen, 1993). The ages of these volcanics vary along the margin, coinciding with the 200 Ma CAMP event in the Carolina Trough (Schlische et al., 2003), but predating CAMP in the Baltimore Canyon (Schlische et al., 2003; Blackburn et al., 2013). Seismic P-wave velocities beneath the SDRs at the base of the crust range from 7.0-7.5 km/s, and represent magmatic addition to the crust via intrusion or underplating (Holbrook & Kelemen, 1993).

2.4 Magnetic anomalies

The East Coast Magnetic Anomaly (ECMA) is a strong positive anomaly extending 2300 km along the ENAM from Blake Spur to offshore Nova Scotia, and

displays segmentation on length scales similar to segmentation observed at the Mid-Atlantic Ridge (Figure 4). This distinct magnetic high is generally assumed to mark the continent-ocean boundary and is located outboard of the thickest portions of the offshore high velocity layer (Behn & Lin, 2000). The Brunswick Magnetic Anomaly (BMA) is a magnetic low that extends from Georgia to offshore Cape Hatteras in North Carolina, and likely marks the hinge zone along the western edge of sedimentary basins along the margin (Behn & Lin, 2000; Figure 4). The northern end of the BMA terminates where it intersects the ECMA. The Blake Spur Magnetic Anomaly (BSMA) is the farthest offshore anomaly, and is a magnetic high noticeably weaker than the ECMA associated with a ridge jump at ~170 Ma (Behn & Lin, 2000; Figure 4).

2.5 Previous geophysical constraints on crustal structure

The ENAM study area has not been the subject of many recent targeted imaging either via passive or active source seismic experiments both onshore and offshore. As a result, much of what is understood about magmatism along the ENAM and the breakup of Pangea is derived from offshore data collected throughout the 1980s and 1990s. However, a single onshore experiment, the 1981 I-64 experiment, does provide some constrains on onshore crustal structure north of the study area.

Recent EarthScope's USArray Transportable Array (TA) results in eastern North America provide insights into regional crustal thickness and upper mantle properties which may influence crustal structures and magmatism. Schmandt et al. (2015) used multimode receiver function stacking with broadband data collected by EarthScope to image crustal structure beneath the US. The estimated Moho depth was found to be

~43 km beneath the Piedmont, with a landward increase in crustal thickness near the western-edge of the Piedmont (Schmandt et al., 2015). Using long-period waveform tomographic modeling, Yuan et al. (2014) found a pronounced band of slow S-wave velocities at a depth of 60 km, which correlates with the Neoproterozoic-Cambrian rift margin of the ENAM. This correlation was attributed to the preservation of rift events during the break up of Rodinia and the Appalachian orogenic event during the formation of Pangea along the margin (Yuan et al., 2014). Wagner et al. (2012) presented dominantly null SKS splitting measurements east of the Appalachians in the mid-Atlantic ENAM, which may be indicative of vertical mantle flow and weak to no anisotropy in the asthenosphere beneath the ENAM. These observations were corroborated by Long et al. (2016), who presented SKS splitting measurements from the TA along the ENAM. Null SKS arrivals were also found within the ENAM CSE, with an apparent lack of upper mantle anisotropy and vertical mantle flow. A possible source for this vertical flow is upwelling associated with volatiles transported by the Farallon slab in the mid-mantle or edge-driven convective downwelling around a lithospheric root (Long et al., 2016). Biryol et al. (2016) present evidence from tomographic P-wave velocity models from TA data which suggests the lithosphere beneath eastern North Carolina has been piecemeal delaminated throughout the Cenozoic, which would place the asthenosphere in close contact with the crust. This setting could facilitate decompression melting beneath the ENAM (Nelson, 1992; Mazza et al., 2014), leading to increased magmatism in the area during passive margin development.

The I-64 experiment (Pratt et al., 1988), consisted of an onshore seismic reflection survey imaging shallow- to deep-crustal structures across the Blue Ridge and Carolina Terranes. This study found thin (3 km thick) allocthonous crystalline rocks in the Blue Ridge Terrane, as well as autochthonous Grenville basement below the Blue Ridge at a depth of 9 km. Middle- to lower-crustal layering was observed at a 25 km depth, with strong east dipping reflections which were thought to be the Precambrian continental margin. These reflections coincide with the Moho, which varies from a depth of 55 km across the Blue Ridge, 35 km across the Carolina Terrane, and then thickens again farther east. With the use of a gravity model the researchers hypothesized that additional magmatic (i.e., granitic plutons and metaigneous rocks) along with the previously known sediments, Mesozoic basin, and one previously known granitic body must be present in the crust along this profile. Through a schematic interpretation of the seismic reflections, an intrusive and/or body of partial melt is identified beneath the Carolina Terrane and the Atlantic Coastal Plain. This magmatic body is interpreted as unbounded by upper crustal structures and the Triassic-aged Richmond basin.

Offshore along the ENAM, a ~20-25 km thick high velocity layer which coincided with the ECMA was observed in the lower crust in four separate active source experiments (Holbrook & Kelemen, 1993). One of these experiments, the 1990 offshore EDGE mid-Atlantic seismic experiment, revealed a high velocity (>7.0 km/s) bottommost layer in oceanic crust from OBS data, which was deemed to be the result of magmatic underplating related to rifting, rather than thinned continental crust (Holbrook et al.,

1992a). However, these data did not provide any evidence for underplating located under the continental crust (Holbrook et al., 1992a).

The MCS data from the EDGE experiment also imaged a northwest-dipping reflector for the first time on the mid-Atlantic margin—this reflector was assumed to be the top of a Jurassic-aged magmatic-underplated layer (Sheridan et al., 1993). A thickened crust was observed landward of this underplating layer, and was relatively thinner and horizontal seaward—this change in Moho depth was thought to represent the edge of the Grenville-aged crust to the west, juxtaposed with Jurassic-aged magmatism to the east (Sheridan et al., 1993). Through the construction of a velocity model, Holbrook et al. (1994) determined that the seaward dipping reflectors and high-velocity lower crust represent a thick igneous crust. Beneath the transitional crust, and just above the Moho, an abrupt decrease in reflectivity and increase in velocities likely represents an intrusion. With the lack of evidence of a hotspot in the central Atlantic during rifting, the study assumes that this igneous material is the product of nonplume processes, such as widespread magmatic underplating during rifting. It has been argued that rifting and plumes may be independent of each other, and that the association of CAMP and rifting of the ENAM do not necessarily indicate plume magmatism (McHone, 2000).

Other studies outside the EDGE experiment include Holbrook et al. (1992b) which examined wide-angle offshore OBS reflection data. This experiment revealed that the Moho rises from 33 km beneath the continental shelf to 20 km beneath the outer rise across a distance of 60-70 km, which represents a continental-crust to oceanic-

crust transition. The study concluded that the Moho in this area is a Jurassic feature which is the result of magmatic intrusion and underplating during the breakup of Pangea. The BA-6 seismic profile was collected offshore and to the south of the ENAM CSE along the Carolina Trough (Holbrook & Kelemen, 1993). The velocity structure of the BA-6 profile also displays a high velocity (>7.0 km/s) layer, with a Moho depth of 35 km in the west shallowing to 20 km in the east. The BMA defines the western terminus of the high velocity layer offshore, with the thickest portion of the layer coinciding with the ECMA.

3 Data

This research utilized data collected as part of the onshore portion of the Eastern North American (ENAM) Community Seismic Experiment (CSE) in the summer of 2015 (Figures 3 & 4). The ENAM CSE was funded by the NSF Geodynamic Processes at Rifting and Subducting Margins (GeoPRISMS) program as part of the Rift Initiation and Evolution (RIE) initiative.

3.1 ENAM CSE

The ENAM CSE included an onshore and offshore component. Two along dip lines (Line 1 and Line 2) were collected onshore and offshore as part of a continuous seismic line. Offshore data were collected using MCS and OBS, with offshore airgun shots recorded using 80 broadband seismometers deployed onshore along Line 1 and Line 2 during the offshore acquisition stage of the experiment, introducing an onshore-offshore component to the experiment to image the continent-ocean boundary.

Additionally, three along strike offshore seismic lines were collected along the ECMA and BSMA.

Two seismic profiles were collected onshore as part of the ENAM CSE: Line 1 and Line 2, each ~220 km long (Figures 3 & 4). Line 1 begins on the Outer Banks in northeastern North Carolina, near Kitty Hawk, and extends across the Coastal Plain and terminates west of the eastern edge of the Carolina Terrane in the Piedmont physiographic province of southeastern Virginia. Line 2 begins on the Outer Banks in east-central North Carolina, near Camp Lejeune, and extends across the Coastal Plain to Fayetteville. The sources used were 182 kg explosive charges, with five shots on Line 1 and six shots on Line 2 with an average shot spacing of 60 km. Shots were recorded using 711 Reftek-125 seismometers ('Texans') on Line 1 and 705 Texans on Line 2, with an average instrument spacing of 250 m. This experimental design and instrument spacing provided adequate imaging of the crust through crustal refractions and Moho reflections.

3.2 Onshore seismic refraction data

Multiple P-wave and S-wave (not included in this study) arrivals are visible in shot gathers from Line 1 and Line 2 of the onshore portion of the ENAM CSE (Figures 5-8 and Appendix A). The signal-to-noise ratio (S/N) decreases from west to east along each shot gather, likely due to a combination of human activity and wave action along the coast and barrier islands. The S/N decrease is abrupt, occurring at a distance of ~170 km on Line 1 and ~100 km on Line 2. This change greatly affects the visibility of phases on shot gathers from shots of the western portions of the ENAM (shots 11 and

13 on Line 1; shots 21, 22, and 23 on Line 2). However, the signal-to-noise ratio is relatively high in shot gathers from the eastern shots (shots 14, 15, 16 on Line 1; shots 24, 25, 27 on Line 2). Moving west to east along each profile, shot gathers show an apparent increasing delay in first arrivals; from ~0 seconds in the western shots (11 on Line 1, 21 on Line 2) to ~1 second in the eastern shots (16 on Line 1, 27 on Line 2). These delays are a result of the thickening of the relatively slow seismic velocities (<3.0 km/s) of the Coastal Plain sediments from west to east across each profile with shots 14, 15, and 16 on Line 1 and shots 24, 25, and 27 on Line 2 displaying a refracted phase through these sediments (P_{sed}), which was not included in this analysis.

Crustal refraction arrivals (Pg) and Moho reflection arrivals (PmP) travel times were picked on every shot gather and used in the tomographic inversion. Pg arrivals on Line 1 have a high S/N from 0 to 170 km across the profile for shots 11, 13, and 14, with the S/N decreasing abruptly at 170 km. For shots 15 and 16 on Line 1, Pg arrivals have a high S/N across the entire shot gathers. Similarly for Line 2, Pg arrivals have a high S/N from 0-100 km across the profile for shots 21, 22, 23, and 24 with an abrupt decrease at ~100 km. Shots 25 and 27 show a Pg arrival with a high S/N across the entire shot gather.

The PmP arrivals generally appear at source-to-receiver offsets greater than 80 km. Because of the low S/N in the eastern portion of the profiles, PmP arrivals are clearer on the western side of shot gathers 15 and 16 on Line 1 and 25 and 27 on Line 2. These wide-angle PmP arrivals are observed as secondary quasi-hyperbolae arrivals on all shots. The PmP phase is characterized by a reverberative wave train at both low

(1-15 Hz) and high (15-25 Hz) frequencies (Figures 9 & 10). This distinctive wave train is observed at multiple stations and appears horizontally continuous. Moho refraction arrivals (Pn) were only observed and picked for shot 11 on Line 1. For every shot gather, Pg becomes emergent where a high amplitude internal crustal reflection (Pi_1P) is observed. Several other internal crustal reflections (Pi_2P and Pi_3P) were observed, all with relatively high amplitudes. However, the amplitudes of these internal crustal reflections are generally less than that of the PmP arrivals because impedance contrasts within the crust are not as large as the contrast between the crust and the mantle. These arrivals were not included in this analysis, but could provide insight into internal crustal reflectivity and suggest that the western portion of the profiles may have a more complicated internal structure.

4 Methods

4.1 Phase identification and reciprocity

The procedure for tomographic inversion required travel time picks for first arrival crustal refraction (Pg), Moho reflection (PmP), and Moho refraction (Pn). First arrival times for each profile were manually picked using the interactive graphics program PLOTSEGY (Zihlman, 1992) after the application of a Butterworth band-pass filter with a low cut frequency of 5 Hz and a high cut frequency of 15 Hz. Picks were checked and refined using a combination of reciprocity and the 2-D seismic ray tracing and forward modeling program MacRay (Luetgert, 1992). The final collection of picks included 1999 Pg arrivals, 258 PmP arrivals, and 7 Pn arrivals for Line 1 and 1685 Pg arrivals, 296

PmP arrivals, and 0 Pn arrivals for Line 2. The total number of picked arrivals was 2264 for Line 1 and 1981 for Line 2.

4.2 Starting velocity model

The starting velocity model for the initial inversion was constructed from a series of 1-D velocity models from each shot derived using the menu-driven 1-D seismic travel-time calculator MacR1D (Luetgert, 1992). Using the calculated velocities and interface depths along each profile from MacR1D, a 2-D two-layer starting model was created for each profile (Figures 11 & 12). The structure of the starting models will affect the speed of convergence during iterative inversions, but it should not affect the final velocity structures if the regularization parameters in each inversion do not bias the solution (e.g., Toomey et al., 1994; Van Avendonk et al., 2016). Smoothing parameters were tested to assess the trade-off between data misfit and model roughness, largely favoring a minimum structure model.

4.3 Tomographic inversion procedure

Fixed pick uncertainties were used based on source receiver offsets: 50 ms for offsets <10 km, 75 ms for offsets between 10 km to 25 km, 100 ms for offsets between 25 km to 50 km, and 125 ms for offsets >50 km. To invert the travel times for seismic velocity, the iterative tomographic method of Van Avendonk et al. (2004) was utilized. Ray tracing and ray bending were performed on the starting model in order to obtain a set of calculated travel times during each iteration. Ray tracing followed the shortest path method of Moser (1991), in which a number of randomly dispersed nodes are placed in 2-D space. The ray trace will follow from node to node in a straight line, so

that the travel time to the receiver will be minimized. This method creates a ray path with sharp angles in areas, but minimizing the gradient in travel time with ray bending reduces this affect (Van Avendonk et al., 2004).

Residual travel times (δt_i) were determined by subtracting the observed travel times from the calculated travel times. This δt_i can be written as a linear combination of small deviations in slowness (δu; i.e., the reciprocal of seismic velocity) and depth to boundaries (δr_k) for each layer k. This can be expressed as:

$$d = G\ \delta m$$

where d contains a vector of residual travel times, G is the Frechet matrix, and δm is a vector of the small deviation of the model. A least squares inversion was then applied to obtain a new set of model parameters for the next iteration of inversion (Van Avendonk et al., 2004). An approximate least squares estimate $\delta\hat{m}$ is found using a sparse matrix solver, with $\delta\hat{m}$ used to update δm in the inversion and to evaluate the data fit of the inversion (χ^2) by comparing picked and calculated travel times by approximating χ^2 with:

$$\chi^2 \approx \frac{1}{M}\left\|C_d^{-1/2}(G\delta\hat{m} - d)\right\|^2$$

where M is the length of d and C_d is a diagonal matrix with data variances. The model perturbations δm required to fit the data should become reasonably small after a series of iterations.

Iterations involving ray tracing and 2-D inversions to solve for seismic velocity were conducted until the root mean squared (RMS) misfit was decreased to 145 ms

with a nominalized χ^2 of 1.0 for Line 1, and a model RMS misfit of 144 ms with a nominalized χ^2 of 1.0 for Line 2. Using this model, a third layer at the top of the crust with a uniform starting velocity of 2.5 km/s, a thickness of 5 km, and pinching out at 90 km was added to simulate the sediments of the Coastal Plain and to further reduce misfits of the models. This three-layer model was then used for a final set of iterations of ray tracing and inversions, reducing the final velocity model RMS misfit to 106 ms (an improvement of 39 ms over the two layer model) with a normalized χ^2 of 1.0 for Line 1 (Figure 13), and a model RMS misfit of 114 ms (an improvement of 30 ms over the two layer model) with a normalized χ^2 of 1.0 for Line 2 (Figure 15).

4.4 Resolution

An estimate of the model resolution was derived from the generalized inversion that produced the final velocity model, with nondimensional resolution values ranging from not resolved (value of 0) to fully resolved (value of 1); resolution values greater than 0.5 are considered adequately resolved (e.g., Van Avendonk, 2004). A total of eight model anomalies of different sizes were tested for each line to determine how well the final velocity models could resolve seismic structures at different scales (Figures 17 & 18 and Appendix B). Ray density of the models were calculated using the derivative weight sum (DWS), which is the summation of the Frechet matrix from the tomographic inversion procedure (Toomey & Foulger, 1989; Figures 19 & 20).

5 Results

The final 2-D seismic velocity models for Line 1 and Line 2 lie entirely within the Piedmont and Coastal Plain Provinces, crossing several Triassic aged basins in the upper crust. These basins are located within the Coastal Plain Province.

5.1 Line 1 velocity model

The final 2-D seismic velocity model for Line 1 (Figures 13 & 14) shows a smooth velocity gradient through the crust: From 6.1 km/s in the upper crust to 7.1 km/s in the lower crust. A pocket of velocities <6.0 km/s is observed in the upper 3 km of the crust around 100 km in the model, which correlates with the location of an intersecting Triassic basin. Additionally, the coastal plain sediment layer appears around 110 km in the model, thickening towards the east to a maximum thickness of 2.9 km at the coast. Velocities within the sediment layer are ~2.5 km/s. At the base of the crust, a high velocity (>7.0 km/s) layer is present, varying in thickness from ~5.0-7.0 km. Velocities in this layer range from 7.0-7.1 km/s, and the layer thickens slightly to the east. The Moho across the profile is relatively flat, appearing at a depth of ~36 km in the west and ~37 km in the east where PmP and Pn ray coverage is available. The upper mantle shows a velocity of 7.9 km/s where Pn coverage is available.

5.2 Line 1 resolution

A seismic structure 10 km long (horizontally) and 5 km thick (vertically) can be resolved (i.e., the resolution is >0.5) in the upper crust (0-7 km in depth) across the entire profile, and can be resolved in the mid-crust (to a depth of 25 km) from 50 km to 130 km (Figure 17 top). A seismic structure 20 km by 10 km can be resolved in the

upper crust (0-15 km) across the entire profile, and can be resolved in the mid- to lower crust (to a depth of 30 km) from 50 km to 150 km (Figure 17 middle). A significant reduction in resolution is present from 90 km to 160 km in the lower and mid crust where ray coverage is low. A seismic structure of 30 km by 15 km can be resolved across the entire model, except for the reduced resolution from 90 km to 120 km in the lower crust, and from 120 km to 160 km in the lower to mid crust where ray coverage is lacking (Figure 17 bottom). The Moho is well resolved from 50 km to 90 km and from 120 km to 160 km. The ray coverage DWS shows ray density is the greatest in the upper crust (0-10 km depth), with greater coverage in the western portion of the model (0-120 km across the profile). The Moho is well sampled in reflection patches from 50 km to 90 km, and 120 km to 160 km.

5.3 Line 2 velocity model

The final 2-D seismic velocity model for Line 2 (Figures 15 & 16) also shows a smooth velocity gradient through the crust. Velocities in the profile increase from 6.0 km/s in the upper crust to 7.3 km/s in the lower crust. Pockets of velocities <6.0 km/s are observed in the upper 5 km in the crust around 50 and 100 km in the model, which correlates with the location of two intersecting Triassic basins. Additionally, the coastal plain sediment layer appears around 120 km in the model, thickening towards the east to a maximum thickness of 1.2 km at the coast, with velocities within the sediment layer of ~2.5 km/s. Similar to Line 1, Line 2 shows a high velocity (>7.0 km/s) layer at the base of the crust, which varies in thickness from ~7.0-11.0 km. Velocities in this layer range from 7.0-7.3 km/s, and the layer thickens towards the east. The high velocity

layer observed in Line 2 is generally both faster and thicker than the layer observed in Line 1. The Moho dips to the east across the profile, from 37 km in the west to 43 km in the east. The dip of the Moho steepens where the highest velocities (>7.2 km/s) are observed. The high velocity layer in Line 2 reaches its maximum thickness where there is a change in slope of the Moho. Velocities >7.2 km/s are observed where the crust thickens noticeably. Upper mantle velocities do not vary due to the lack of constraints from Pn arrivals.

5.4 Line 2 resolution

A seismic structure 10 km long (horizontally) and 5 km thick (vertically) can be resolved (i.e., the resolution is >0.5) in the upper crust (0-10 km in depth) across the entire profile, and can be resolved in the mid-crust (to a depth of 20 km) from 100 km to 150 km (Figure 18 top). A seismic structure 20 km by 10 km can be resolved in the upper crust (0-15 km) across the entire profile, and can be resolved in the mid- to lower crust (to a depth of 30 km) from 90 km to 150 km (Figure 18 middle). A seismic structure of 30 km by 15 km can be resolved across the entire model, except for the reduced resolution from 50 km to 70 km in the mid to lower crust where ray coverage is lacking (Figure 18 bottom). The Moho is well resolved from 60 km to 120 km and from 140 km to 180 km. The ray coverage DWS shows ray density is the greatest in the upper crust (0-5 km depth; Figure 20). The Moho is well sampled in reflection patches from 70 km to 80 km, 100 km to 130 km, and 150 km to 170 km.

5.5 1-D velocity profiles

Three 1-D velocity profiles were extracted from Line 1 and Line 2 at 50 km, 100 km, and 150 km distances across the final velocity models to more directly compare velocity structure across and between the transects (Figures 21-23). These profiles were also plotted in comparison to average velocities of continental rifts and extended continental crust from Christensen & Mooney (1995). For Line 1 (Figure 21), the three extracted profiles contain relatively similar velocities above 30 km depth, and all three show higher velocities than the averages from the literature. Variations above 10 km are likely due to the profiles sampling Triassic basins and/or the Coastal Plain sediments. Below 30 km the profiles match the average velocities of continental rifts. However, the observed Moho depth of 36-27 km is much shallower than the average Moho depth of 40 km.

Similarly, for Line 2 (Figure 22), the profiles display higher velocities than average for extended continental crust above 30 km, and start to converge with the average at 30 km depth. Again, the Moho is generally shallower (~38 km) than the average of 40 km. Velocities in the crust generally increase from west to east by approximately 0.2 km/s in Line 2 (Figure 23), which contrasts the similar velocities observed across the profile below 10 km depth in Line 1. The fairly uniform velocities from profiles in Line 1 are most similar to the 100 km profile in Line 2, which is taken from the middle of the model. Line 1 profiles show a Moho depth around 37 km depth in the 50 km and 150 km profile, and a depth of around 38 km in the 100 km profile. This

rolling Moho in Line 1 differs from the gradually dipping Moho in Line 2. The Moho gradually deepens from 50 km to 150 km along the profile in Line 2.

6 Discussion

6.1 High velocity layer as magmatic addition

Upper crustal Triassic basins appear to have no influence on the extent of the high velocity layer lower crustal layer observed on both ENAM seismic profiles (Figures 13 & 15). The high velocity layer appears continuous along dip where ray coverage is available in the models, and there is evidence that this layer may extend as far north as central Virginia (Pratt et al., 1988). High velocity lower crust previously observed offshore along the ENAM and along the conjugate West African Margin exhibit similar velocities to the onshore high velocity layer, suggesting that these layers have similar compositions and may have formed during pre- or early-rift processes.

High velocities (6.8-7.5 km/s) in the lower crust near rift axes are indicative of mafic or ultramafic rock (i.e., high in Mg) derived from magmatic addition through intrusion or underplating (Sheridan et al., 1993; Holbrook et al., 1994; Shillington et al., 2009). The elevated velocity structure along the ENAM coincides with average measured P-wave velocities for mafic igneous rocks (Christensen & Mooney, 1995), with upper crustal (>15 km) velocities coinciding with basaltic velocities and lower crustal (<30 km) velocities coinciding with gabbroic velocities (Christensen & Mooney, 1995; Figures 21 & 22). Interestingly, velocities observed throughout the crust in the ENAM profiles are higher than expected for continental rifts and extended continental crust (Christensen & Mooney, 1995; Figures 21 & 22). Lower crust velocities

correspond to global averages of mafic rocks, supporting the interpretation that this high velocity layer is derived from a magmatic layer of mafic composition. The elevated velocities throughout the rest of the crust, may indicate mid- to upper-crustal magmatic intrusion.

Upper crustal velocities along Lines 1 and 2 are similar to velocities associated with the observed offshore SDRs (Holbrook et al., 1994). This similarity may indicate magmatic addition or alteration to the upper crust and explains the elevated crustal velocities (6.0-7.0 km/s) above the high velocity layer. Thus, the onshore region could be igneous rich, rifted/extended continental crust with significant magmatic addition and/or intrusions throughout. Numerous Mesozoic dikes have been mapped immediately to the west of the study area within the Piedmont province (Figure 3). However, there are no mapped dikes in the Coastal Plain, suggesting either that magmatism did not reach the surface in this region, or that surface magmatism is buried by coastal plain sediments. Evidence from gravity modeling carried out by Pratt et al. (1988) suggests the presence of at least one previously unknown buried mafic dike beneath the Coastal Plain north of the ENAM study area. The simple geographic relationship with onshore Mesozoic diking and offshore Mesozoic magmatism suggests that the high velocity lower crust beneath the coastal plan is likely Mesozoic in age and was emplaced around the time of Mesozoic diking, extension, and rifting. Further study of the internal reflectivity along each of the profiles could provide insight into these potential internal crustal structures.

The high velocity layer does not appear uniform along strike when comparing both models: Line 1 shows a high velocity layer of relatively uniform thickness and velocity along dip (Figure 13), while Line 2 shows a high velocity layer with varying thickness and velocities along dip (Figure 15). Variations in mantle water content and/or temperature during magmatic emplacement can produce gradual changes in properties of the magmatic addition to the crust (Holbrook et al., 2001; Robinson et al., 2001; Shillington et al., 2009), with higher temperatures and/or water content resulting in elevated velocities and/or the emplacement of additional magmatic material. Variations from a thermal and/or compositional anomaly in the upper mantle could explain the differences observed in both the high velocity layer thickness and differing lower crustal velocities along strike, with Line 2 being hotter and/or wetter than Line 1.

The reverberative PmP arrivals across both profiles is indicative of layering of material above the Moho as a result of alternating relatively high and low velocity material (Cho et al., 2012). Fractionation leading to the formation of cumulates during cooling of a magmatic body or the intrusion of magmatic material in the form of sills near the base of the crust are two possible processes that would form layered magmatic material in the crust. Cumulate formations and layered intrusions are often associated with mafic to ultramafic magmatic bodies (Thybo, 2000; Cho et al., 2012). Additionally, layered intrusions may form cumulates within individual layers, leading to layering at multiple scales (Winter, 2010). Layering at both fine and large scales could explain why the reverberate PmP wave train is observed at both high and low frequencies. The high

frequency waves would sample relatively thinner layers in the high velocity layer, while low frequencies would sample relatively thicker layers in the high velocity layer.

6.2 Relation to rifting and CAMP

Multiple factors support a Mesozoic-aged rift- and CAMP-related origin for magmatic addition to the base of the coastal plain crust: the coincident voluminous CAMP event at 200 Ma (Condie, 1989; Hames et al., 2000), Mesozoic-aged onshore diking and offshore magmatism with similar seismic velocities attributed to rifting (Holbrook & Kelemen, 1993), as well as magmatism along the conjugate West African margin that has previously been determined to be rift related or at least coincident with rifting (Contrucci et al., 2004). The CAMP event is too large to be inconsequential to extension, and would have provided a significant amount of intruded magmatic material during early extension to assist successful rift development. A voluminous magmatic event such as CAMP may emplace magmatic additions, intrusions, and dikes throughout the crust, altering crustal composition and increasing observed seismic velocities throughout, explaining the elevated velocities observed in the models. High seismic velocities and layered material near the Moho can be indicative of a layered mafic magmatic intrusion to the base of the crust and are often associated with rifts (Thybo et al., 2000; Winter, 2010). Because the study area is entirely within CAMP boundaries, with evidence suggesting there has been significant layered magmatic addition to the crust, it seems likely that this ENAM magmatism is related to CAMP and helped initiate rifting at 200 Ma.

6.3 Other possible origins of magmatism

Given the complex tectonic history of the ENAM, other mechanisms could contribute to magmatic addition such as decompression melting of ascending material associated with Cenozoic aged delamination (Biryol et al., 2016). Null shear-wave splitting results in the region surrounding the ENAM may indicate upward flow of material in the mantle (Long et al., 2016). This upward flow could be a result of asthenospheric upwelling in response to lithospheric delamination, possibly leading to decompression melting and ponding of magmatic material at the base of the crust (Nelson, 1992). Volcanism associated with delamination formed a swarm of Cenozoic dikes in western North Carolina (Biryol et al., 2016), suggesting any delamination-related magmatism in the study area is likely Cenozoic in age.

Another potential alternative source of vertical mantle flow is the release of volatiles from the Juan de Fuca slab beneath the ENAM (Long et al., 2016). The presence of volatiles in the mantle can lower the solidus, which allows melting to occur at lower temperatures and/or higher pressures than would typically be required, facilitating magmatism in the upper mantle and intrusions into the lower crust (Shillington et al., 2009). Although these two scenarios are not mutually exclusive, it is difficult to determine which source for vertical flow (delamination, volatile flow, or both) best explains the null SKS arrivals and the influence this may have on the emplacement of magmatic material at the base of the crust. In either case, delamination and/or volatile flow would facilitate the emplacement of magmatic material near the base of the crust.

The previously proposed magmatic addition to the base of the crust as well as the potential layering near the Moho should result in a gradational Moho, as the density contrast between the upper mantle and lower crustal mafic material would be relatively low (Thurner et al., 2015). However, composite multimode common conversion point imaging reveal a high Ps/P ratio, indicating a sharp Moho beneath the ENAM study area (Schmandt et al., 2015). Similar attributes of the Moho have been observed beneath the Sierra Nevada (Ducea & Saleeby, 1998; Schmandt et al., 2015) and are likely a result of lithospheric delamination (Ducea & Saleeby, 1998) rather than magmatic addition. This evidence suggests, at the very least, that the Moho beneath the ENAM is a Cenozoic feature.

Since delamination of the lithosphere is a Cenozoic aged event this would imply that a portion of the magmatic addition is Cenozoic in age. Because delamination has occurred piecemeal throughout the Cenozoic and has migrated from east to west across the ENAM, this potentially delaminated related magmatic addition was emplaced during the earliest stages of delamination. This pattern could explain the lack of correlation with Triassic basins, since delamination and Triassic extension are unrelated. In this delamination origin scenario, some magmatism beneath the ENAM may be unrelated to rifting and is a Cenozoic feature.

7 Conclusions

Using onshore seismic refraction data collected as part of the Eastern North American Margin (ENAM) Community Seismic Experiment (CSE), this study constrains a high P-wave velocity (7.0-7.3 km/s) layer at the base of the crust of the Coastal Plain,

which appears similar to velocities of mafic magmatic material observed offshore the ENAM and at other rifts with significant magmatism (Holbrook & Kelemen, 1993; Christensen & Mooney, 1995; Shillington et al., 2009). Additionally, reverberate Moho reflection (PmP) arrivals indicate layering near the base of the crust (Thybo et al., 2000; Cho et al., 2012) attributed to either layered intrusions, cumulate formations, or both (e.g., Thybo et al., 2000).

I suggest that the magmatic material observed onshore was emplaced after Triassic extension, with magmatism migrating to its observed location offshore during successful rifting in the Jurassic due to changes in either mantle composition and/or flow patterns during the emplacement of the Central Atlantic Magmatic Provence (CAMP). In this case, it would seem that magmatism facilitated the rifting of strong continental crust in the Jurassic. This scenario explains why Triassic extension did not rupture the continental crust and develop into rifting: without magmatism to facilitate the development of rifting, extension failed. With the migration of extension to the east and the introduction of magmatic intrusions in the crust, extension could continue into rifting during the Jurassic, successfully rupturing the continental crust and forming oceanic crust.

8 References

Aleinikoff, J.N., Zartman, R.E., Walter, M., Rankin, D.W., Lyttle, P.T., Burton, W.C., 1995. U-Pb ages of metarhyolites of the Catocin and Mount Rogers formations, central and southern Appalachians: Evidence for two phases of Iapetan rifting. American Journal of Science 295, 428-454.

Aleinikoff, J.N., Burton, W.C., Lyttle, P.T., Nelson, A.E., Southworth, C.S., 2000. U-Pb geochronology ages of zircon and monazite from Mesoproterozoic granitic gneisses of the northern Blue Ridge, Virginia and Maryland, USA. Precambrian Research 99, 113-146.

Behn, M.D., and Lin, J., 2000. Segmentation in gravity and magnetic anomalies along the U.S. East Coast passive margin: Implications for incipient structure of the oceanic lithosphere. Journal of Geophysical Research 105(B11), 25,769-25,790.

Biryol, C.B., Wagern, L.S., Fischer, K.M., Hawman, R.B., 2016. Relationship between observred upper mantle structures and recent tectonic activity across the Southeastern United States. Journal of Geophysical Research: Solid Earth 121, 1-22.

Blackburn T.J., Olsen, P.E., Bowring, S.A., McLean, N.M., Kent, D.V., Puffer, J., McHone, G., Rasbury, E.T., Et-Touhami, M., 2013. Zircon U-Pb geochronology links the end-Triassic extinction with the Central Atlantic Magmatic Province. Science 340, 941-945.

Bott, M.H.P., Stein, S., Wortel, R., Kusznir, N., Fleitout, L., Zoback, M.L., Cartwright, J., 1991. Sublithosphereic loading and plate-boundary forces [and discussion].

Philosophical Transactions: Physical Sciences and Engineering 337(1645), 83-93.

Brown, P.M., 1985. Geologic map of North Carolina. North Carolina Department of Natural Resources, Geological Survey Section.

Buck, W.R., 2004. Consequences of asthenospheric variability on continental rifting. From: “Rheology and deformation of the lithosphere at continental margins,” 1-30, edited by G.D. Karner, B. Taylor, N.W. Driscoll, D.L. Kohlstedt, Columbia University Press, New York.

Calais, E., d’Oreye, N., Albaric, J., Deschamps, A., Delvaux, D., Deverchere, J., Ebinger, C., Ferdinand, R.W., Kervyn, F., Macheyeki, A.S., Oyen, A., Perrot, J., Saria, E., Smets, B., Stamps, D.S., Wautheir, C., 2008. Strain accommodation by slow slip and dyking in a youthful continental rift, East Africa. Nature 456, 783-788.

Carrigan, C.W., Miller, C.F., Fullagar, P.D., Bream, B.R., Hatcher, R.D., Jr., Coath, C.D., 2003. Ion microprobe age and geochemistry of southern Appalachian basement, with implications for Proterozoic and Paleozoic reconstructions. Precambrian Research 120, 1-36.

Cho, H.-M., Baag, C.-E., Lee, J.M., Moon, W.M., Jung, H., Kim, K.Y., 2012. P- and S-wave velocity model along crustal scale refraction and wide angle reflection profile in the southern Korean peninsula. Tectonophysics 582, 84-100.

Christensen, N.I., Mooney, W.D., 1995. Seismic velocity structure and composition of the continental crust: A global view. Journal of Geophysical Research 100(B7) 9761-9788.

Condie, K.C., 1989. Origin of the Earth's crust. Global and Planetary Change 1(1-2), 57-81.

Contrucci, I., Lingelhofer, F., Perrot, J., Bartolome, R., Gutscher, M.-A., Sahabi, M., Malod, J., Rehault, J.-P., 2004. The crustal structure of the NW Moroccan continental margin from wide-angle and reflection seismic data. Geophysical Journal International 159(1), 117-128.

Dalziel, I.W.D., 1991. Pacific margins of Laurentia and east Antarctica-Australia as a conjugate rift pair: Evidence and implications for an Eocambrian supercontinent. Geology 19, 598-601.

Ducea, H., Saleeby, J., 1998. A case for delamination of the deep batholithic crust beneath the Sierra Nevada, California. International Geology Review 40(1), 78-93.

Fenneman, N.M., Johnson, D.W., 1946. Physiographic divisions of the conterminous U.S. USGS.

Hames, W.E., Renne, P.R., Ruppel, C., 2000. New evidence for geologically instantaneous emplacement of earliest Jurassic Central Atlantic magmatic province basalts on the North American margin. Geology 28(9), 859-862.

Hatcher, R.D., Jr., 2010. The Appalachian orogeny: A brief summary. GSA Memoirs 206, 1-19.

Hibbard, J.P., Stoddard, E.F., Secor, D.T., Dennis, A.J., 2002. The Carolina zone: Overview of Neoproterozoic to early Paleozoic peri-Gondwanan terranes along the eastern flank of the southern Appalachians. Earth-Science Reviews 57, 299-339.

Holbrook, W.S., Purdy, G.M., Collins, J.A., Sheridan, R.E., Musser, D.L., Glover, L., III, Talwani, M., Ewing, J.I., Hawman, R., Smithson, R.B., 1992a. Deep velocity structure of rifted continental crust, US mid-Atlantic margin, from wide-angle reflection/refraction data. Geophysical Research Letters 19(16) 1,699-1,702.

Holbrook, W.S., Reiter, E.C., Purdy, G.M., Toksoz, M.N., 1992b. Image of the Moho across the continent-ocean transition, US east coast. Geology 20, 203-206.

Holbrook, W.S., Kelemen, P.B., 1993. Large igneous province on the US Atlantic margin and implications for magmatism during continental breakup. Nature 364, 433-436.

Holbrook, W.S., Purdy, G.M., Sheridan, R.E., Glover, L., III, Talwani, M., Ewing, J., Hutchinson, D., 1994. Seismic structure of the US mid-Atlantic continental margin. Journal of Geophysical Research 99(B9), 17,871-17,891.

Holbrook, W.S., Larsen, H.C., Korenaga, J., Dalh-Jensen, T., Reid, I.D., Kelemen, P.B., Hopper, J.R., Kent, G.M., Lizzaralde, D., Bernstein, S., Detrick, R.S., 2001. Mantle thermal structure and active upwelling during continental breakup in the North Atlantic. Earth and Planetary Science Letters 190, 251-266.

Long, M.D., Jackson, K.G., McNamara, J.F., 2016. SKS splitting beneath Transportable Array stations in eastern North America and the signature of past lithospheric deformation. Geochemistry Geophysics Geosystems 17, 2-15.

Luetgert, L.H., 1992. MacRay: Interactive two-dimensional seismic raytracing for the Macintosh. USGS Open-File Report 92-356.

Mazza, S.E., Gazel, E., Johnson, E.A., Kunk, M.J., McAleer, R., Spotila, J.A., Bizimis, M., Coleman, D.S., 2014. Volcanoes of the passive margin: The youngest magmatic event in eastern North America. Geology 42(6), 483-486.

McHone, J.G., 2000. Non-plume magmatism and rifting during the opening of the central Atlantic Ocean. Tectonophysics 316, 287-296.

Moser, T.J., 1991. Shortest path calculation of seismic rays. Geophysics 56(1), 59-67.

Nelson, K.D., 1992. Are crustal thickness variations in old mountain belts like the Appalachians a consequence of lithospheric delamination? Geology 20, 498-502.

Pratt, T.L., Coruh, C., Costain, J.K., Glover, L., III, 1988. A geophysical study of the Earth's crust in central Virginia: Implications for Appalachian crustal structure. Journal of Geophysical Research 93(B6), 6,649-6,667.

Robinson, C.J., Bickle, M.J., Minshull, T.A., White, R.S., Nichols, A.R.L., 2001. Low degree mantling under the Southwest Indian Ridge: The roles of mantle temperature, conductive cooling and wet melting. Earth and Planetary Science Letters 188, 383-398.

Rudnick, R.L., 1995. Making continental crust. Nature 378, 571-578.

Schlische, R.W., 2003. Progress in understanding the structural geology, basin evolution, and tectonic history of the eastern North American margin. From: “The Great Rift Valleys of Pangea in Eastern North America; Volume One: Tectonics, Structure, and Volcanism,” 21-64, edited by Peter M. LeTourneau and Paul E. Olsen, Colombia University Press, New York.

Schmandt, B., Lin, F.-C., Karlstrom, K.E., 2015. Distinct crustal isostasy trends east and west of the Rocky Mountain Front. Geophysical Research Letters 42, 10,290-10,298.

Secor, D.T., Samson, S., Snoke, A., Palmer, A., 1983. Confirmation of the Carolina slate belt as an exotic terrane. Science 221, 649-651.

Sheridan, R.E., Musser, D.L., Glover, L., III, Talwani, M., Ewing, J.I., Holbrook, W.S., Purdy, G.M., Hawman, R., Smithson, S., 1993. Deep seismic reflection data of EDGE US mid-Atlantic continental-margin experiment: Implications for Appalachian sutures and Mesozoic rifting and magmatic underplating. Geology 21, 563-567.

Shillington, D.J., Scott, C.L., Minshull, T.A., Edwards, R.A., Brown, P.J., White, N., 2009. Abrupt transition from magma-starved to magma-rich rifting in the eastern Black Sea. Geology 37(1), 7-10.

Steckler, M.S., Watts, A.B., 1981. Subsidence history and tectonic evolution of Atlantic-type continental margins. From: “Dynamics of Passive Margins,” 184-196, edited by R.A. Scrutten, AGU Geodynamics Series 6, Washington, D.C.

Swanson, M.T., 1986. Preexisting fault control for Mesozoic basin formation in eastern North America. Geology 14, 419-422.

Thomas, W.A., 2006. Tectonic inheritance at a continental margin. GSA Today 16(2), np.

Thomas, W.A., 2011. The Iapetan rifted margin of southern Laurentia. Geosphere 7(1), 97-120.

Thurner, S., Margolis, R., Niu, A.L., 2015. PdS receiver function evidence for crustal scale thrusting, relic subduction, and mafic underplating in the Trans-Hudson Orogen and Yavapai province. Earth and Planetary Science Letters 426, 13-22.

Thybo, H., Maguire, P.K.H., Birt, C., Perchuc, E., 2000. Seismic reflectivity and magmatic underplating beneath the Kenya Rift. Geophysical Research Letters 27(17), 2,745-2,748.

Thybo, H., Artemieva, I.M., 2013. Moho and magmatic underplating in continental lithosphere. Tectonophysics 609, 605-619.

Toomey, D.R., Foulger, G.R., 1989. Tomographic inversion of local earthquake data from the Hengill-Grensdalur central volcano complex, Iceland. Journal of Geophysical Research 94(12), 497-517.

Toomey, D.R., Solomon, S.C., Purdy, G.M., 1994. Tomographic imaging of the shallow crustal structure at 9°30'N. Journal of Geophysical Research 99, 24,135-24-157.

Van Avendonk, H.J.A., Shillington, J.S., Holbrook, W.S., Hornbach, M.J., 2004. Inferring crustal structure in the Aleutian island arc from a sparse wide-angle seismic data set. Geochemistry Geophysics Geosystems 5(8), np.

Van Avendonk, H.J.A., McIntosh, K.D., Kuo-Chen, H., Lavier, L.L., Okaya, D.A., Wu, F.T., Wang, C.-Y., Lee, C.-S., Liu, C.-S., 2016. A lithospheric profile across northern Taiwan: From arc-continent collision to extension. Geophysical Journal International 204, 331-346.

Vick, H., Channell, J., Opdyke, N., 1987. Ordovician docking of the Carolina slate belt: paleomagnetic data. Tectonics 6, 573-583.

Wagner, L.S., Long, M.D., Johnston, M.D., Benoit, M.H., 2012. Lithospheric and asthenospheric contributions to shear-wave splitting observations in the southeastern United States. Earth and Planetary Science Letters 341-344, 128-138.

Walsh, G.J., Aleinikoff, J.N., 1999. U-Pb zircon age of metafelsite from the Pinney Hollow Formation: Implications for the development of the Vermont Appalachians. American Journal of Science 299, 157-170.

Whitmeyer, S.J., Karlstrom, K.E., 2007. Tectonic model for the Proterozoic growth of North America. Geosphere 3(4), 220-259.

Winter, J.D., 2010. Principles of igneous and metamorphic petrology, second edition. Pearson Prentice Hall.

Withjack, M.O., Schlische, R.W., Olsen, P.E., 1998. Diachronous rifting, drifting, and inversion on the passive margin of central eastern North America: An analog for other passive margins. AAPG Bulletin 82(5A), 817-835.

Yuan, H., French, S., Cupillard, P., Romanowicz, B., 2014. Lithospheric expression of geologic units in central and eastern North America from full waveform tomography. Earth and Planetary Science Letters 402, 176-186.

Zihlman, F.N., 1992. PLOTSEGY V1.0: A DOS graphics program to display SEG-Y disk-image seismic data. USGS Open-File Report 92-349B.

9 Figures

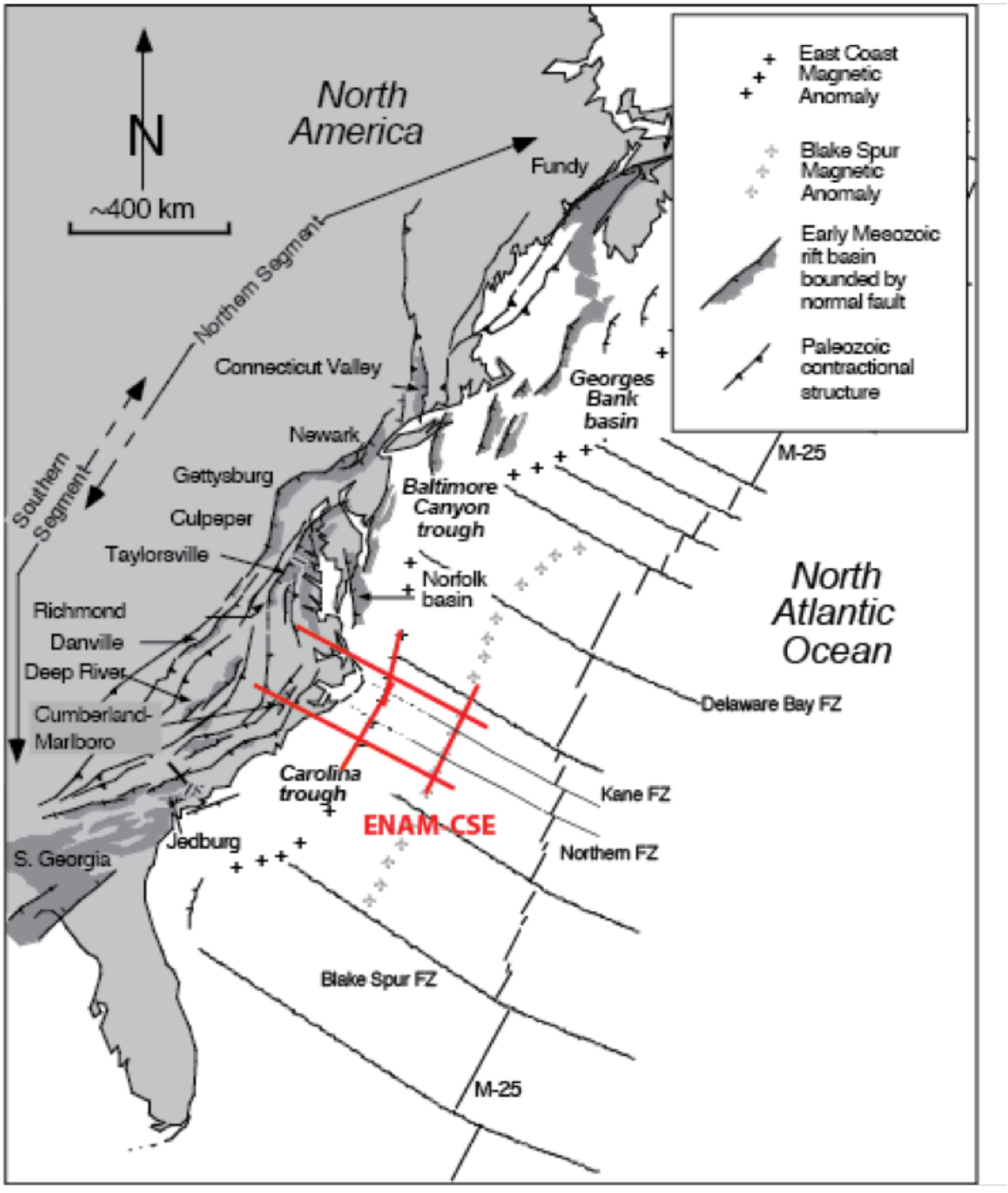

Figure 1: Regional map of the ENAM showing offshore magnetic anomalies, Triassic basins, and offshore fracture zones. Red lines show onshore and offshore profiles from the ENAM CSE (after Withjack et al., 1998).

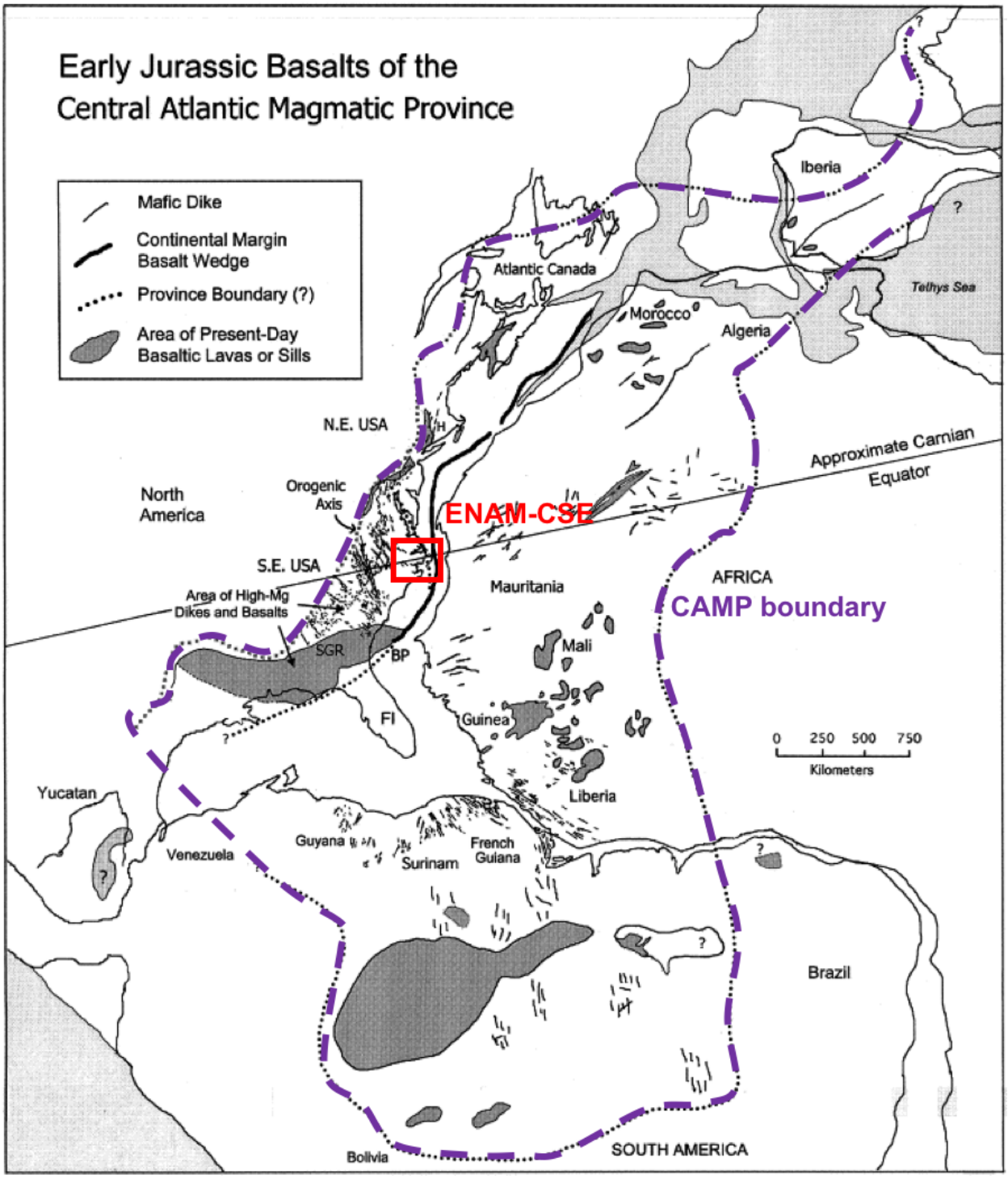

Figure 2: Reconstruction of the region showing continent configuration 200 Ma near the break up of Pangea and emplacement of CAMP. Purple dashed line delineates CAMP boundary. Red box indicates ENAM CSE (after McHone, 2000).

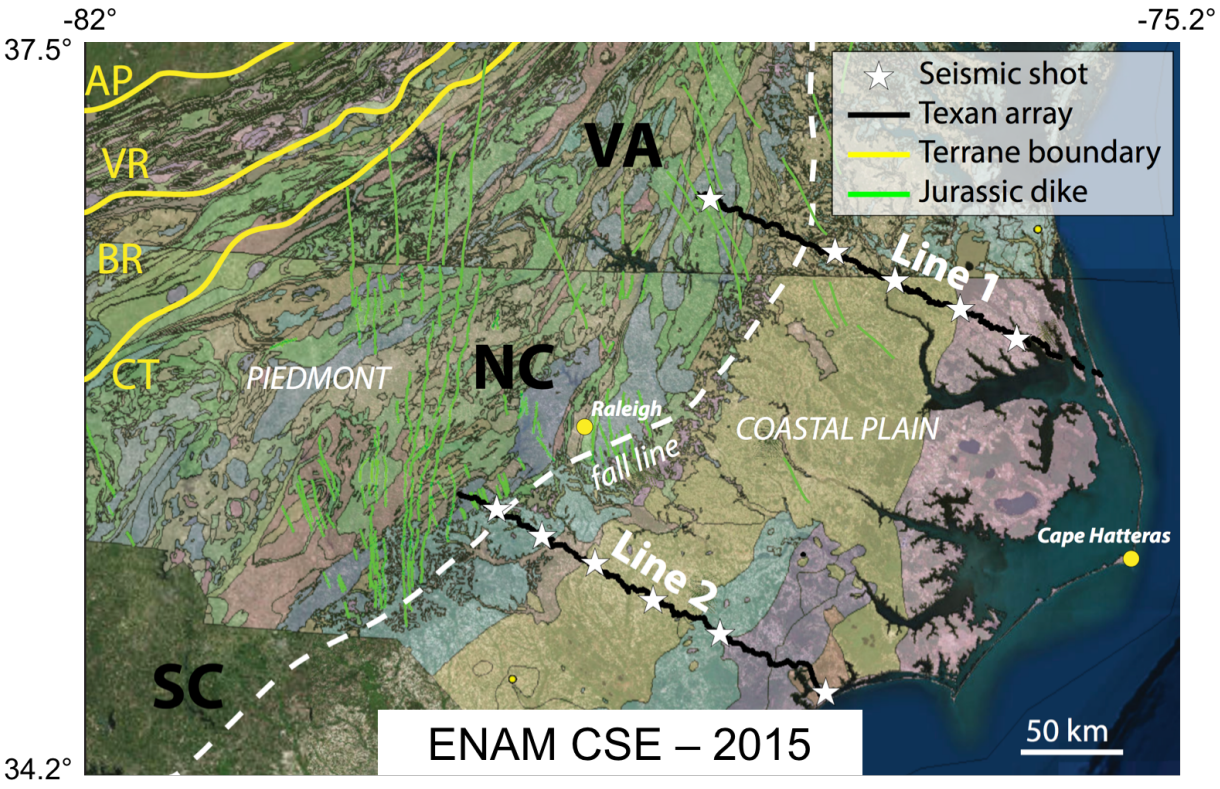

Figure 3: ENAM onshore experiment showing station locations (black circles) and explosion locations (white stars) with Jurassic dikes (green lines), physiographic provinces, accreted terranes, and geology (after Fenneman & Johnson, 1946; Brown, 1985).

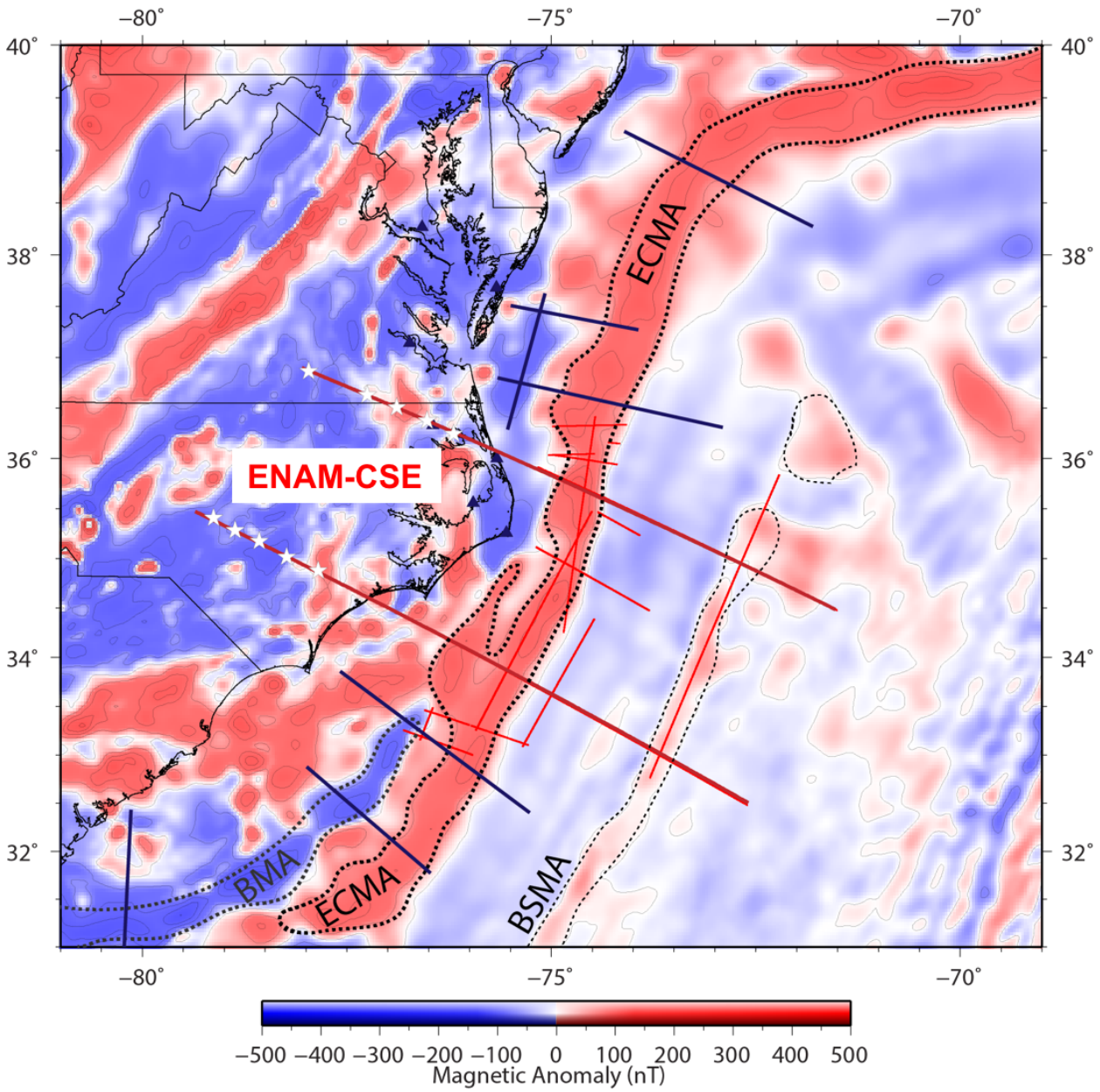

Figure 4: ENAM CSE with magnetic anomaly base map. Thick red lines show onshore/offshore profiles. Thin red lines show offshore profiles. Thick blue lines show previous seismic experiments from the region. Stars show onshore shot point locations.

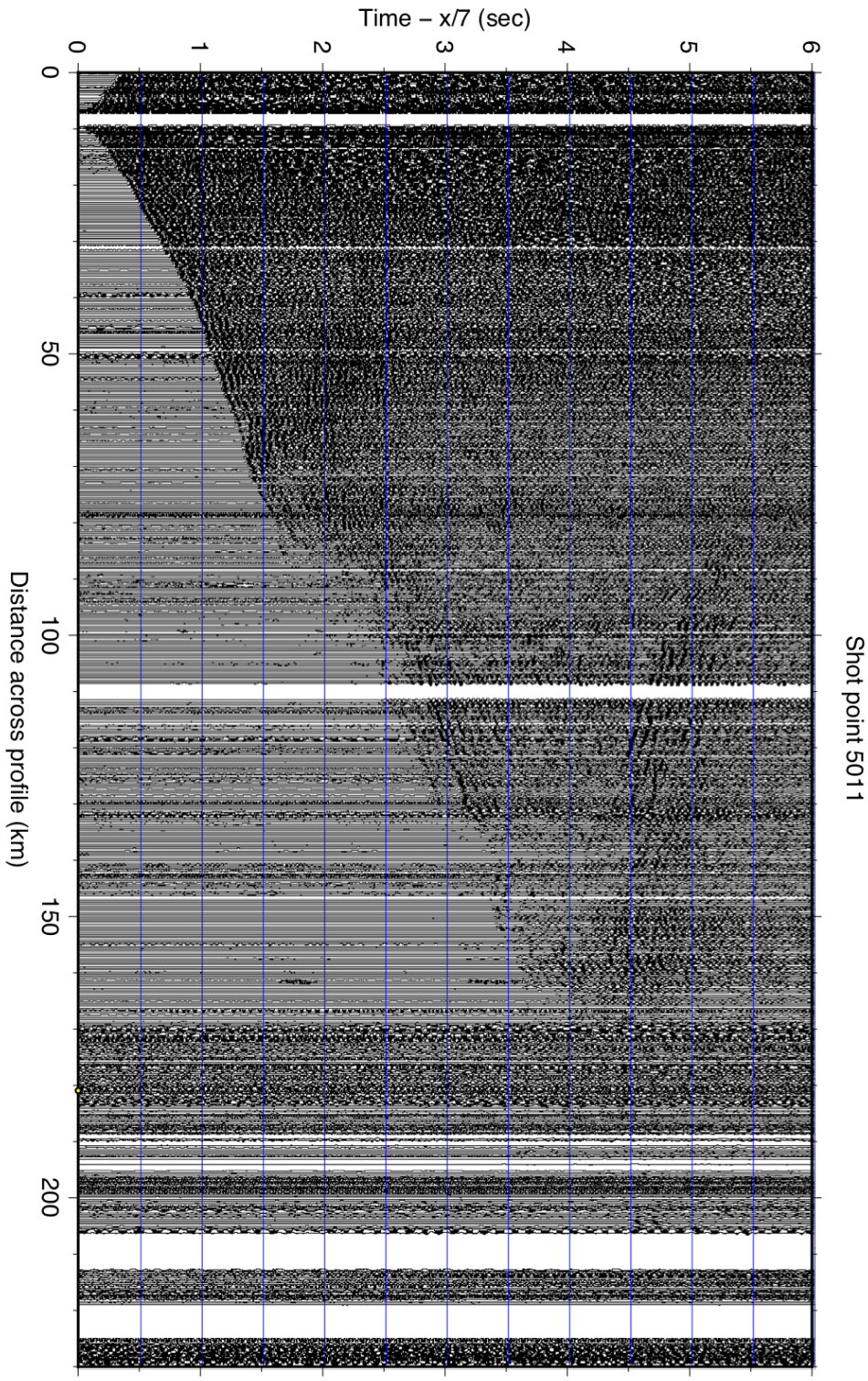
Time – x/7 (sec)
0
1
2
3
4
5
6
Distance across profile (km)
0
50
100
150
200
Shot point 5011

Figure 5: Uninterpreted shot gather of shot point 11, Line 1. Velocity reduction is 7 km/s.

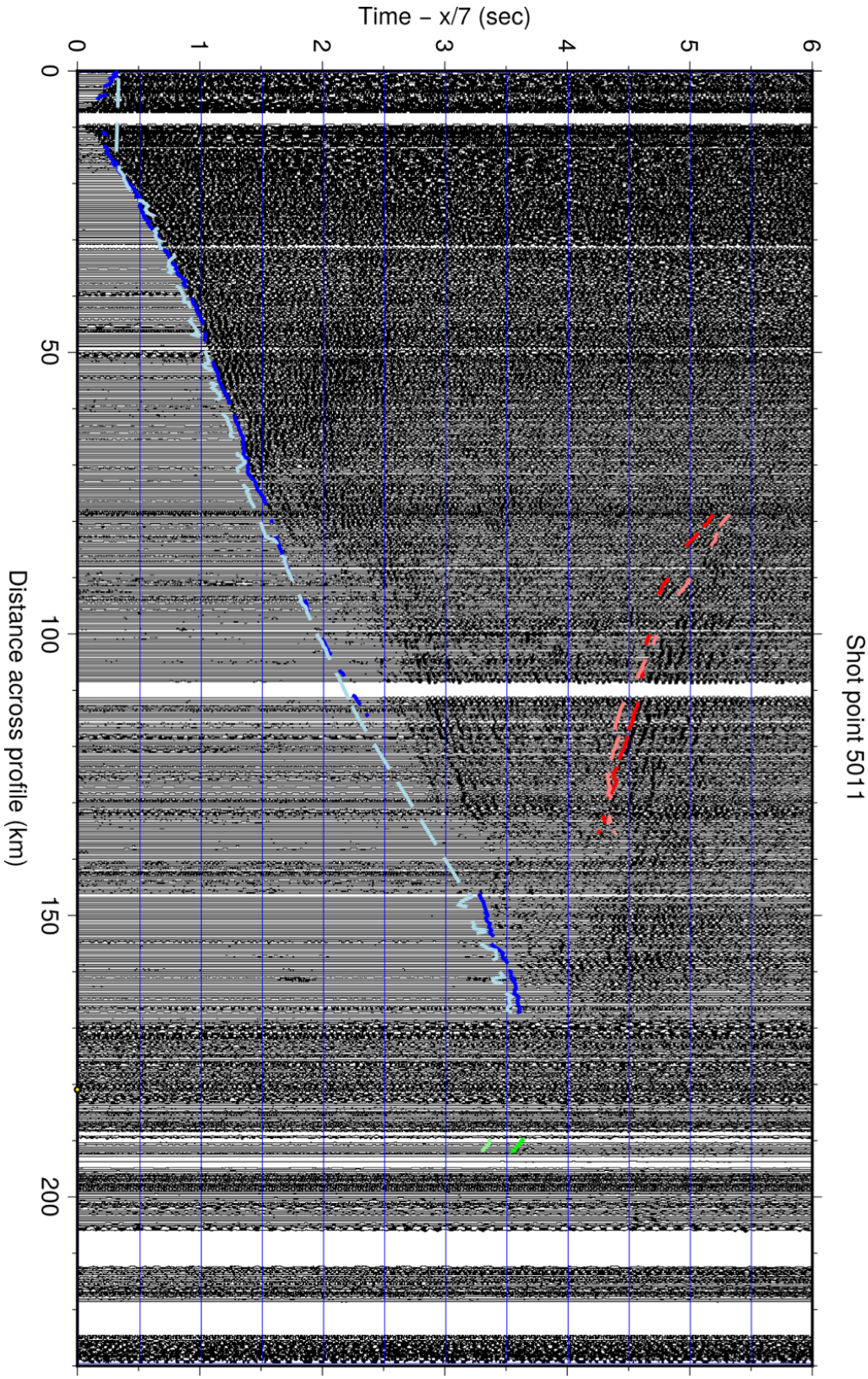
Time – x/7 (sec)
0
1
2
3
4
5
6
Distance across profile (km)
0
50
100
150
200
Shot point 5011

Figure 6: Interpreted shot gather of shot point 11, Line 1. Dark blue line shows picked crustal refraction (Pg) arrivals. Light blue line shows calculated Pg arrivals. Dark red line shows picks Moho reflection (PmP) arrivals. Light red line shows calculated PmP arrivals. Dark green line shows picks Moho refraction (Pn) arrivals. Light green line shows calculated Pn arrivals. Velocity reduction is 7 km/s.


Time – x/7 (sec)
0
1
2
3
4
5
6
0
50
100
150
200
Shot point 5023

Figure 7: Uninterpreted shot gather of shot point 23, Line 2. Velocity reduction is 7 km/s.

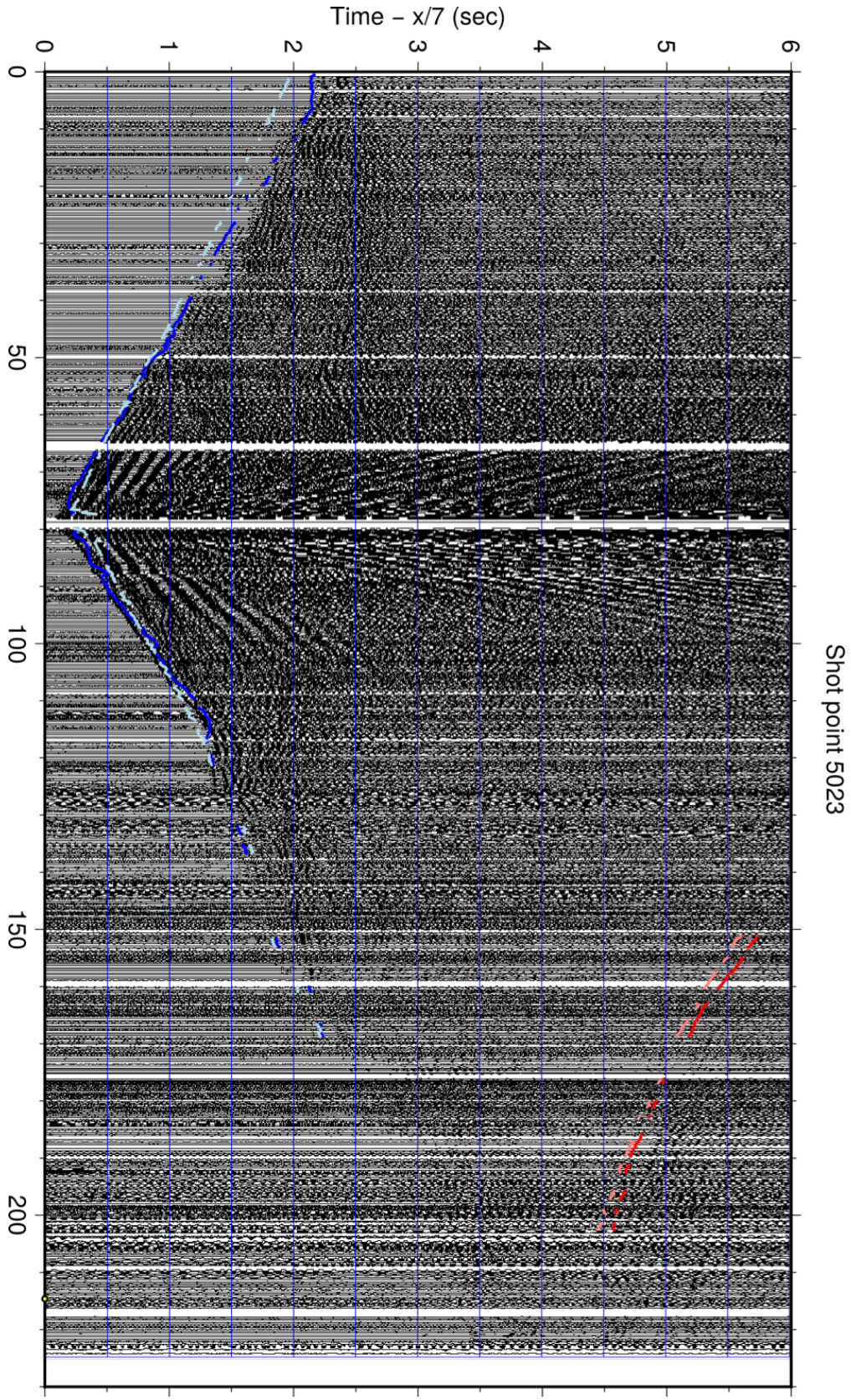
Time – x/7 (sec)
0
1
2
3
4
5
6
0
50
100
150
200
Shot point 5023

Figure 8: Interpreted shot gather of shot point 23, Line 2. Dark blue line shows picked crustal refraction (Pg) arrivals. Light blue line shows calculated Pg arrivals. Dark red line shows picks Moho reflection (PmP) arrivals. Light red line shows calculated PmP arrivals. Velocity reduction is 7 km/s.

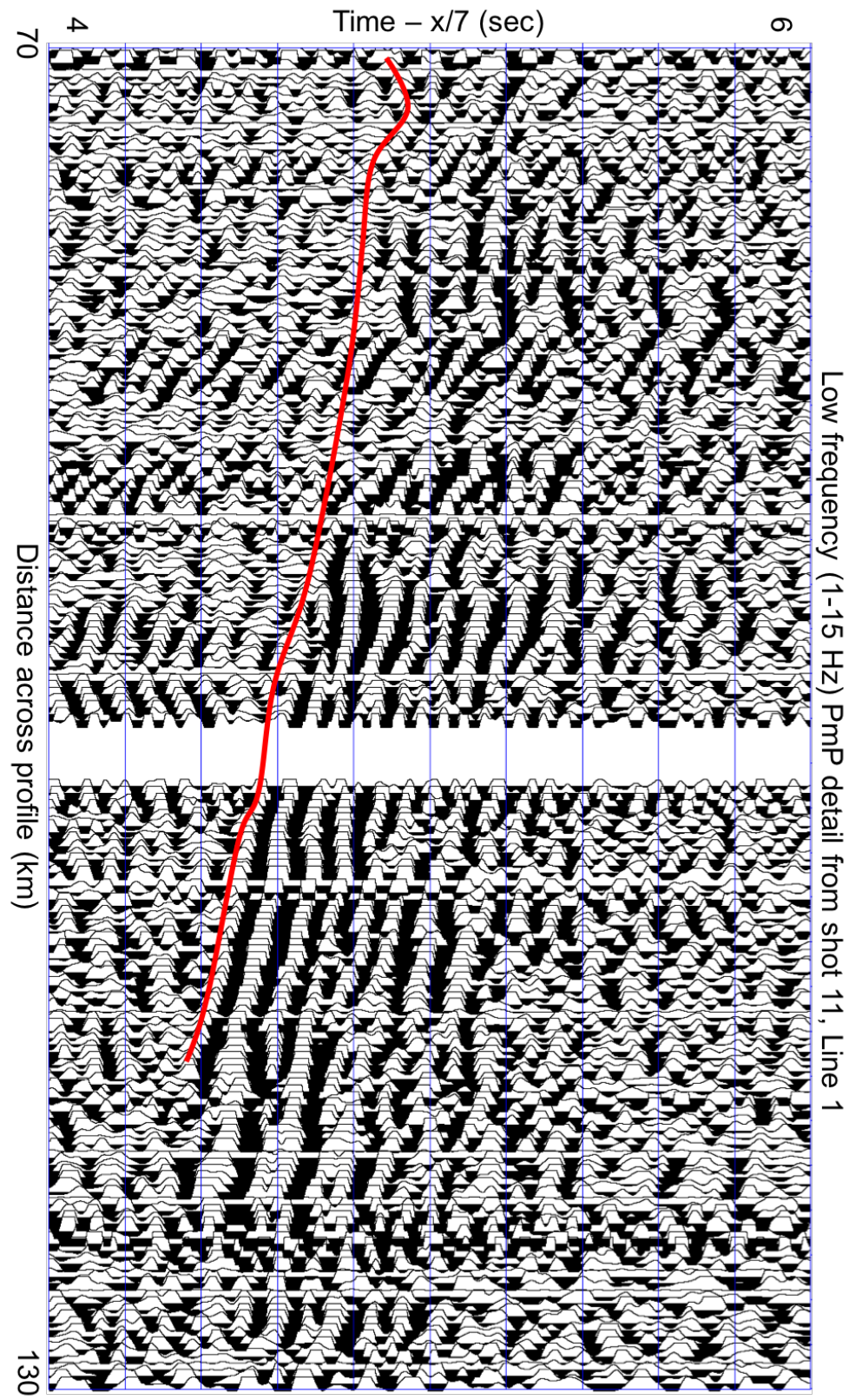
Time – x/7 (sec)
4
6
70
130
Distance across profile (km)
Low frequency (1-15 Hz) PmP detail from shot 11, Line 1

Figure 9: Detail of reverberate PmP arrivals from shot 11 Line 1. Filtered to low (1-15 Hz) frequencies. Velocity reduction is 7 km/s.

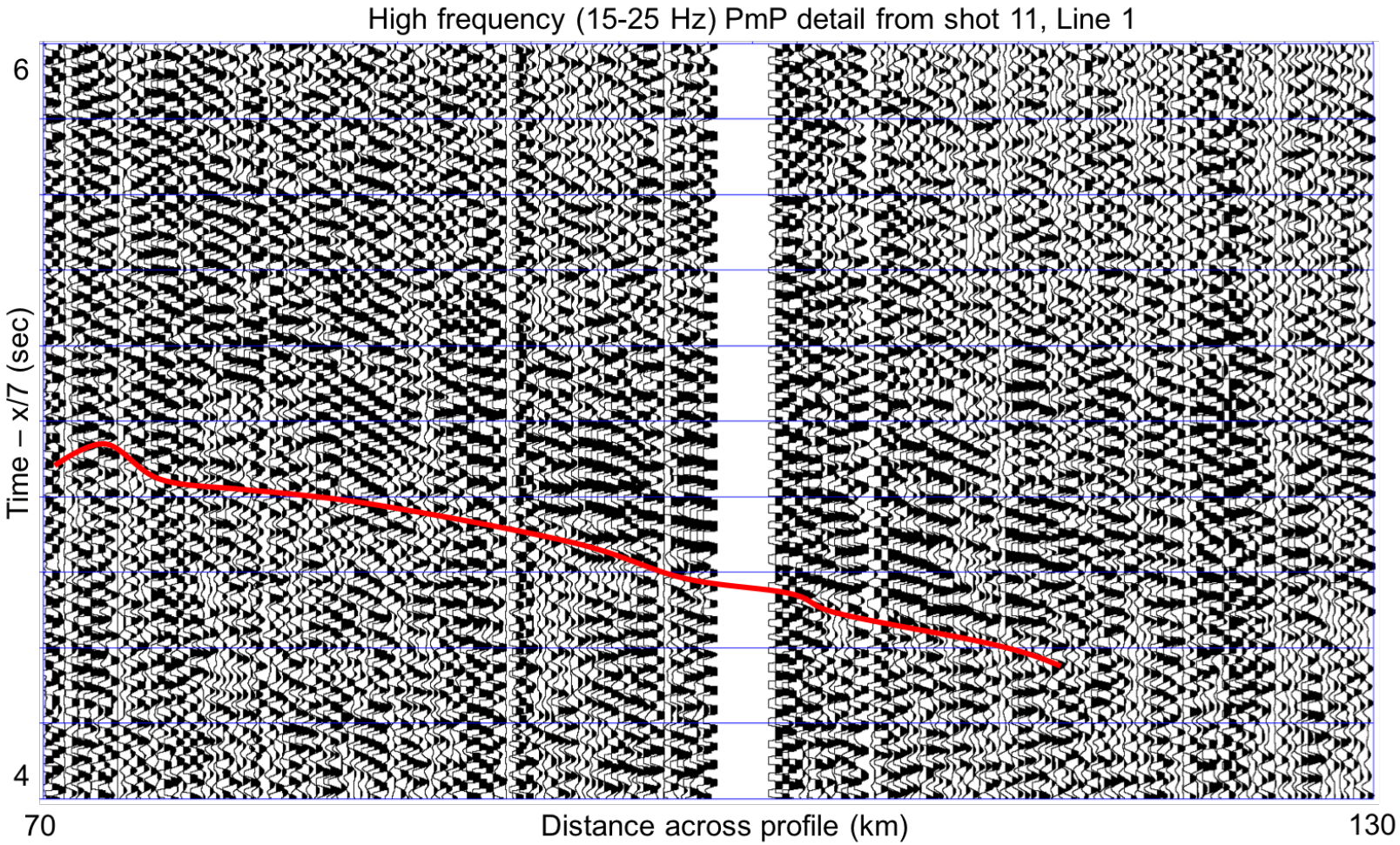
High frequency (15-25 Hz) PmP detail from shot 11, Line 1
6
4
Time – x/7 (sec)
70
Distance across profile (km)
130

Figure 10: Detail of reverberate PmP arrivals from shot 11 Line 1. Filtered to high (15-25 Hz) frequencies. Velocity reduction is 7 km/s.

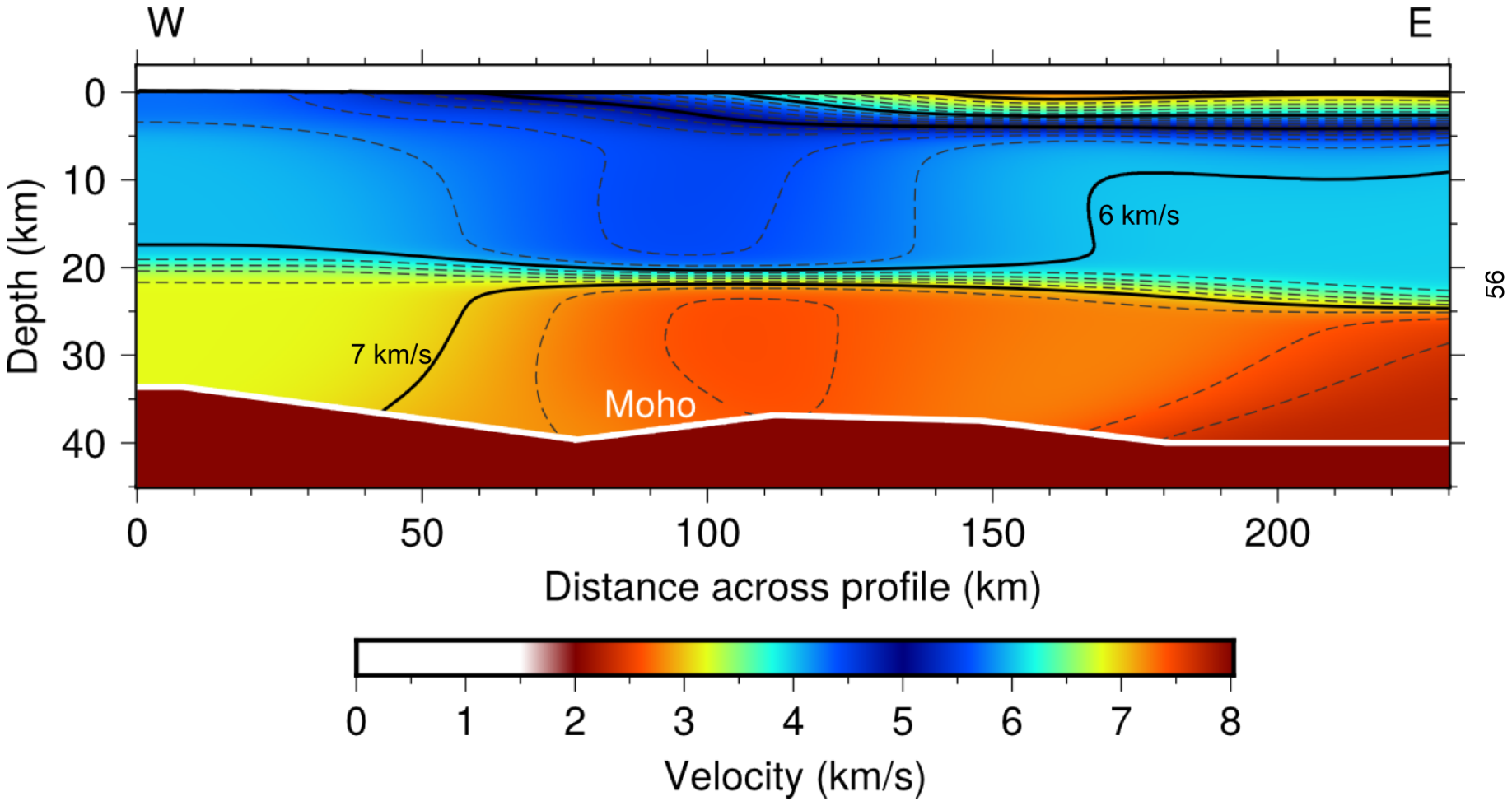
W
E
Depth (km)
0
10
20
30
40
6 km/s
7 km/s
Moho
0
50
100
150
200
Distance across profile (km)
0
1
2
3
4
5
6
7
8
Velocity (km/s)

Figure 11: Line 1 starting velocity model constructed from 1-D models from each shot gather.

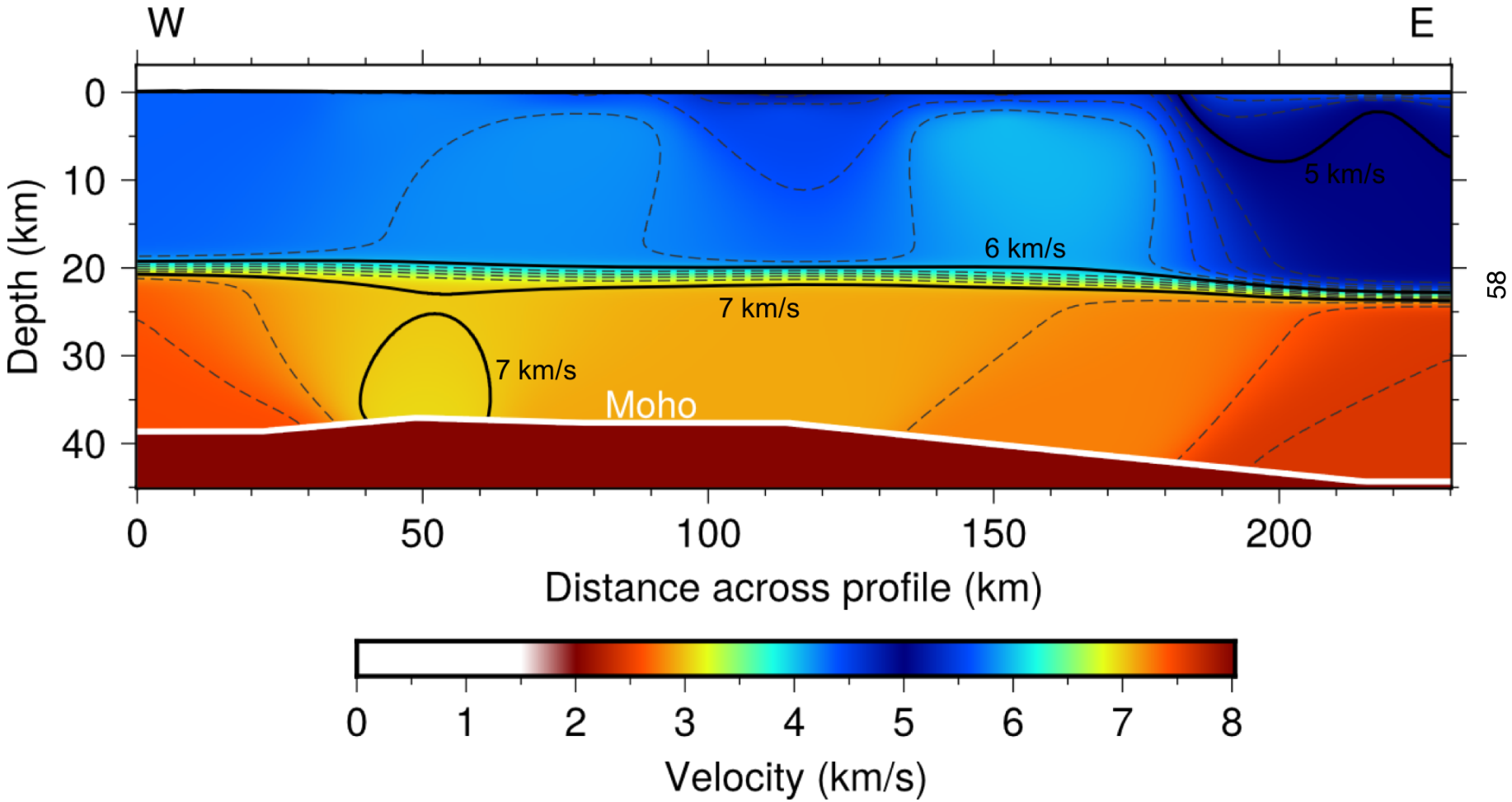
W
E
0
10
20
30
40
Depth (km)
5 km/s
6 km/s
7 km/s
7 km/s
Moho
0
50
100
150
200
Distance across profile (km)
0
1
2
3
4
5
6
7
8
Velocity (km/s)

Figure 12: Line 2 starting velocity model constructed from 1-D models from each shot gather.

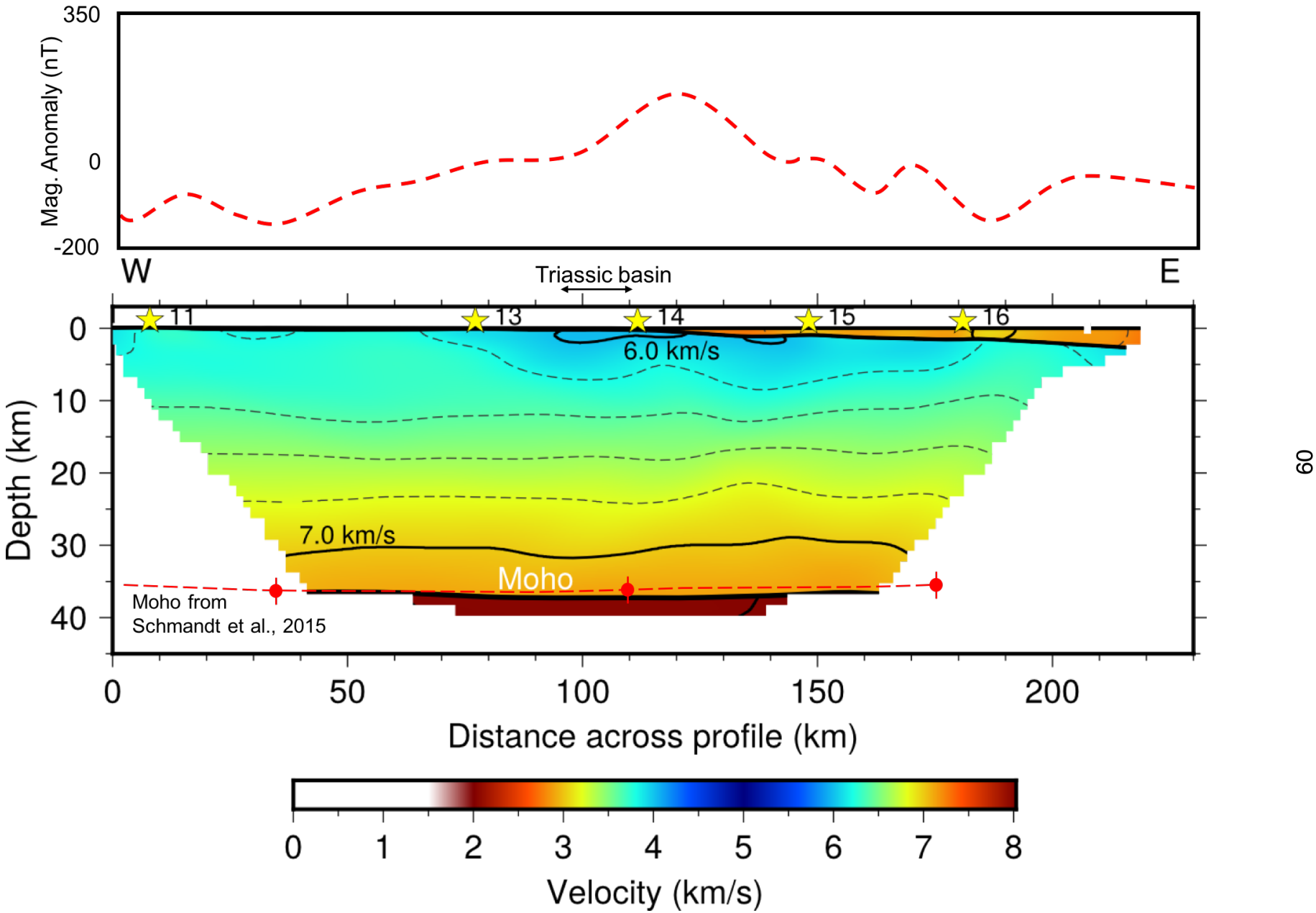
350
0
-200
Mag. Anomaly (nT)
W
Triassic basin
E
11
13
14
15
16
6.0 km/s
7.0 km/s
Moho
Moho from
Schmandt et al., 2015
Depth (km)
0
10
20
30
40
0
50
100
150
200
Distance across profile (km)
0
1
2
3
4
5
6
7
8
Velocity (km/s)

Figure 13: Line 1 final velocity model after tomographic inversion following iterative ray tracing and inversion methods from van Avendonk et al. (2004) with magnetic anomalies (top). Moho depth from Schmandt et al. (2015) with an uncertainty of +/- 2 km. Stars represent shot points and numbers. Chi squared = 1.0; RMS travel time residual = 106 ms. Contour interval is 0.2 km/s.

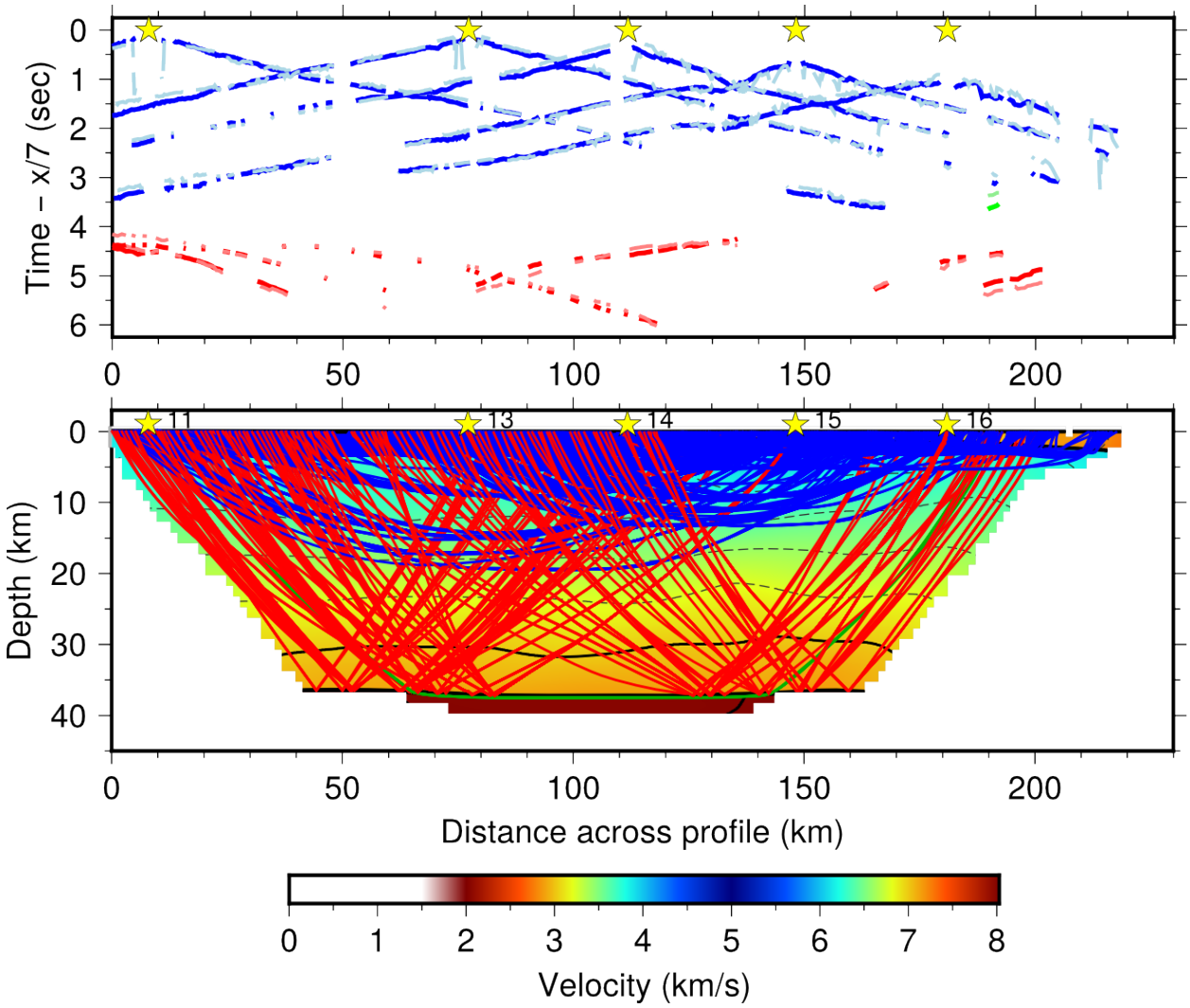

Figure 14: (Top) Line 1 travel time curves with picked (dark colored lines) and calculated (light colored lines) arrivals. Blue lines show Pg arrivals, red lines show PmP arrivals, and green lines show Pn arrivals. Stars represent shot points and numbers. (Bottom) Line 1 fine velocity model showing representative ray coverage across the model. Blue lines show Pg rays, red lines show PmP rays, and green lines show Pn rays. Stars represent shot points and numbers.

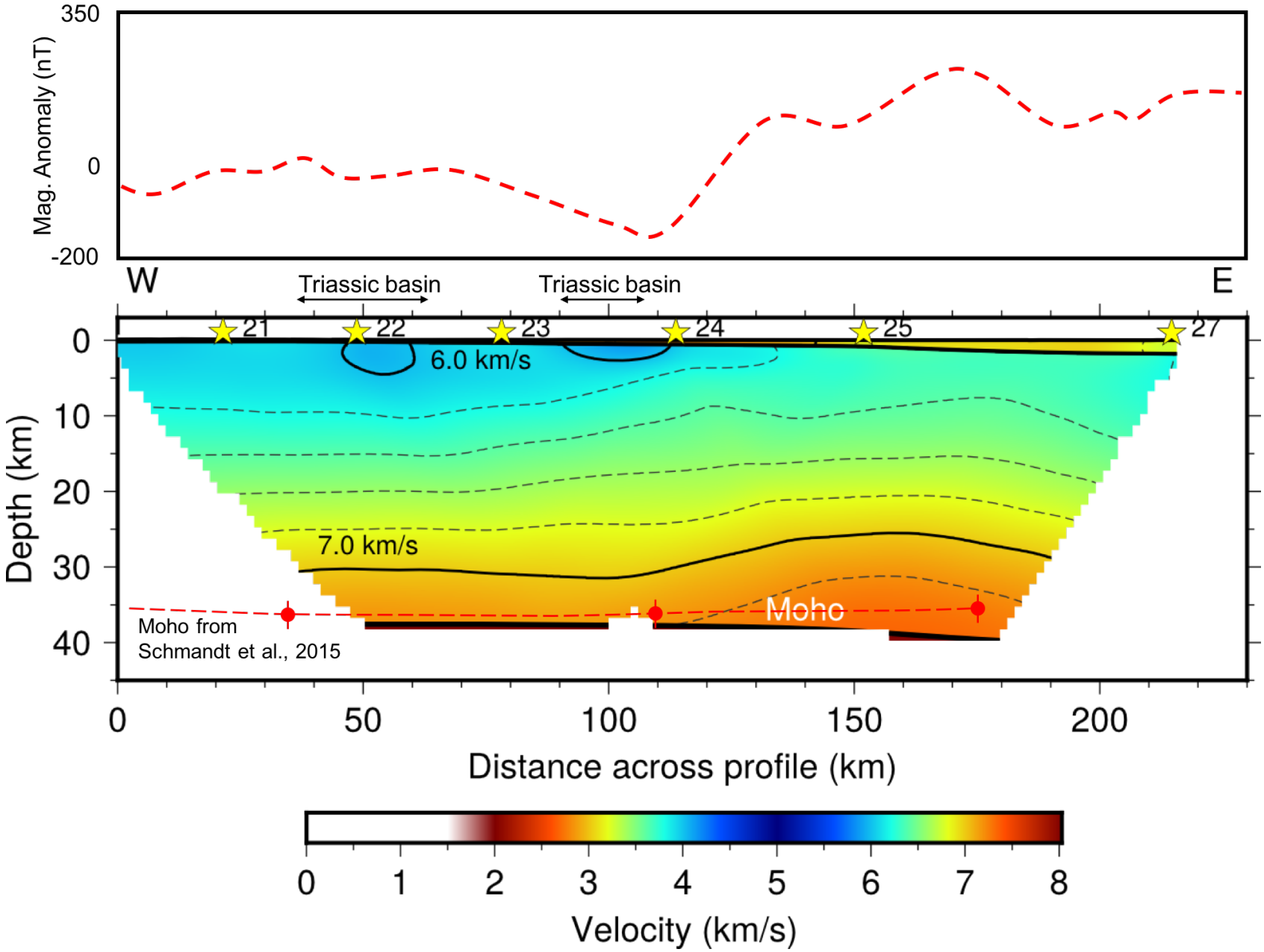
350
0
-200
Mag. Anomaly (nT)
W
E
Triassic basin
Triassic basin
21
22
23
24
25
27
6.0 km/s
7.0 km/s
Moho
Moho from
Schmandt et al., 2015
Depth (km)
0
10
20
30
40
0
50
100
150
200
Distance across profile (km)
0
1
2
3
4
5
6
7
8
Velocity (km/s)

Figure 15: Line 2 final velocity model after tomographic inversion following iterative ray tracing and inversion methods from van Avendonk et al. (2004) with magnetic anomalies (top). Moho depth from Schmandt et al. (2015) with an uncertainty of +/- 2 km. Stars represent shot points and numbers. Chi squared = 1.0; RMS travel time residual = 114 ms. Contour interval is 0.2 km/s.

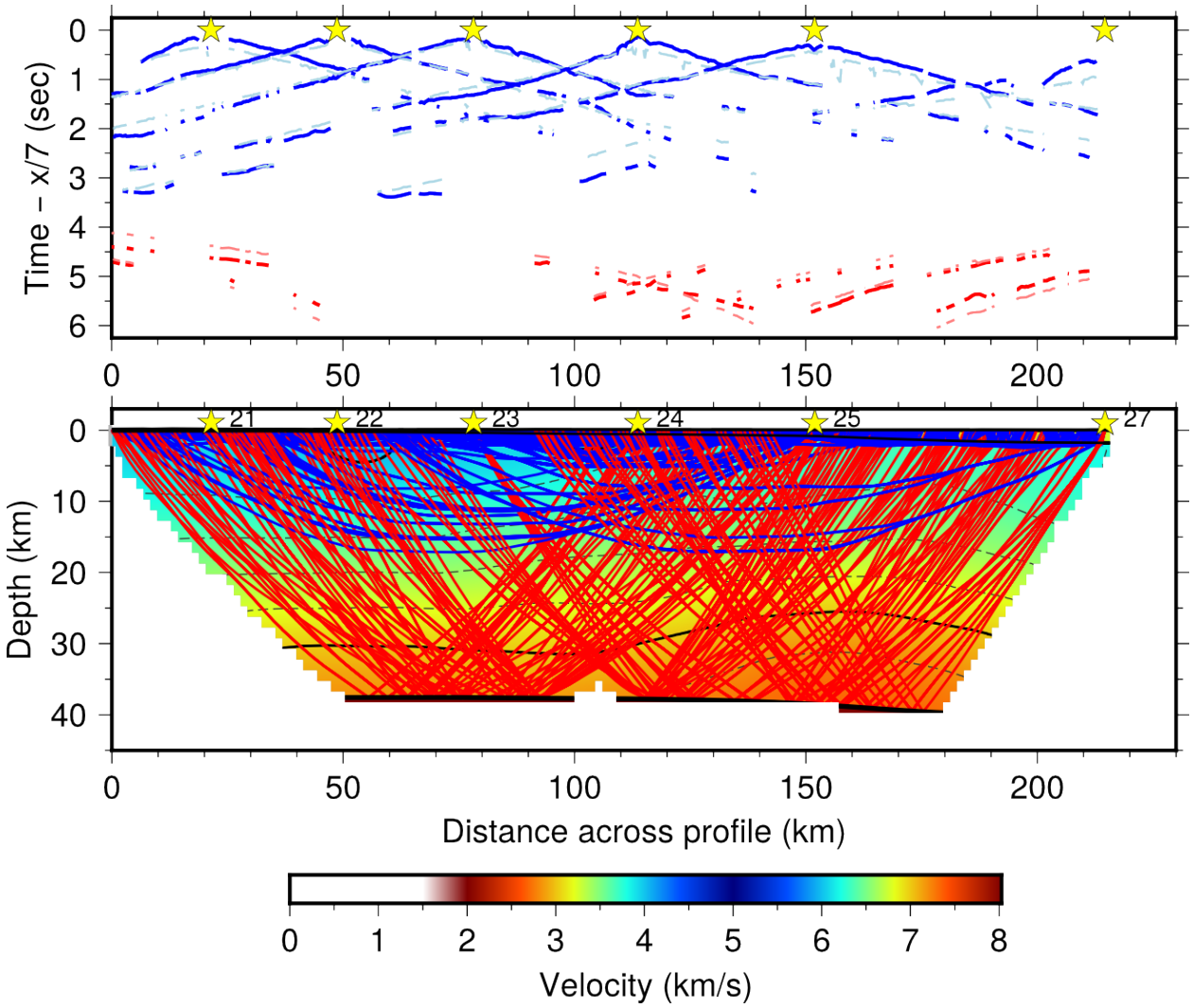

Figure 16: (Top) Line 2 travel time curves with picked (dark colored lines) and calculated (light colored lines) arrivals. Blue lines show Pg arrivals and red lines show PmP arrivals. Stars represent shot points and numbers. (Bottom) Line 2 fine velocity model showing representative ray coverage across the model. Blue lines show Pg rays and red lines show PmP rays. Stars represent shot points and numbers.

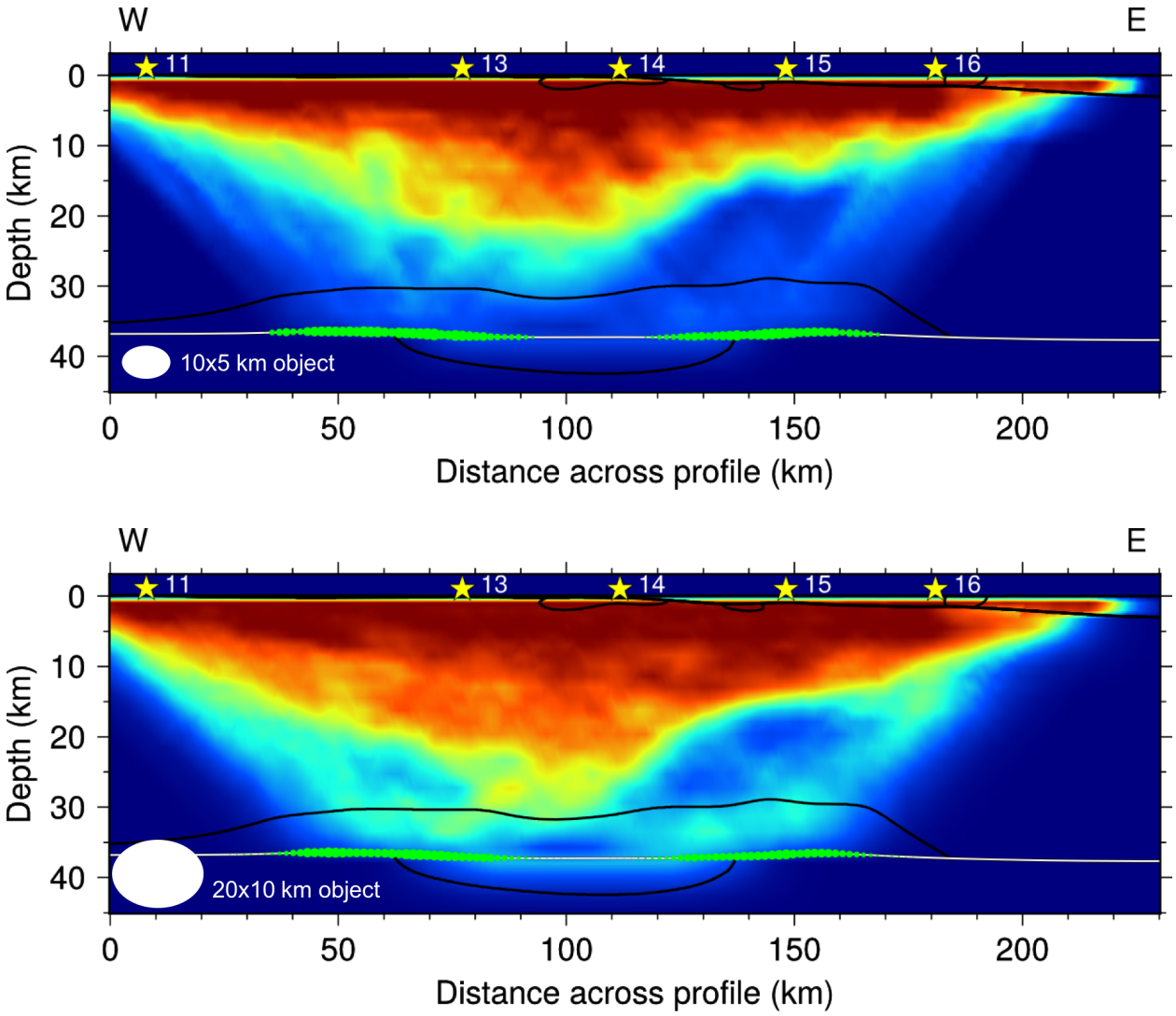
W
E
11
13
14
15
16
0
10
20
30
40
Depth (km)
10x5 km object
0
50
100
150
200
Distance across profile (km)
W
E
11
13
14
15
16
0
10
20
30
40
Depth (km)
20x10 km object
0
50
100
150
200
Distance across profile (km)

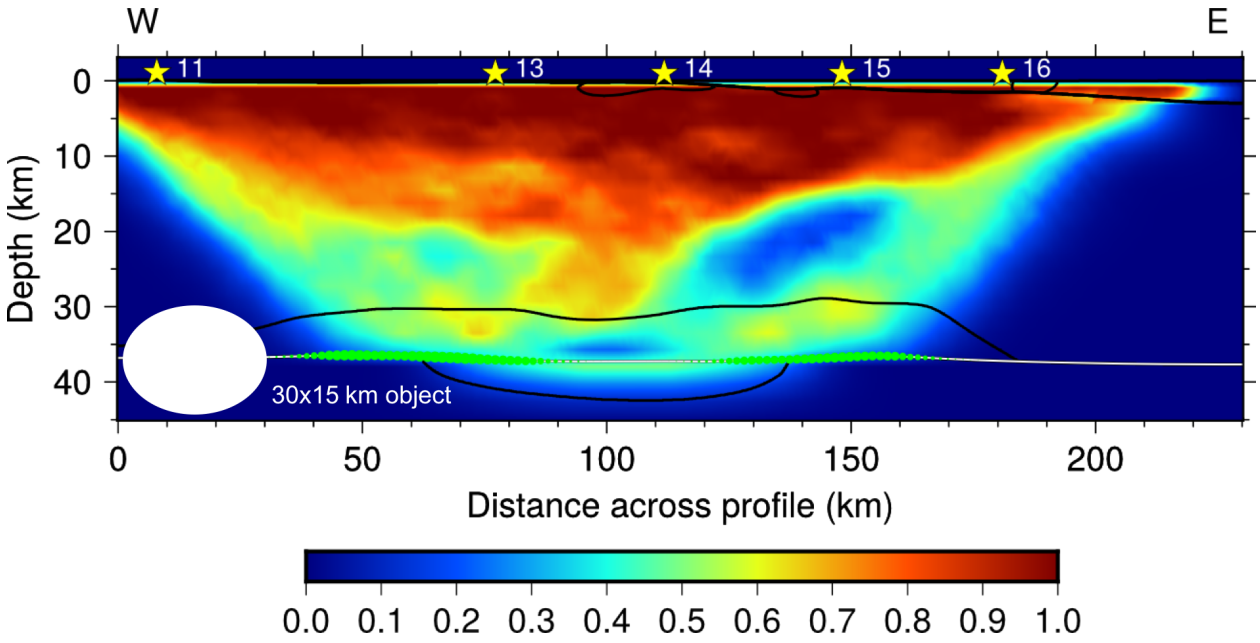

Figure 17: Resolution of seismic velocity variations and layer boundary depth at varying scales for Line 1, showing 6.0 km/s and 7.0 km/s contours. Stars represent shot points and numbers. (Top) Elliptical model features that measure 10x5 km are well resolved in the upper 10 km of the crust across the profile, with moderate resolution below 15 km in the middle of the profile and poor resolution below 10 km on the sides and 30 km in the middle of the model. (Middle) Elliptical model features that measure 20x10 km are well resolved in the upper 10 km of the crust across the profile, with moderate resolution below 20 km in the middle of the profile. (Bottom) Elliptical model features that measure 30x15 km are well resolved in throughout the model, except around 35 km depth in the middle of the model and between 15 km and 30 km in the eastern portion of the model.

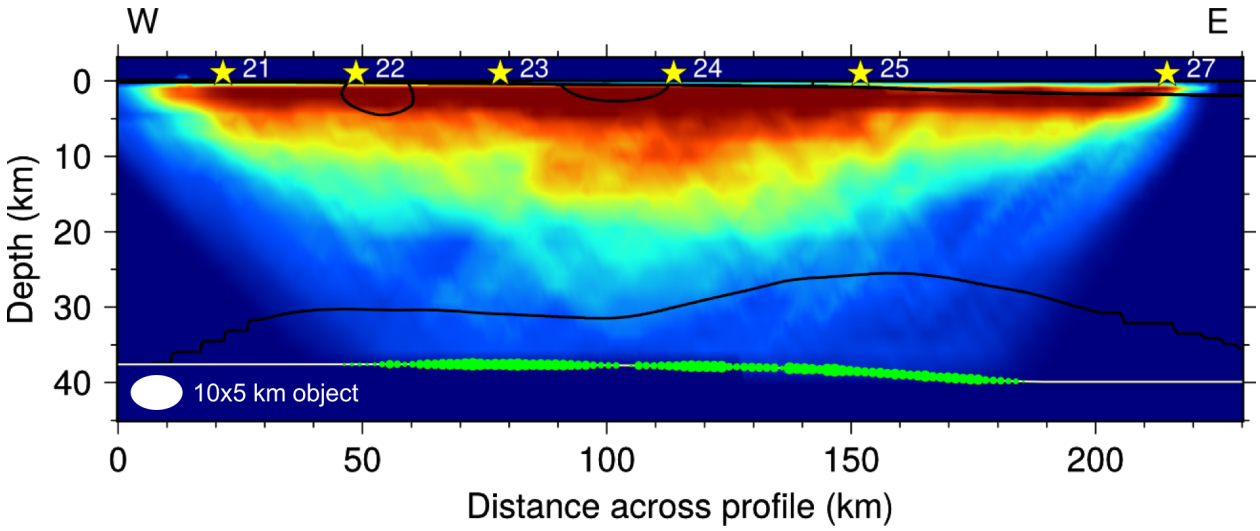
W
E
21
22
23
24
25
27
0
10
20
30
40
Depth (km)
10x5 km object
0
50
100
150
200
Distance across profile (km)

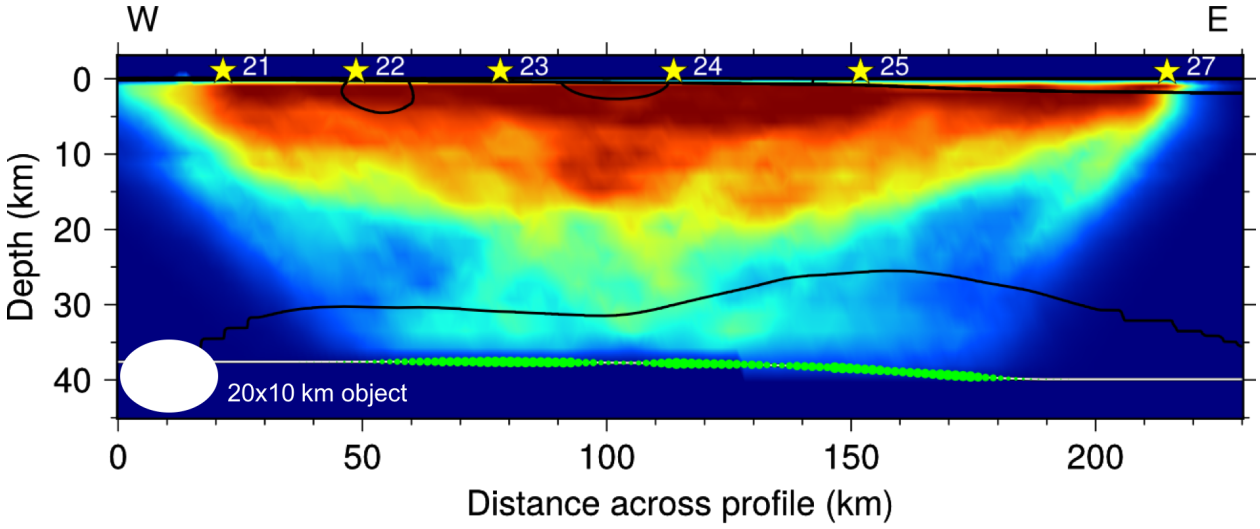
W
E
21
22
23
24
25
27
0
10
20
30
40
Depth (km)
20x10 km object
0
50
100
150
200
Distance across profile (km)

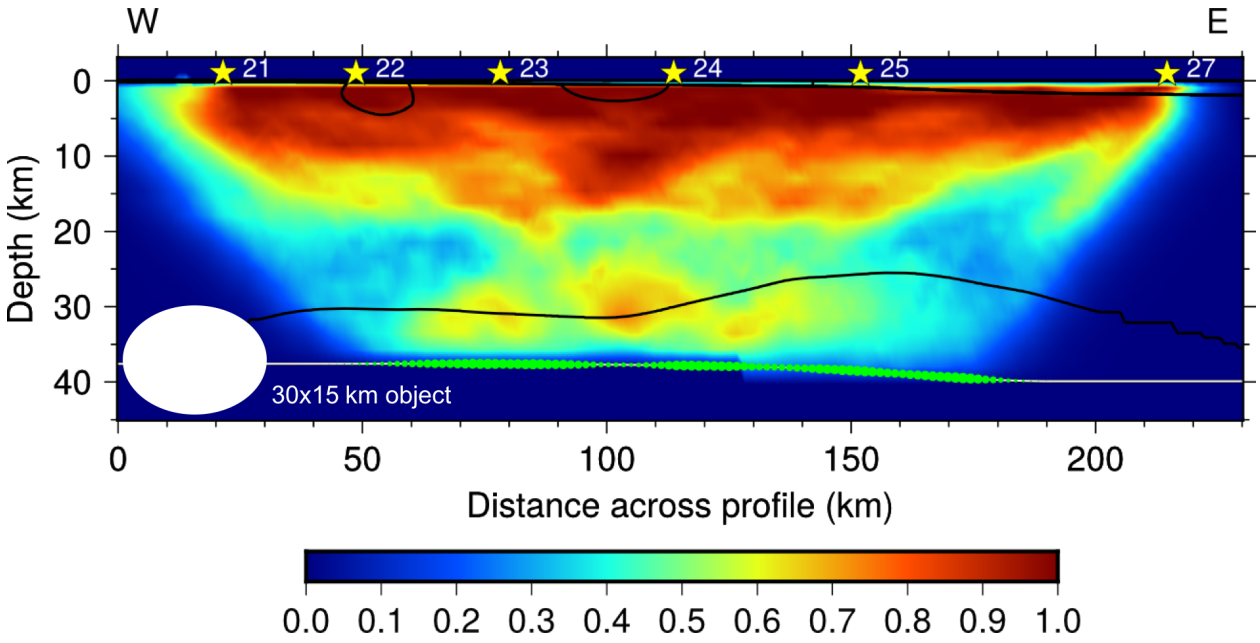

Figure 18: Resolution of seismic velocity variations and layer boundary depth at varying scales for Line 2, showing 6.0 km/s and 7.0 km/s contours. Stars represent shot points and numbers. (Top) Elliptical model features that measure 10x5 km are well resolved in the upper 10 km of the crust across the profile, with moderate resolution below 15 km in the middle of the profile and poor resolution below 10 km on the sides and 30 km in the middle of the model. (Middle) Elliptical model features that measure 20x10 km are well resolved in the upper 10 km of the crust across the profile, with moderate resolution below 20 km in the middle of the profile. (Bottom) Elliptical model features that measure 30x15 km are well resolved in throughout the model, except at ~35 km near the middle of the model, around 20 km to 30 km in the western portion of the model, and 15 km to 25 km in the eastern portion of the model.

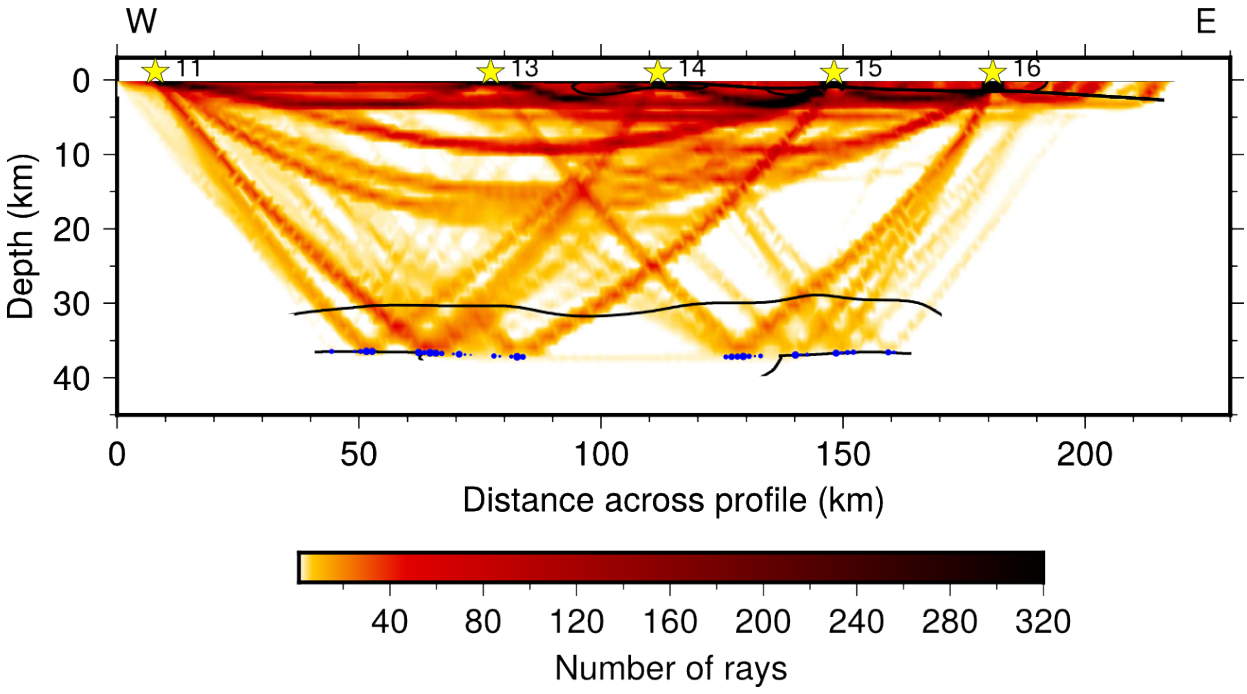

Figure 3: Derivative weight sum (DWS) showing ray coverage across Line 1. The DWS is a nondimensional values used as a proxy for ray density. Stars represent shot points and numbers.

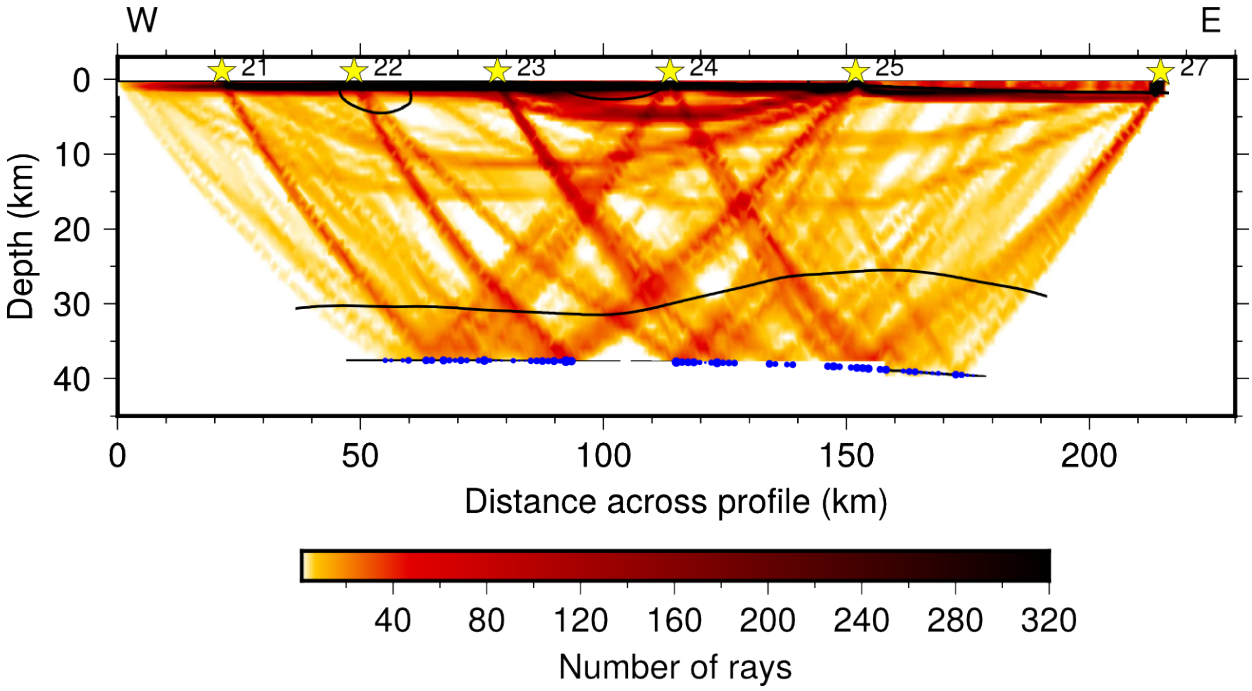

Figure 20: Derivative weight sum (DWS) showing ray coverage across Line 2. The DWS is a nondimensional values used as a proxy for ray density. Stars represent shot points and numbers.

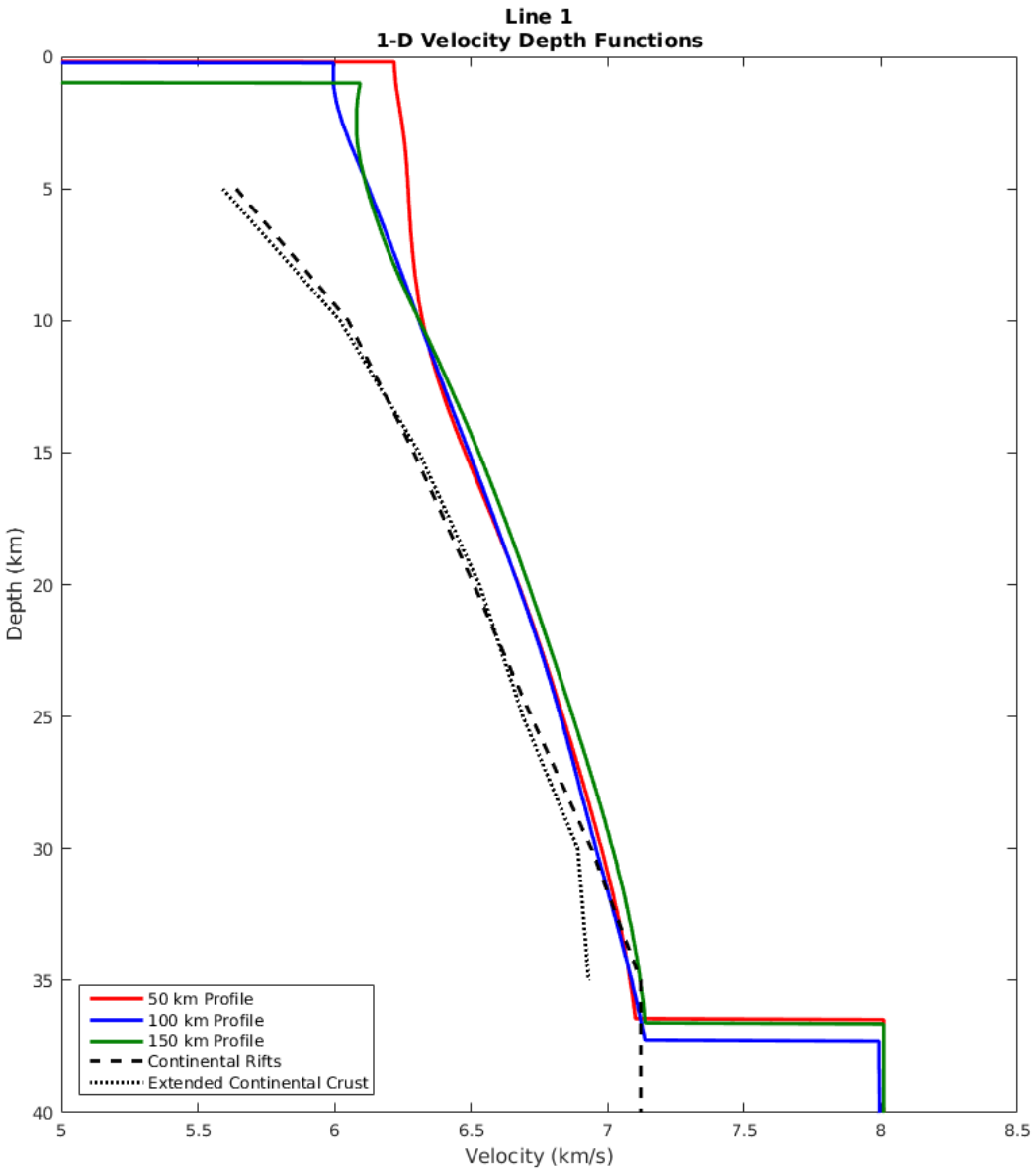

Figure 21: Line 1 1-D velocity profiles extracted at 50 km (red line), 100 km (blue line), and 150 km (green line) distances across the final velocity model. Dashed black line shows average velocities from continental rifts and dotted black line shows average velocities from extended continental crust (Christensen & Mooney, 1995).

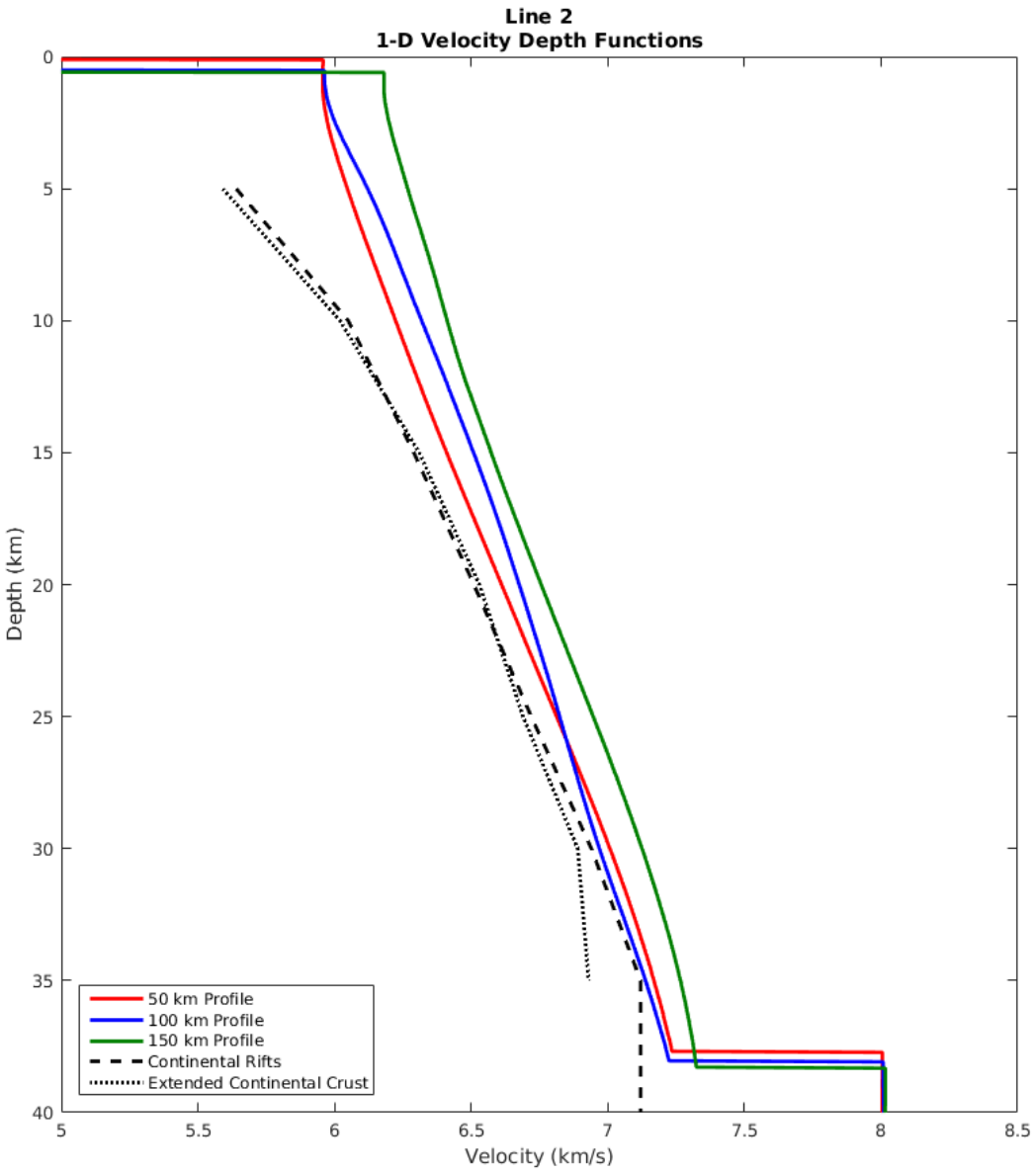

Figure 22: Line 2 1-D velocity profiles extracted at 50 km (red line), 100 km (blue line), and 150 km (green line) distances across the final velocity model. Dashed black line shows average velocities from continental rifts and dotted black line shows average velocities from extended continental crust (Christensen & Mooney, 1995).

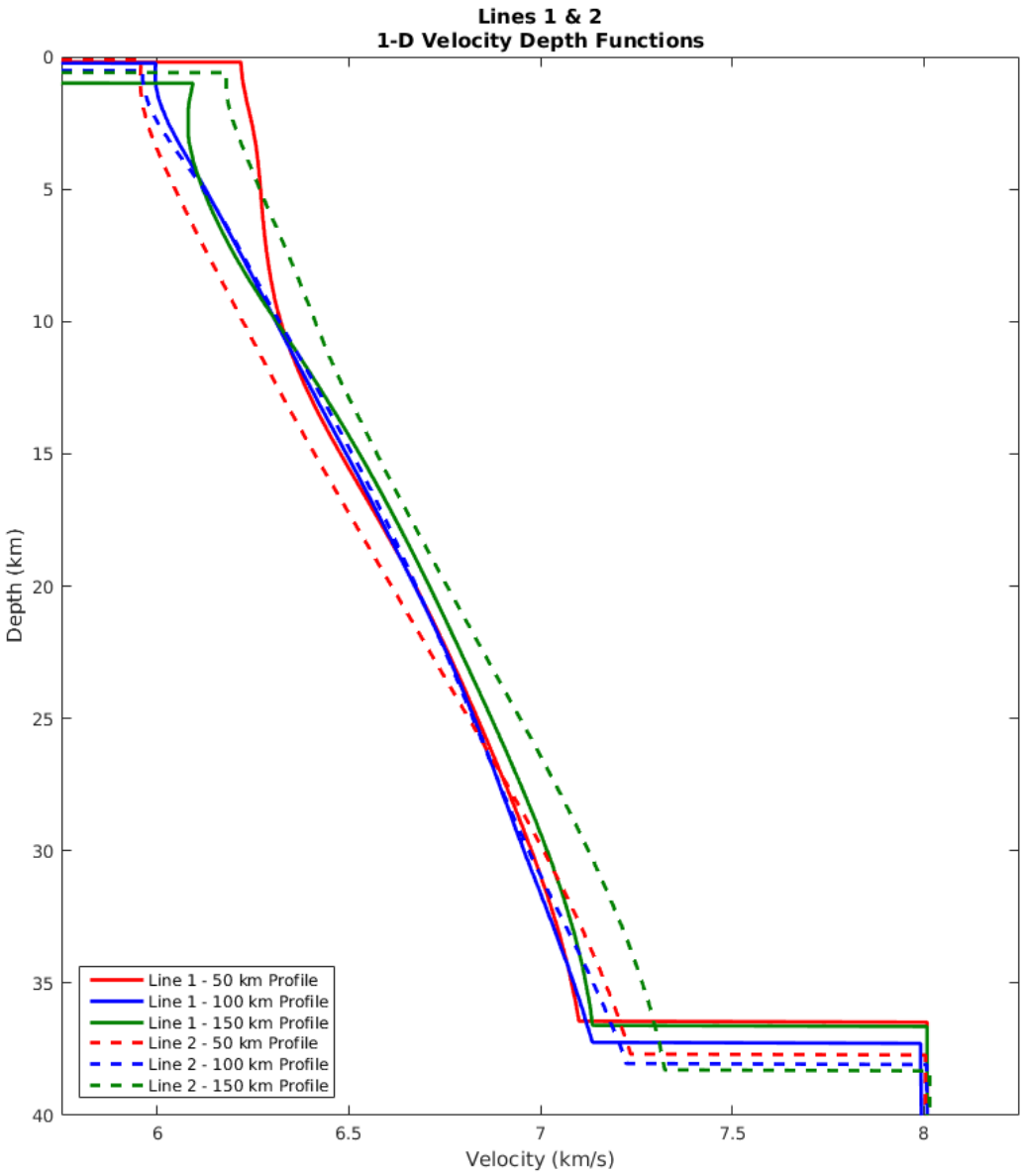

Figure 23: Combined 1-D velocities from figures 22 and 23. Solid lines are profiles from Line 1. Dashed lines are profiles from Line 2.

10 Appendix A: Shot gathers and ray tracing results

10.1 Shot 11, Line 1

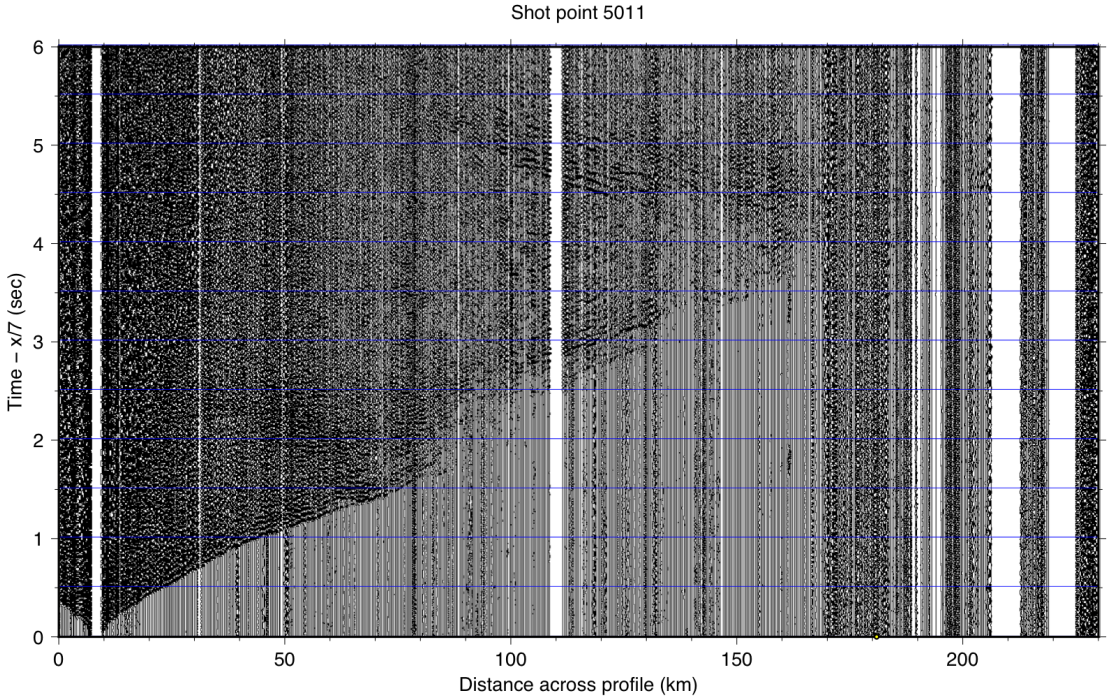

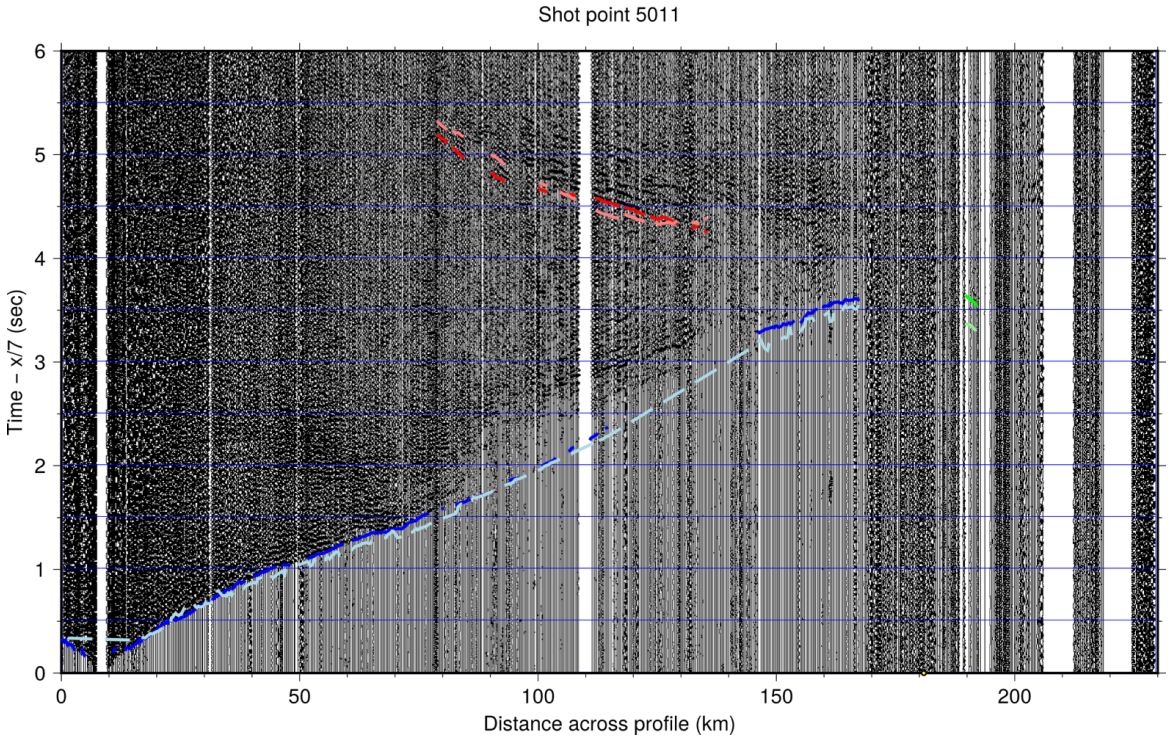

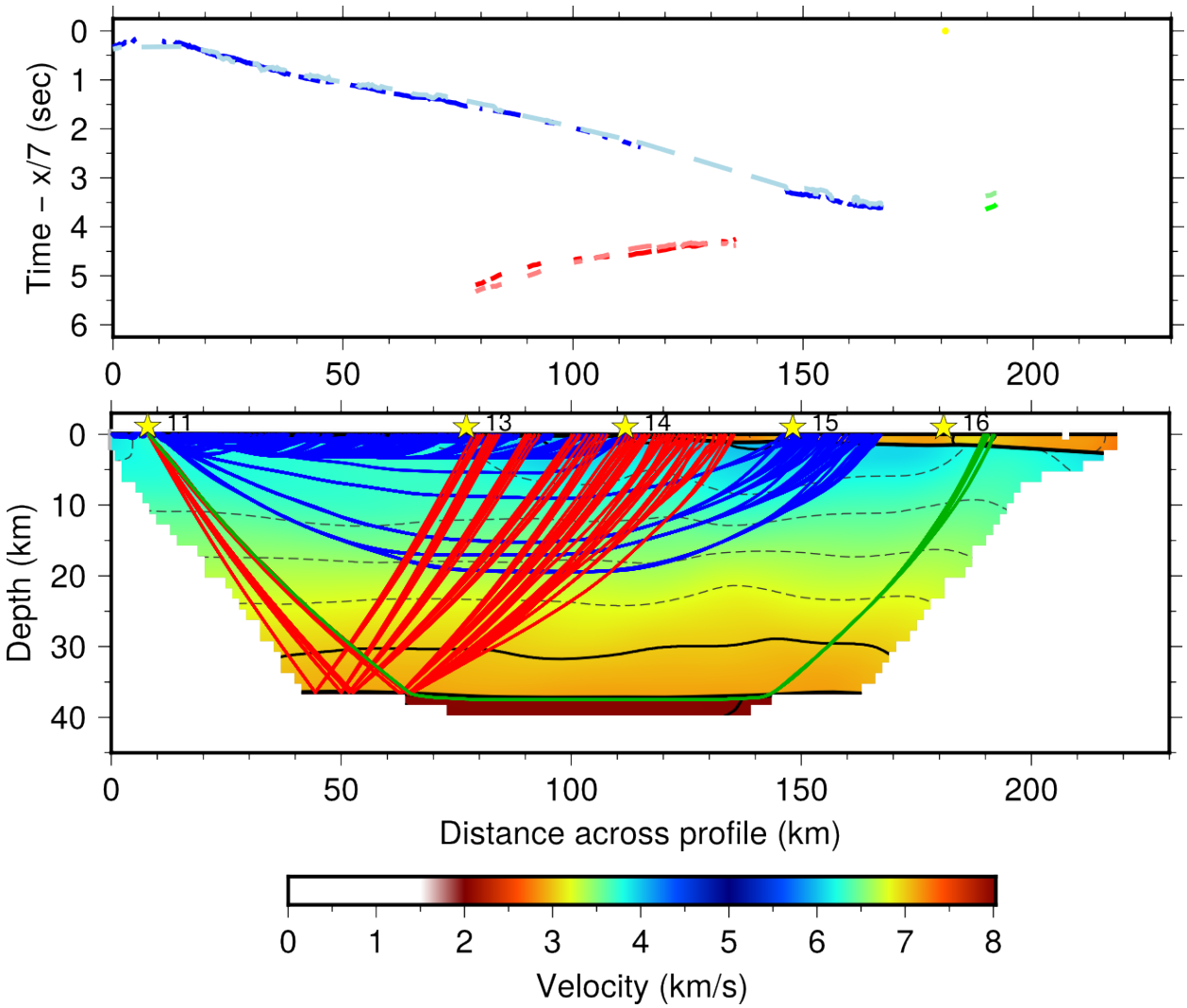
Time – x/7 (sec)
0
1
2
3
4
5
6
0
50
100
150
200
11
13
14
15
16
Depth (km)
0
10
20
30
40
0
50
100
150
200
Distance across profile (km)
0
1
2
3
4
5
6
7
8
Velocity (km/s)

10.2 Shot 13, Line 1

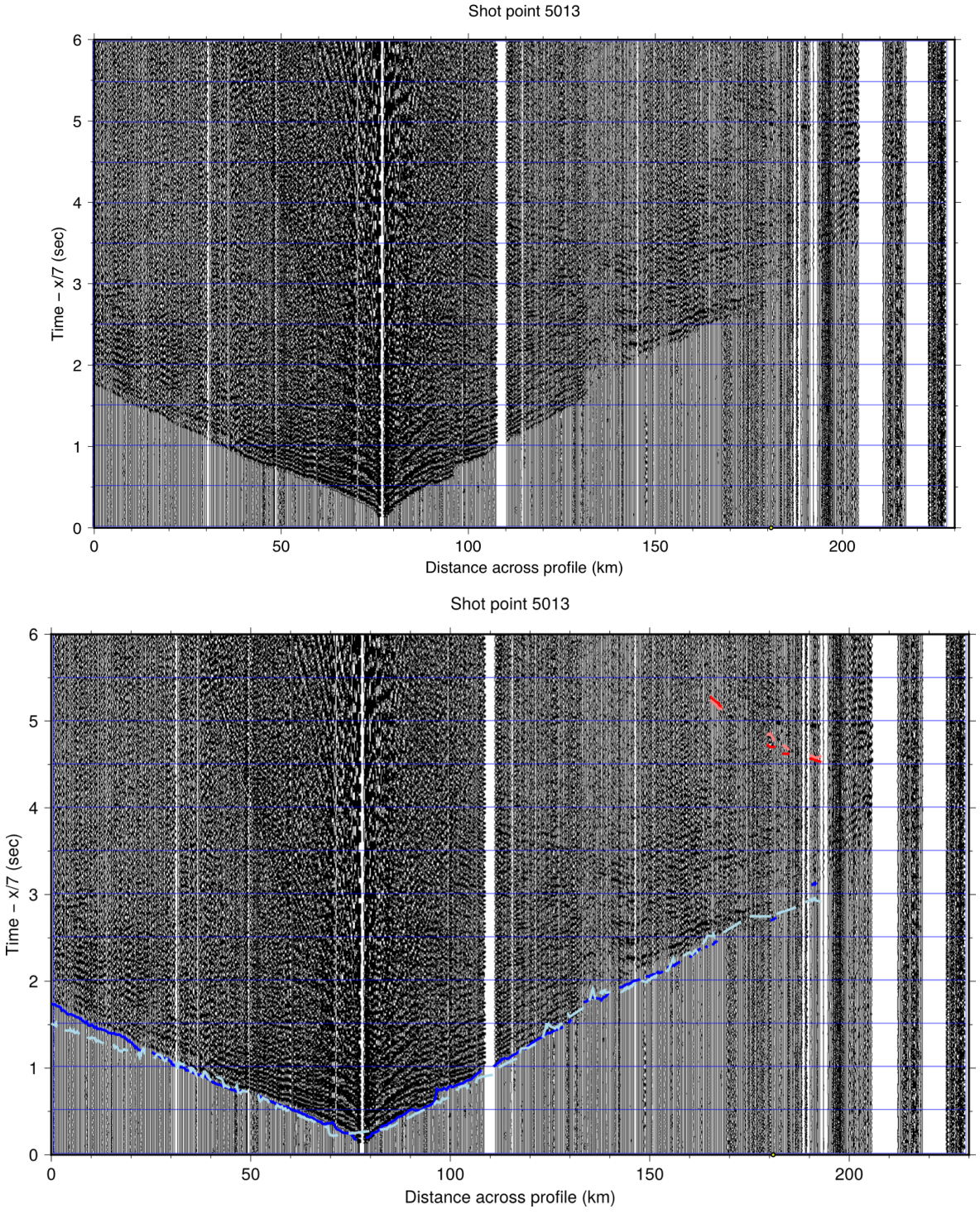

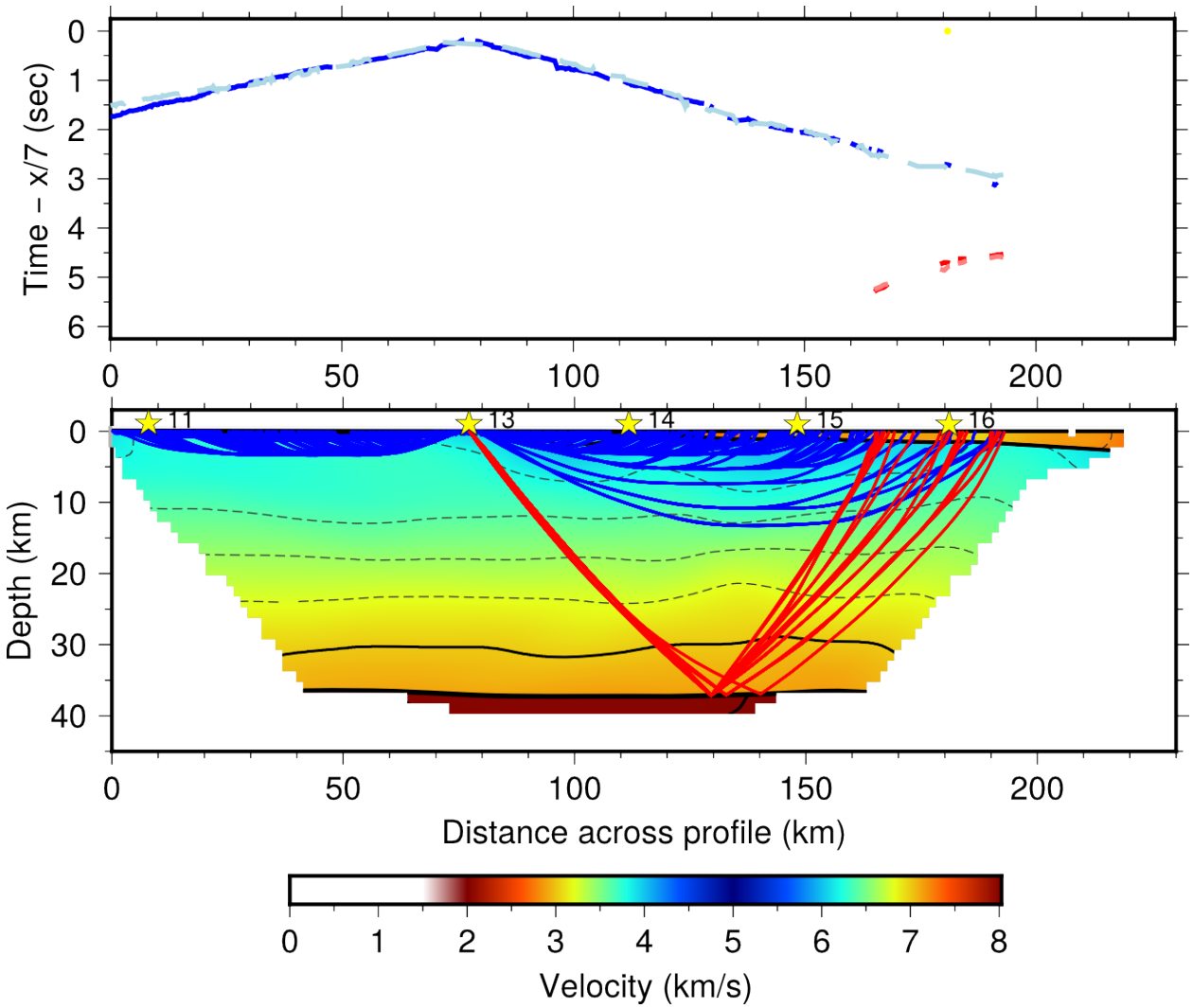
Time – x/7 (sec)
0
1
2
3
4
5
6
0
50
100
150
200
11
13
14
15
16
Depth (km)
0
10
20
30
40
0
50
100
150
200
Distance across profile (km)
0
1
2
3
4
5
6
7
8
Velocity (km/s)

10.3 Shot 14, Line 1

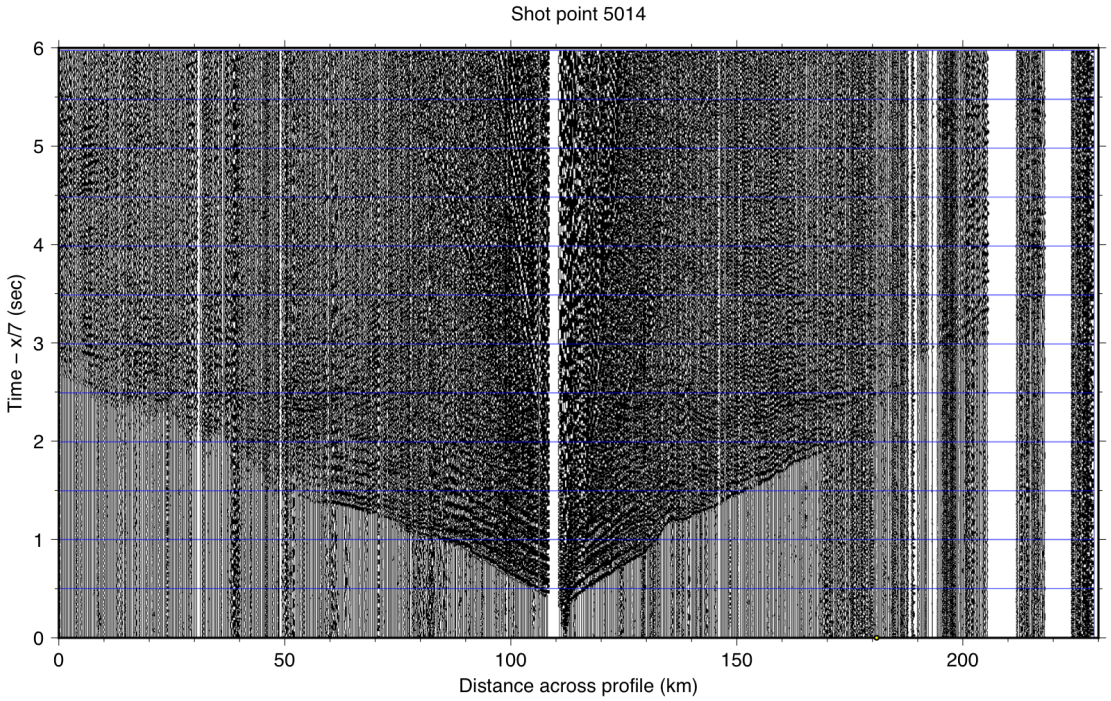

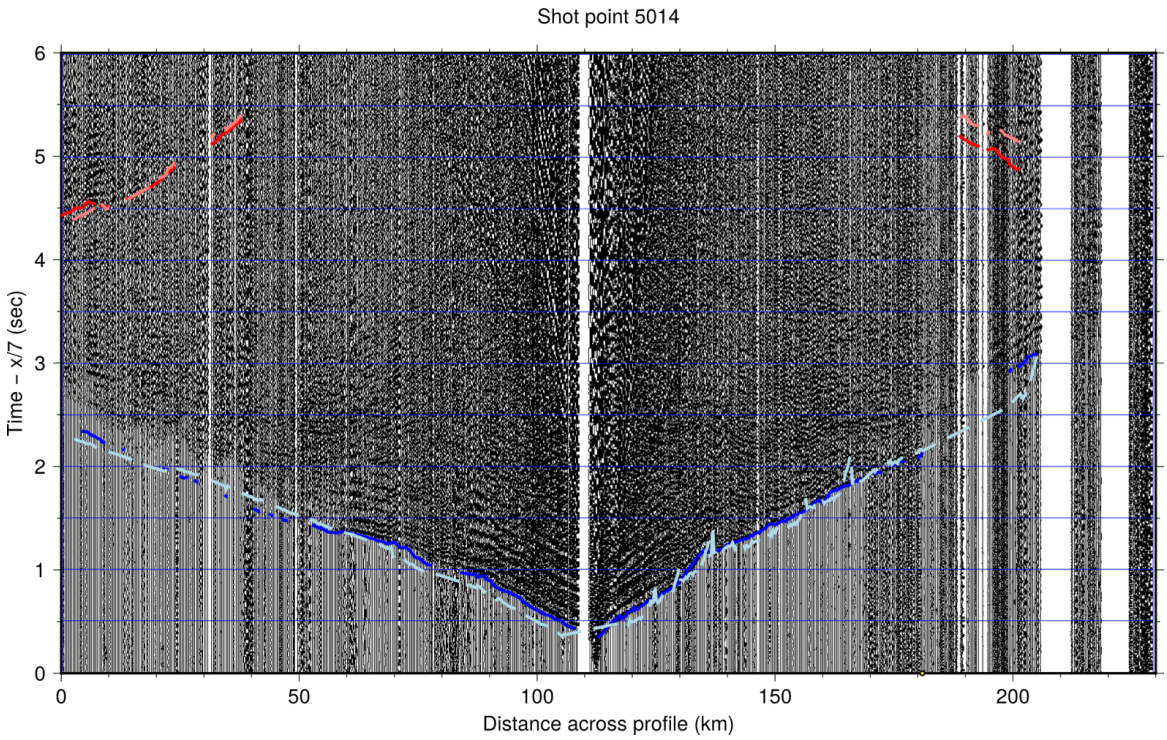

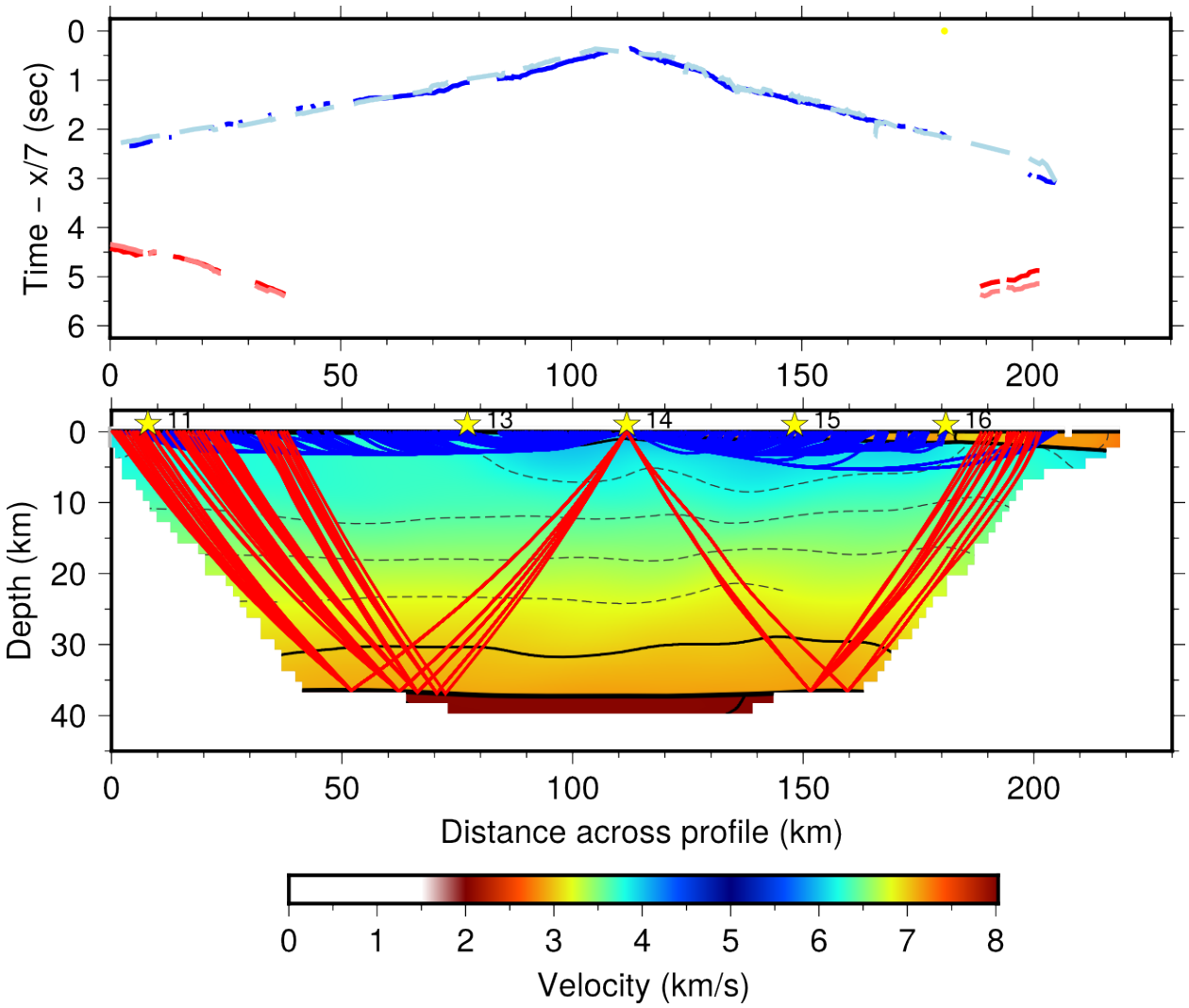
Time – x/7 (sec)
0
1
2
3
4
5
6
0
50
100
150
200
11
13
14
15
16
Depth (km)
0
10
20
30
40
0
50
100
150
200
Distance across profile (km)
0
1
2
3
4
5
6
7
8
Velocity (km/s)

10.4 Shot 15, Line 1

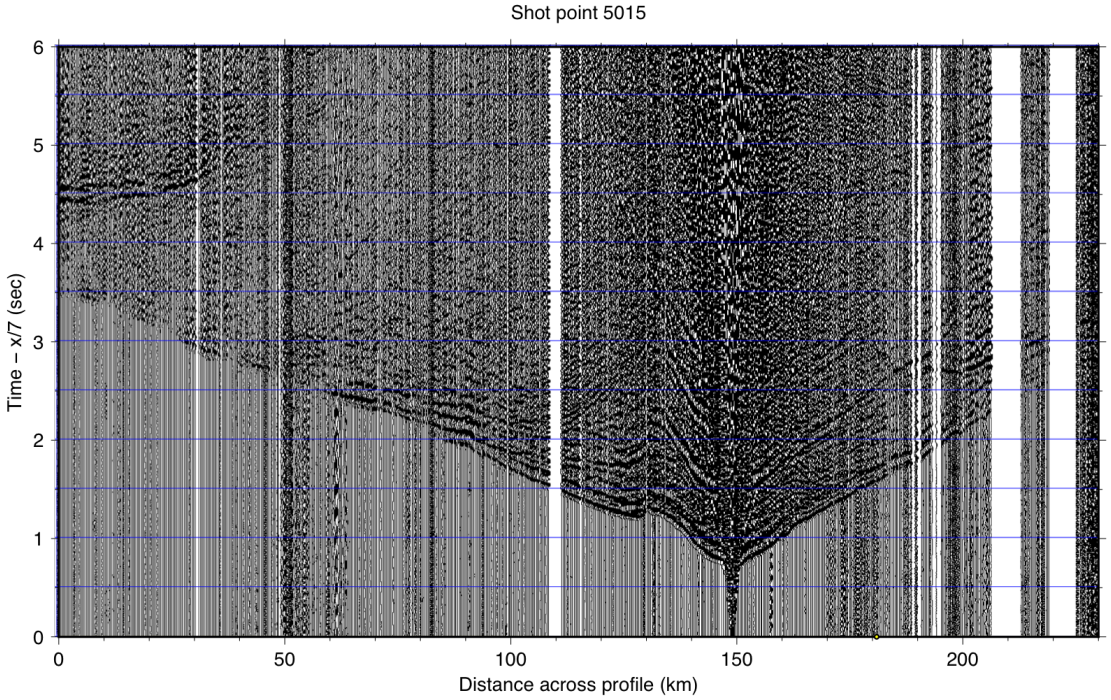

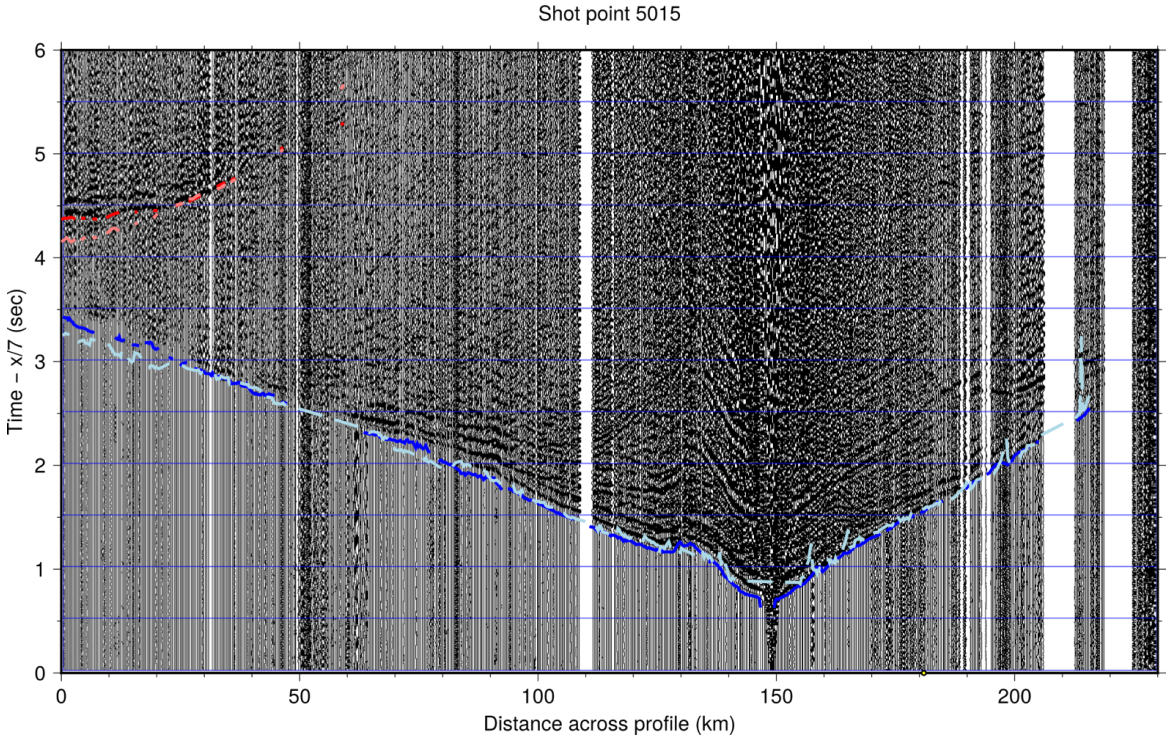

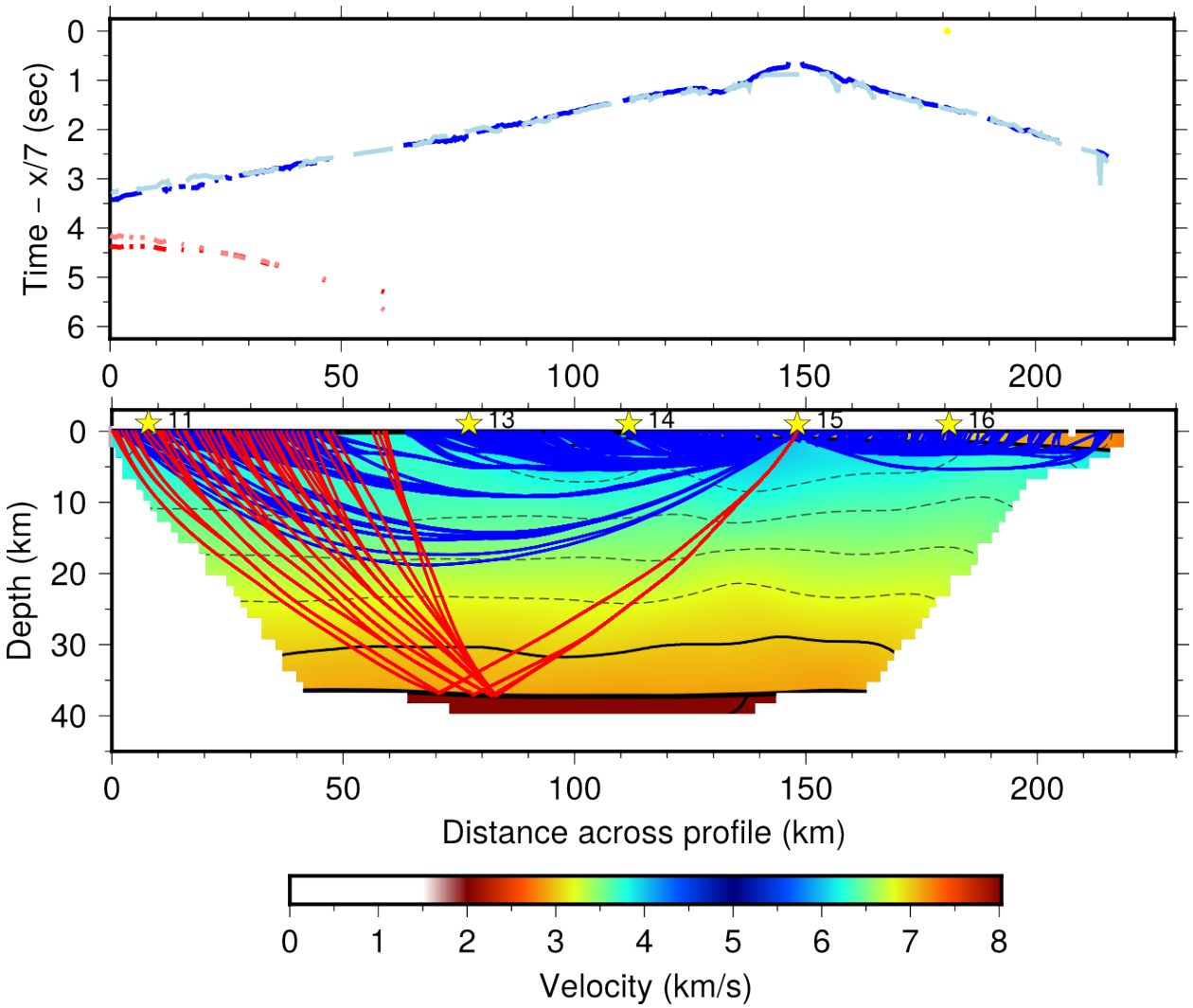
Time – x/7 (sec)
0
1
2
3
4
5
6
0
50
100
150
200
11
13
14
15
16
Depth (km)
0
10
20
30
40
0
50
100
150
200
Distance across profile (km)
0
1
2
3
4
5
6
7
8
Velocity (km/s)

10.5 Shot 16, Line 1

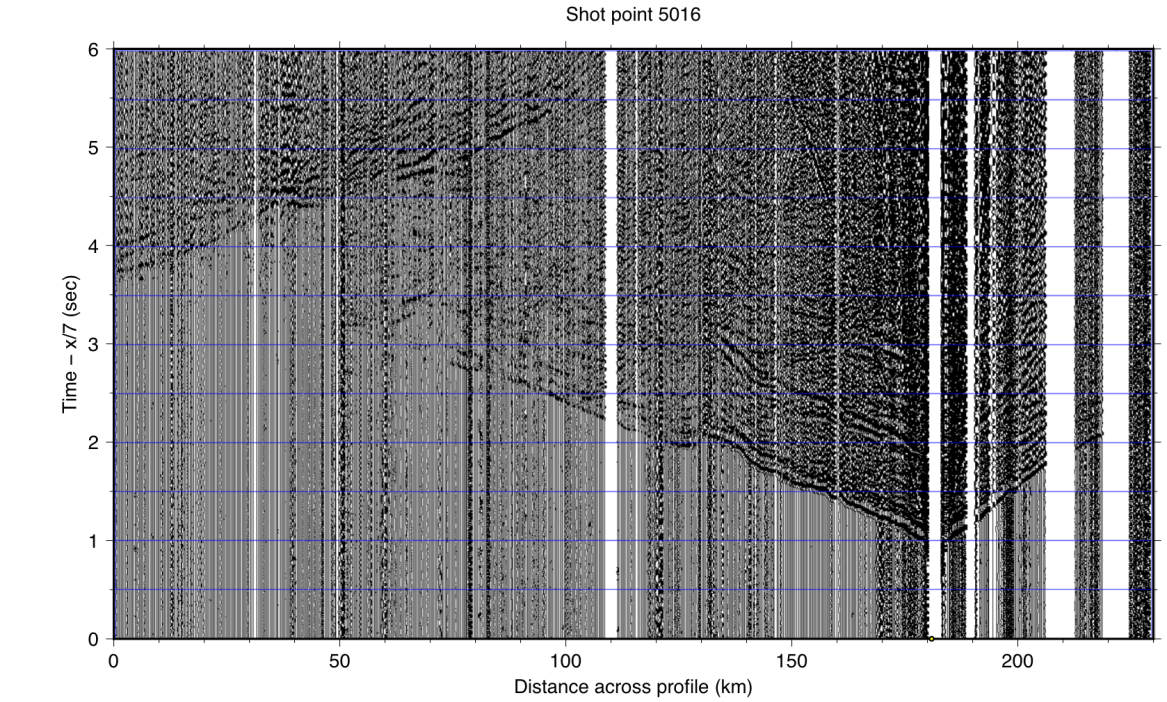

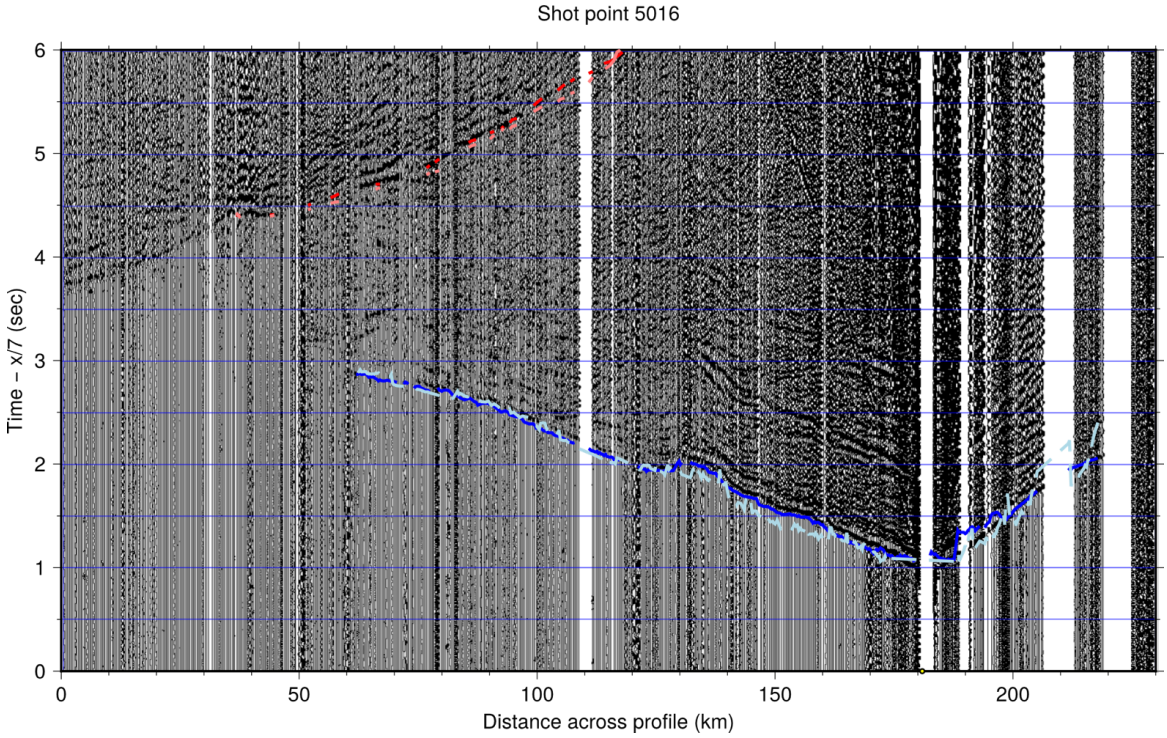

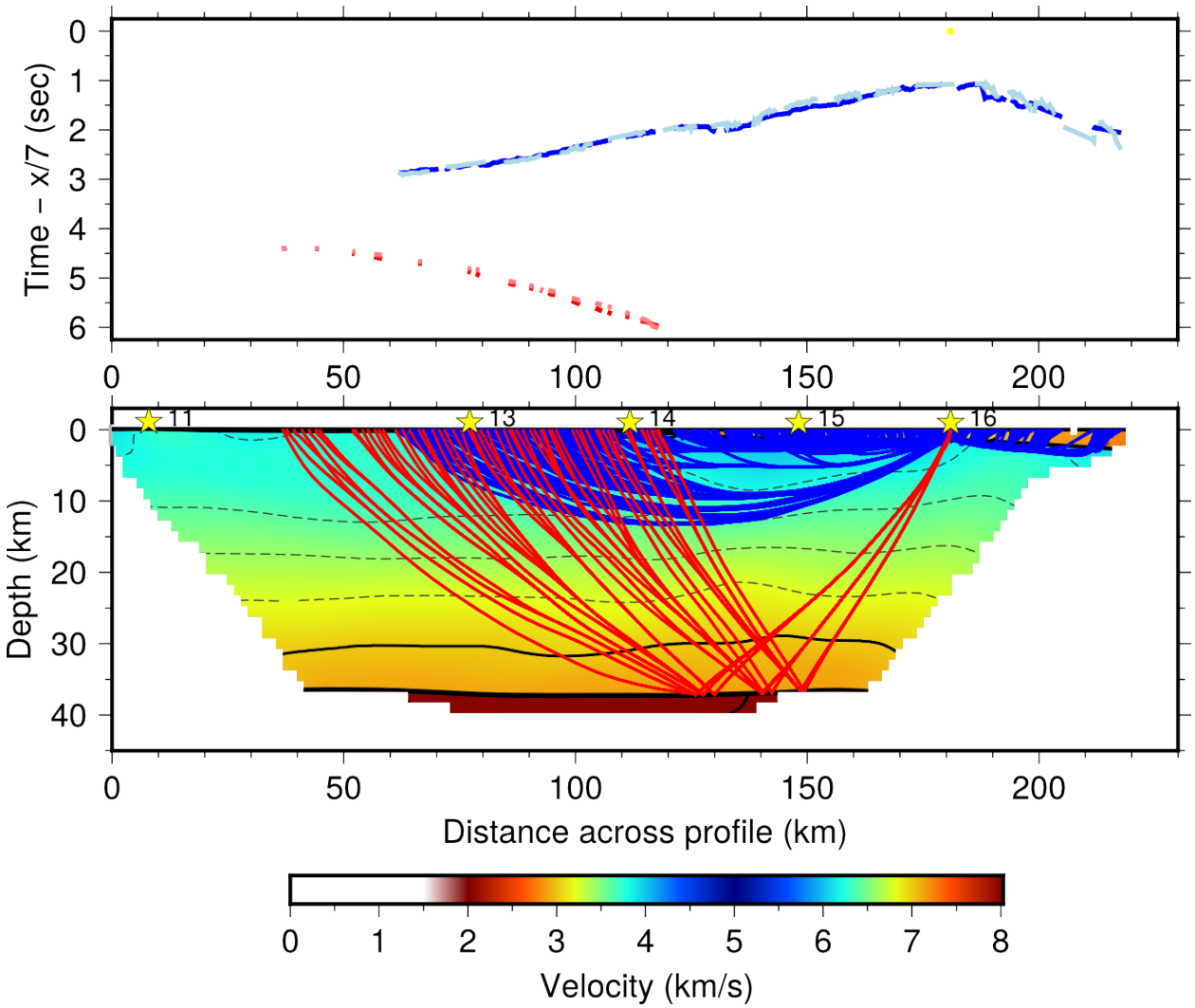
Time – x/7 (sec)
0
1
2
3
4
5
6
0
50
100
150
200
11
13
14
15
16
Depth (km)
0
10
20
30
40
0
50
100
150
200
Distance across profile (km)
0
1
2
3
4
5
6
7
8
Velocity (km/s)

10.6 Shot 21, Line 2

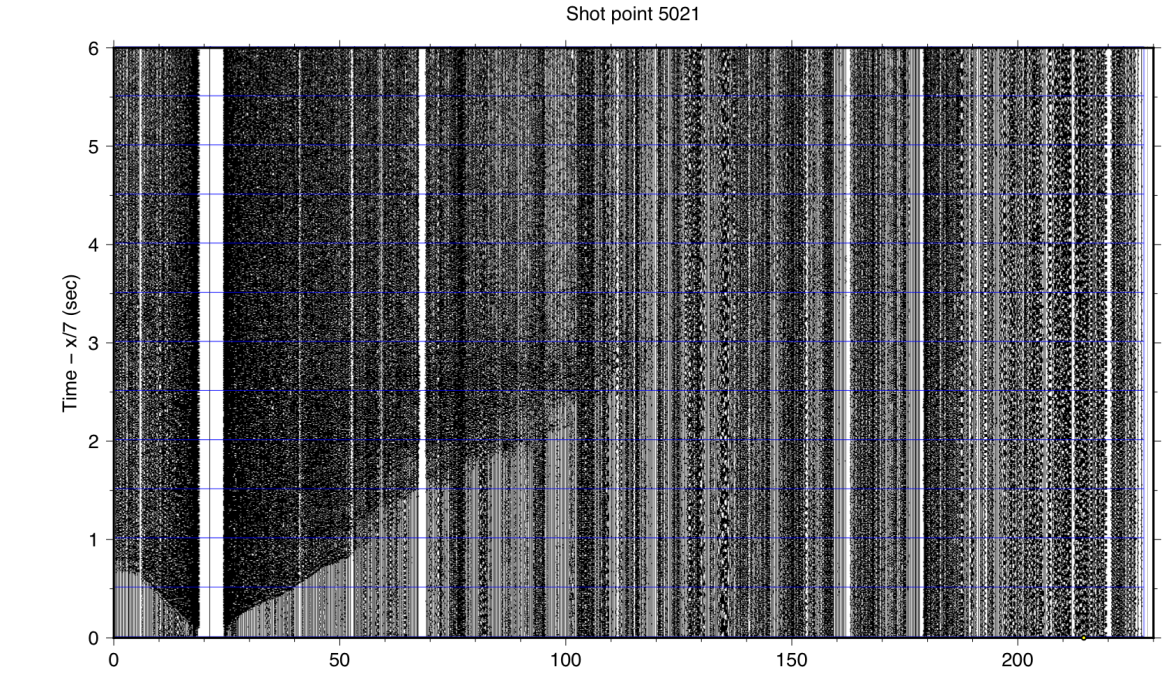

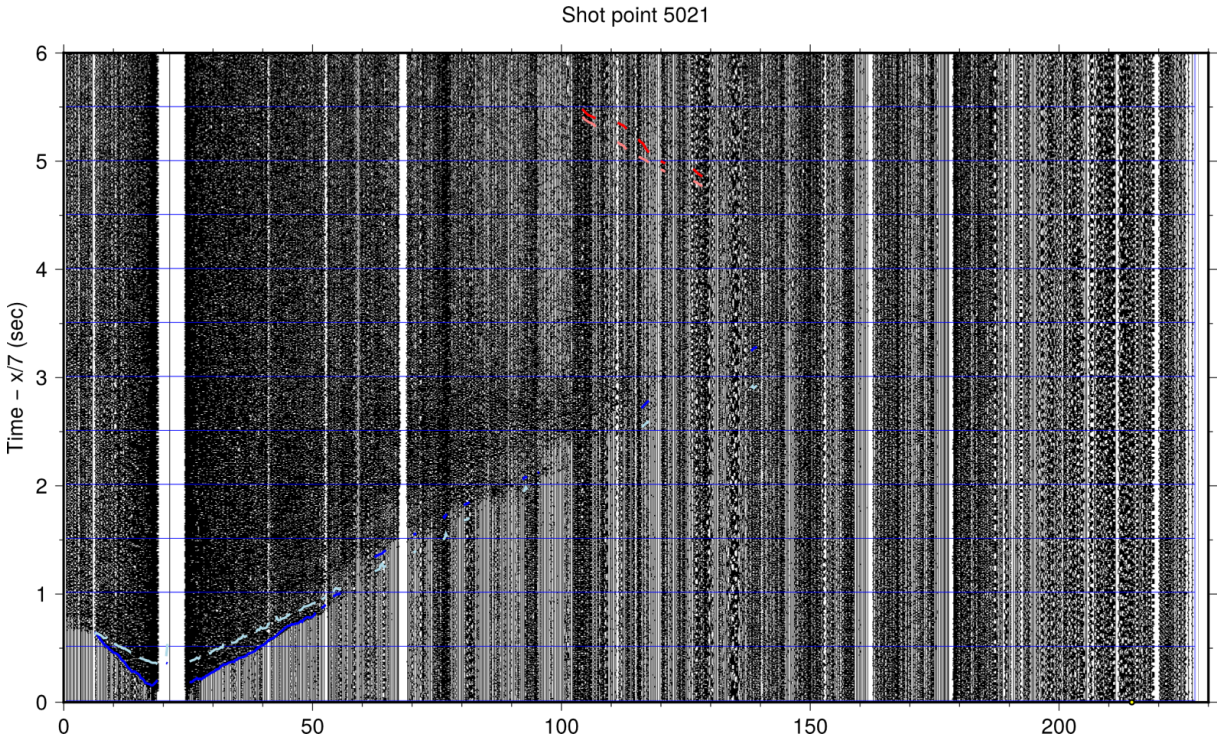

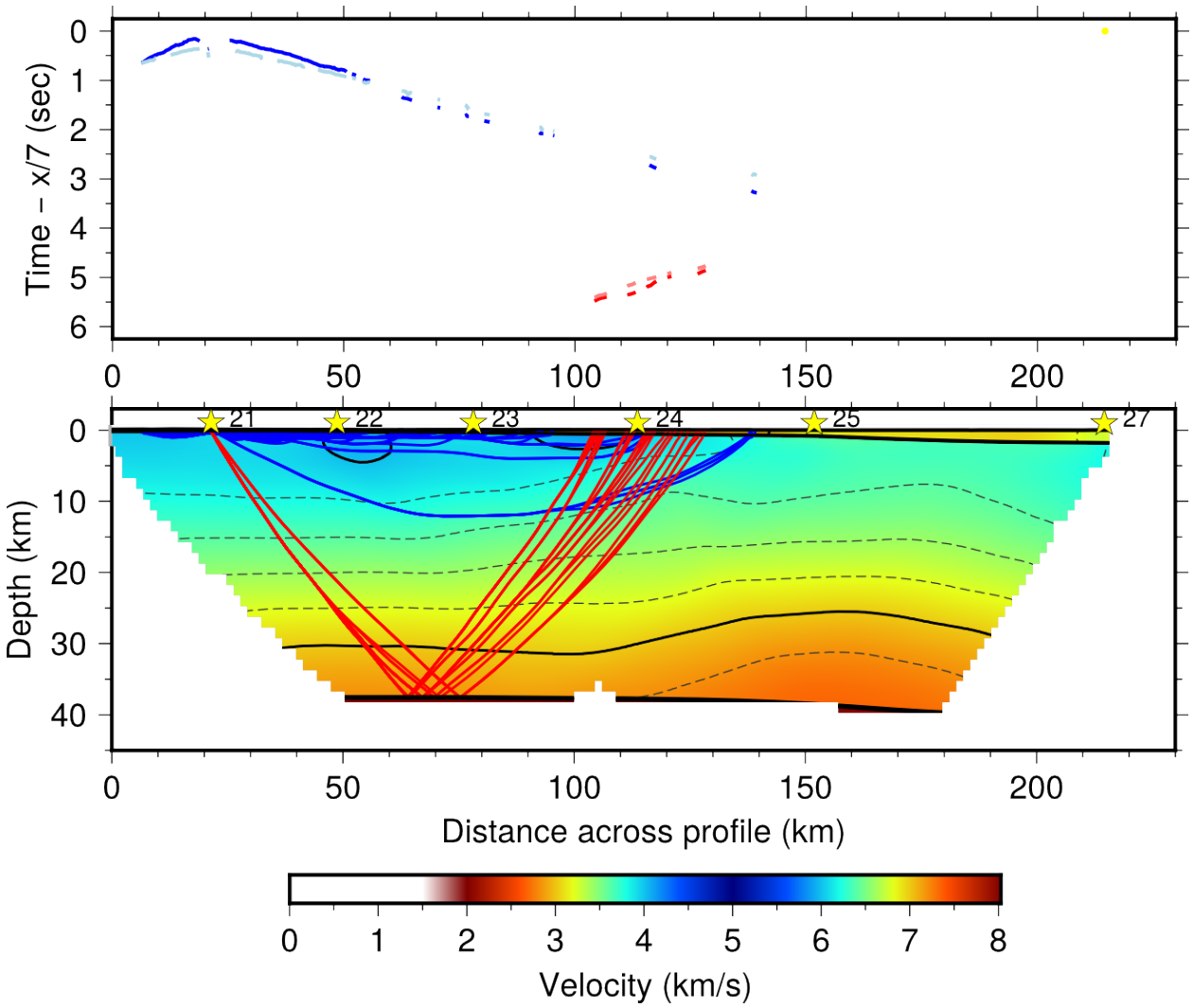
Time – x/7 (sec)
0
1
2
3
4
5
6
0
50
100
150
200
21
22
23
24
25
27
Depth (km)
0
10
20
30
40
0
50
100
150
200
Distance across profile (km)
0
1
2
3
4
5
6
7
8
Velocity (km/s)

10.7 Shot 22, Line 2

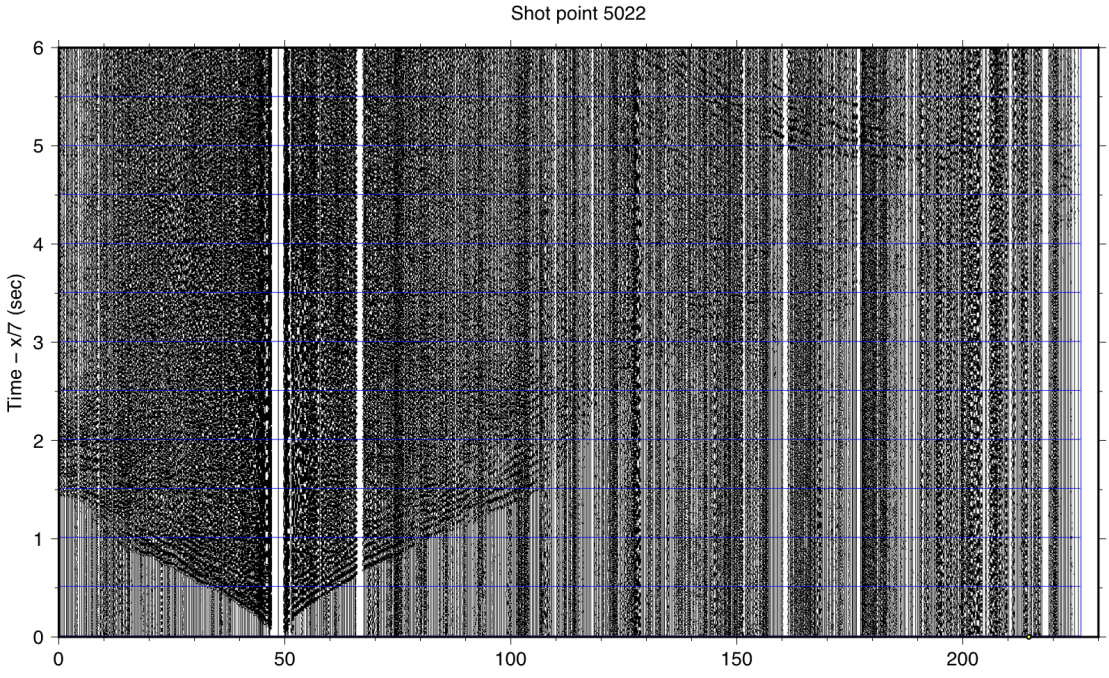

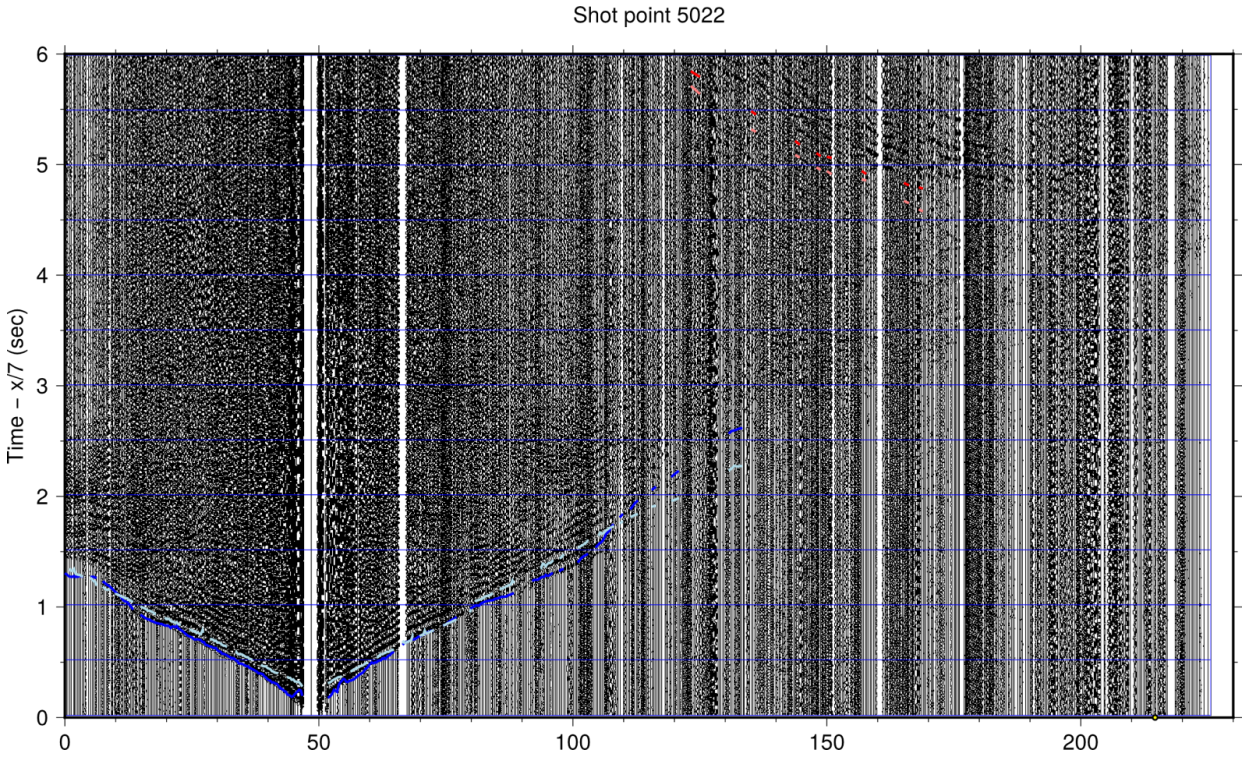

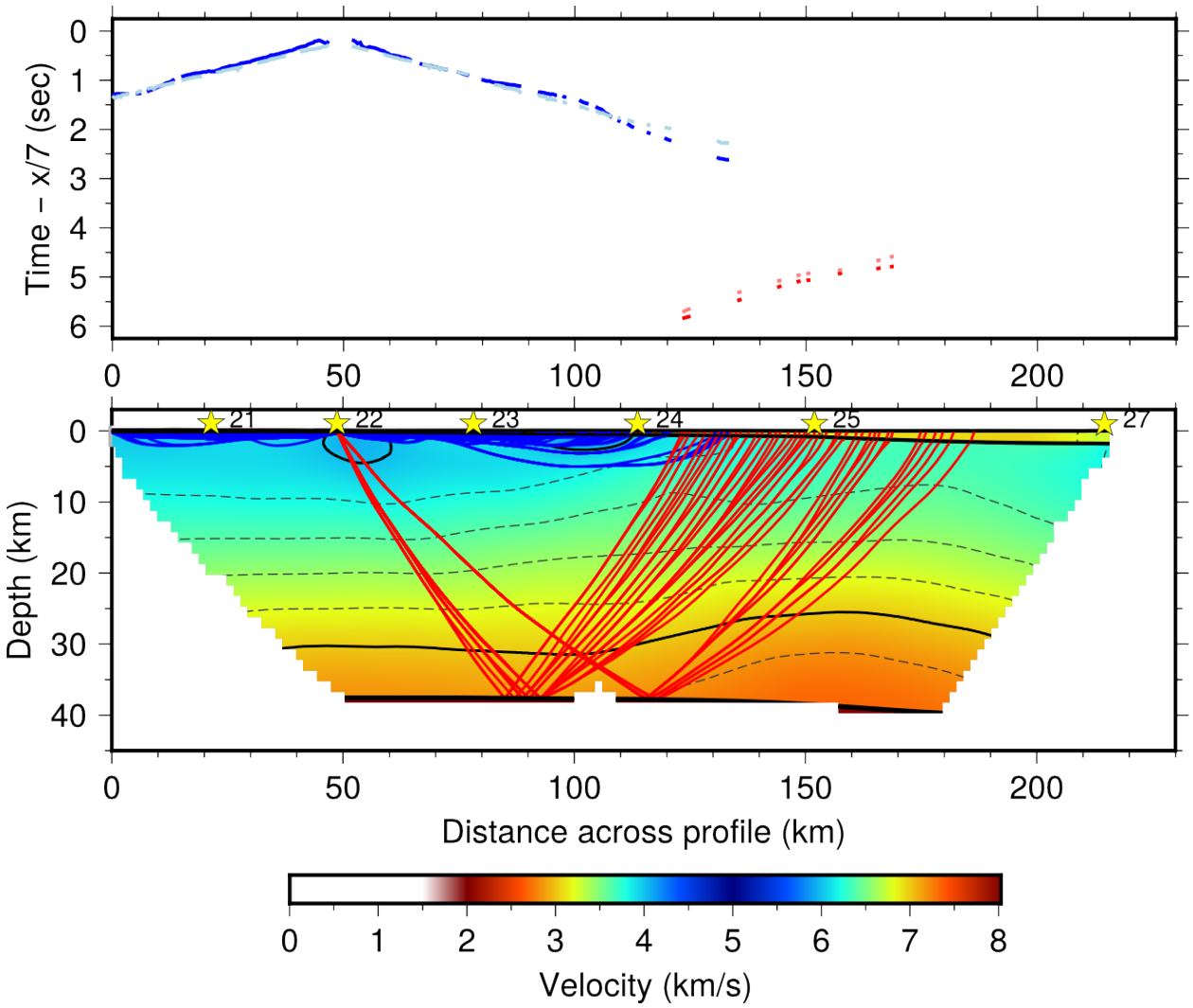
Time – x/7 (sec)
0
1
2
3
4
5
6
0
50
100
150
200
21
22
23
24
25
27
Depth (km)
0
10
20
30
40
0
50
100
150
200
Distance across profile (km)
0
1
2
3
4
5
6
7
8
Velocity (km/s)

10.8 Shot 23, Line 2

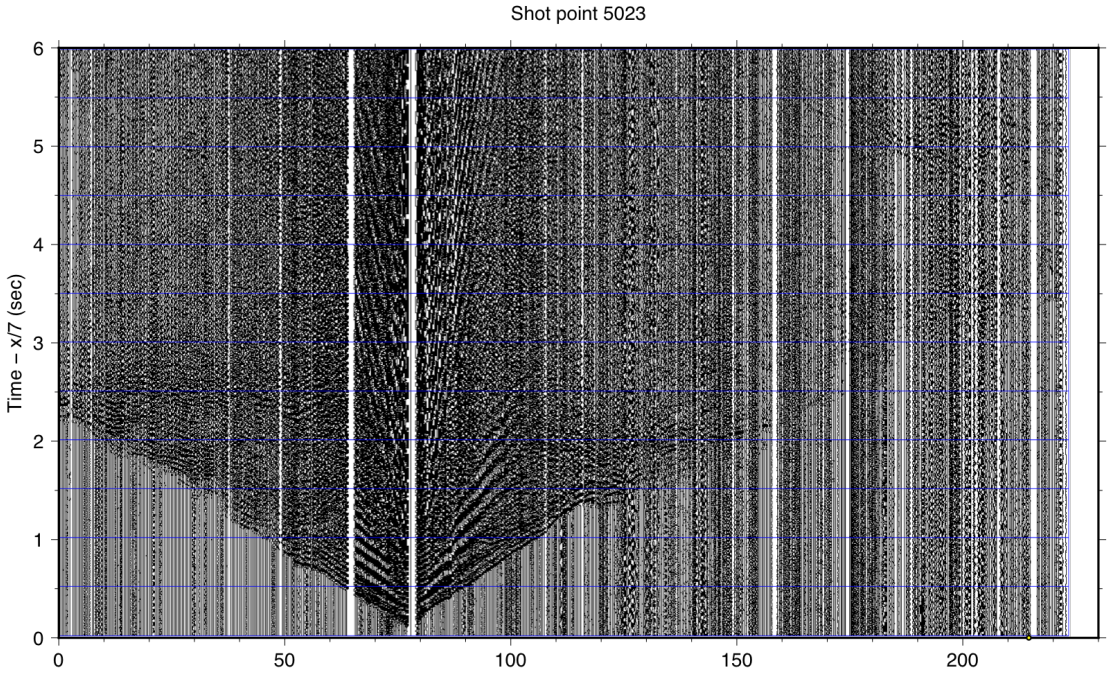

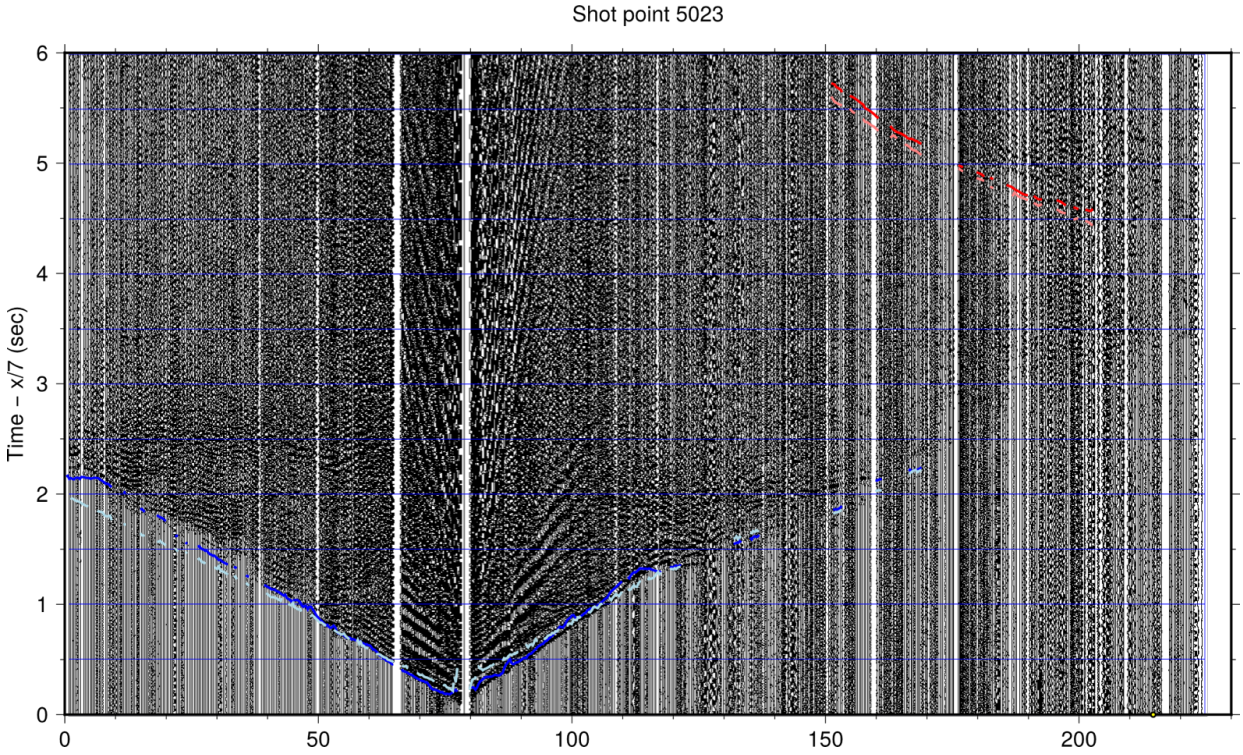

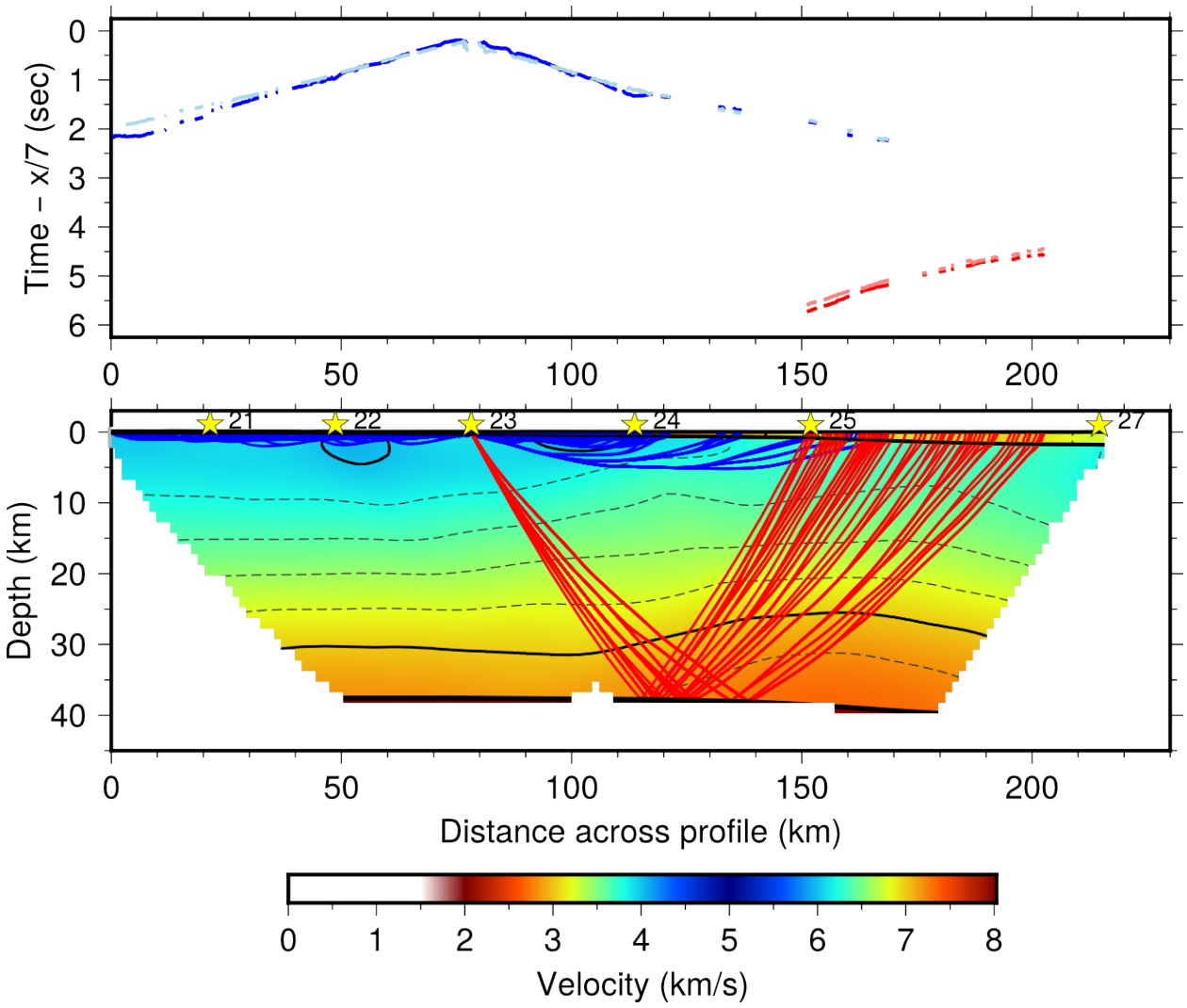
Time – x/7 (sec)
0
1
2
3
4
5
6
0
50
100
150
200
21
22
23
24
25
27
Depth (km)
0
10
20
30
40
0
50
100
150
200
Distance across profile (km)
0
1
2
3
4
5
6
7
8
Velocity (km/s)

10.9 Shot 24, Line 2

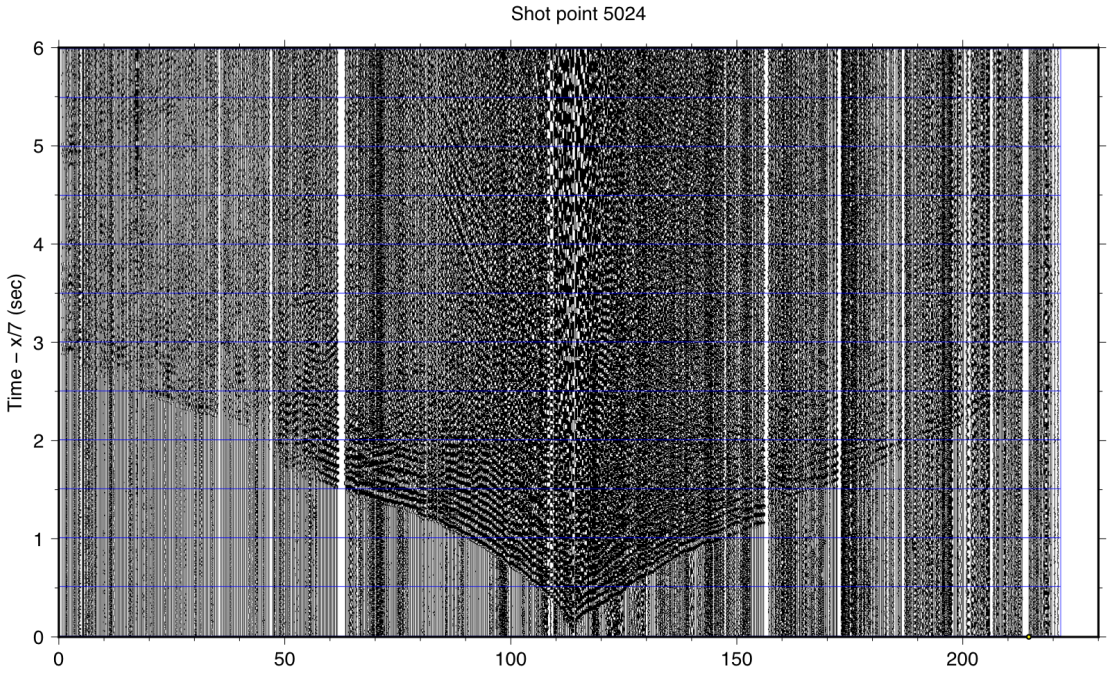

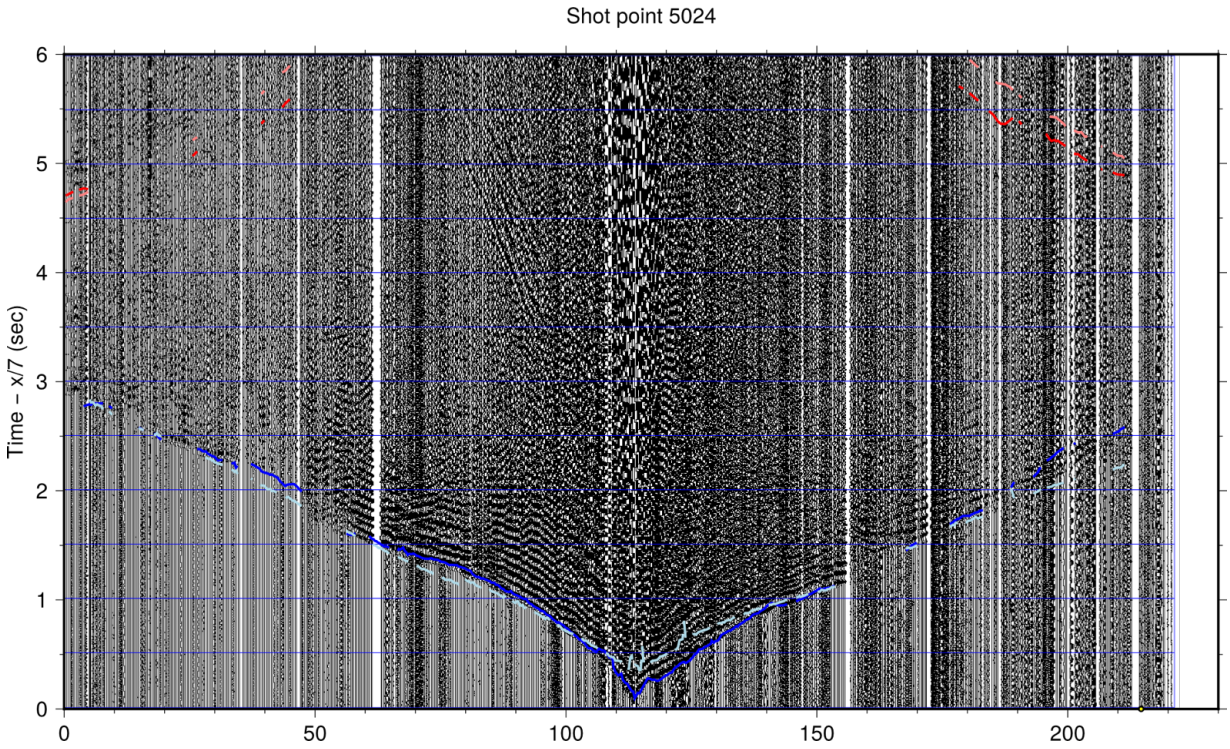

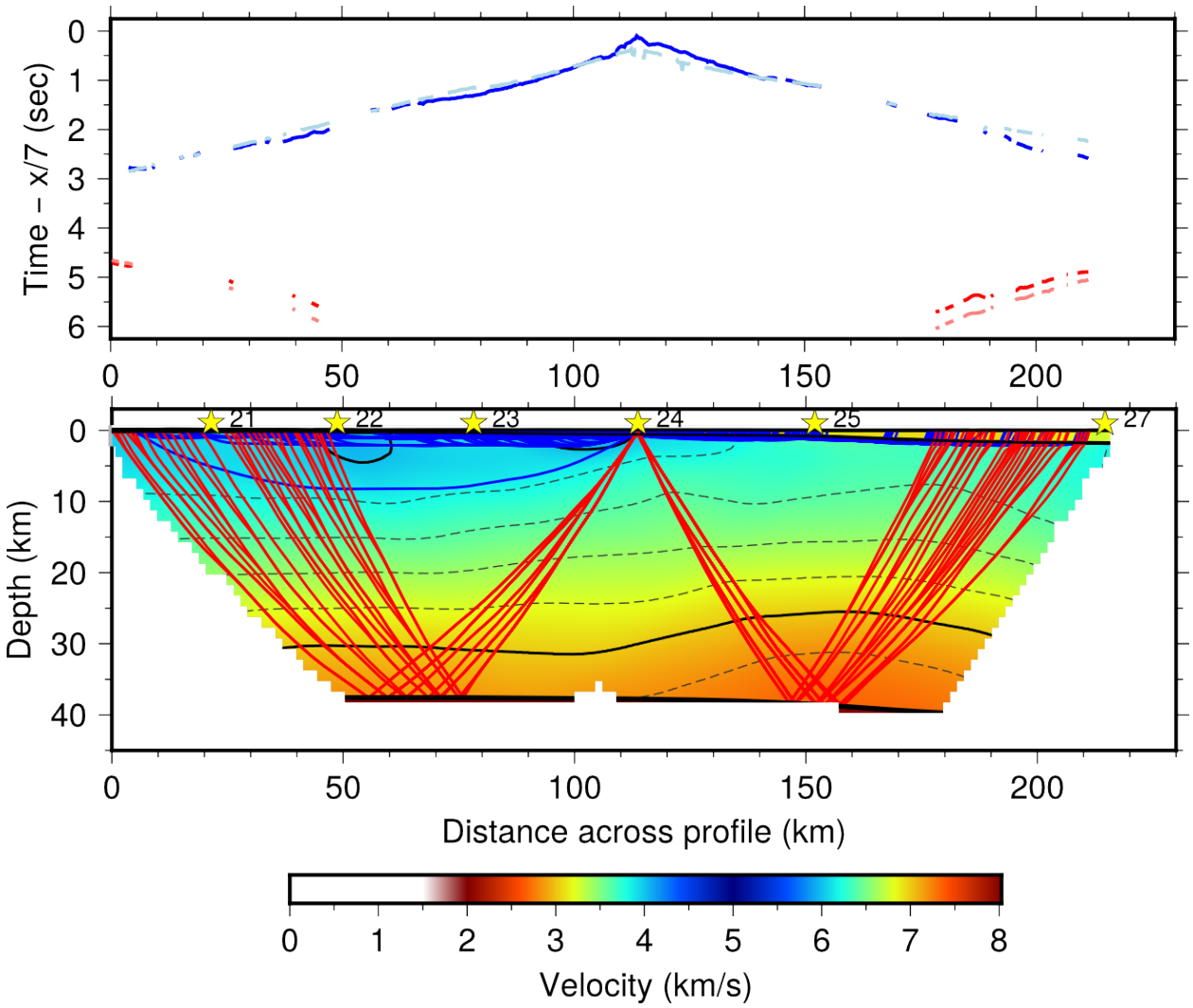
Time – x/7 (sec)
0
1
2
3
4
5
6
0
50
100
150
200
Depth (km)
0
10
20
30
40
21
22
23
24
25
27
Distance across profile (km)
0
1
2
3
4
5
6
7
8
Velocity (km/s)

10.10 Shot 25, Line 2

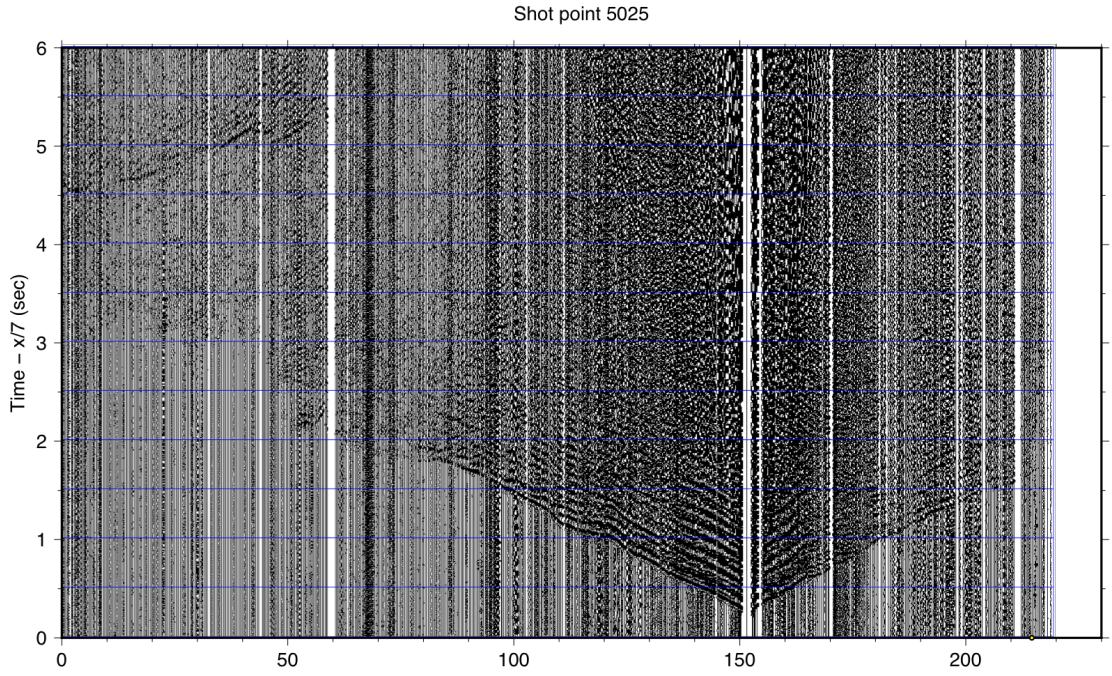

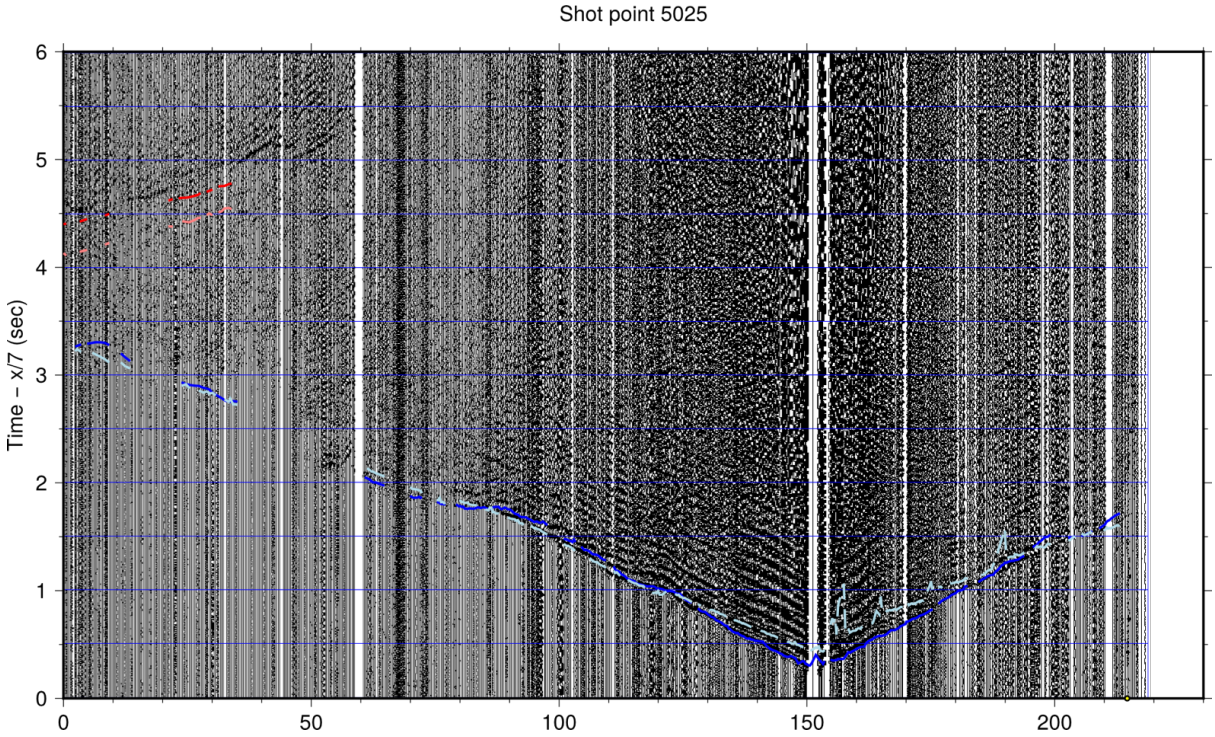

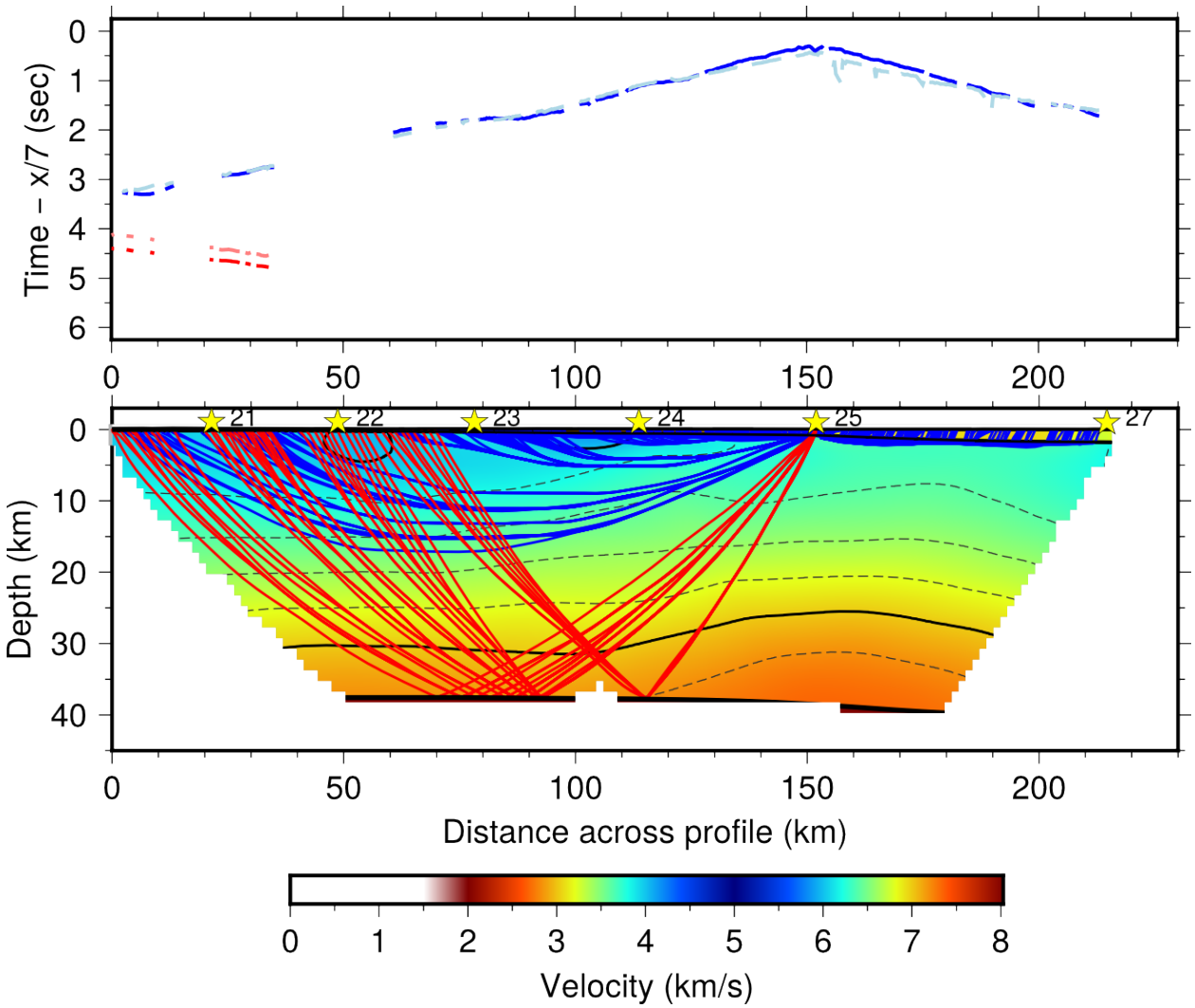
Time – x/7 (sec)
0
1
2
3
4
5
6
0
50
100
150
200
21
22
23
24
25
27
Depth (km)
0
10
20
30
40
0
50
100
150
200
Distance across profile (km)
0
1
2
3
4
5
6
7
8
Velocity (km/s)

10.11 Shot 27, Line 2

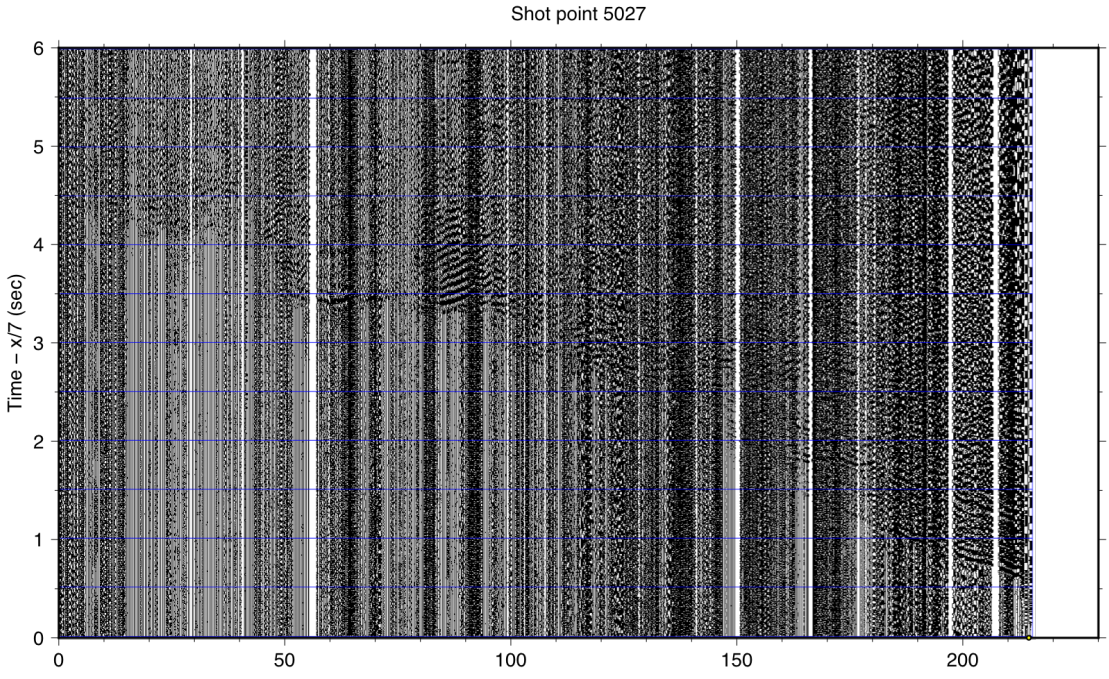

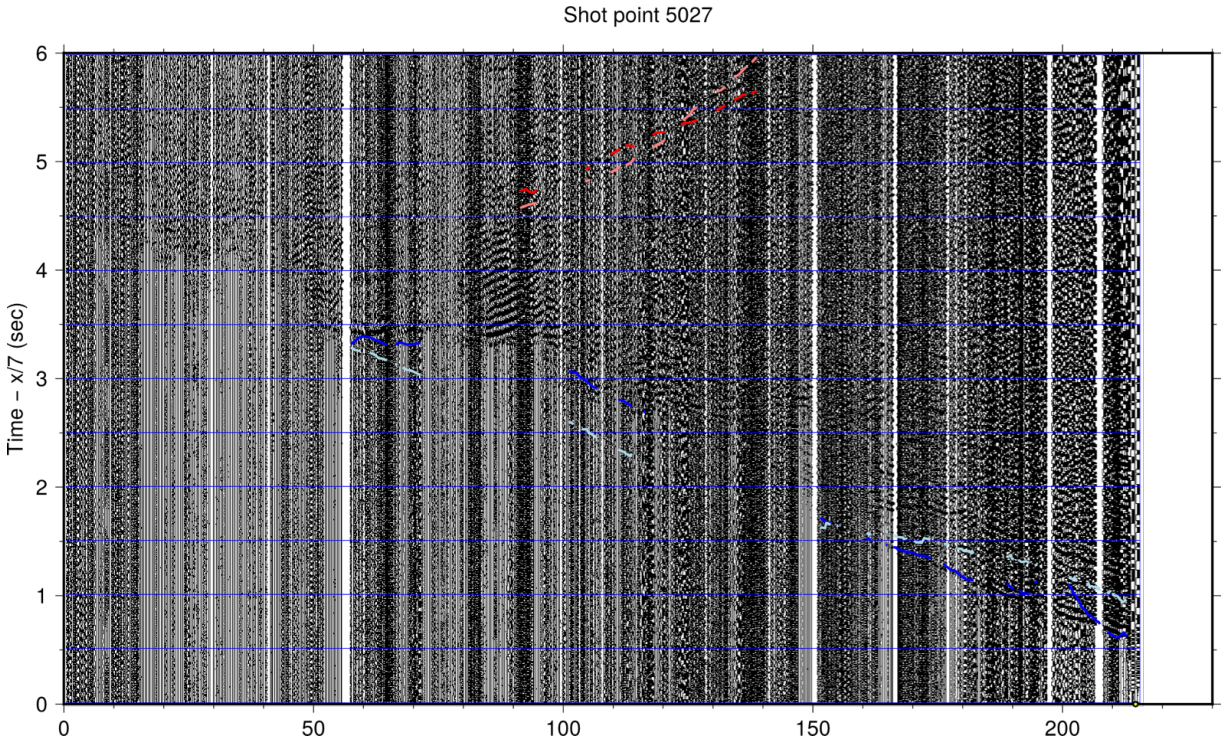

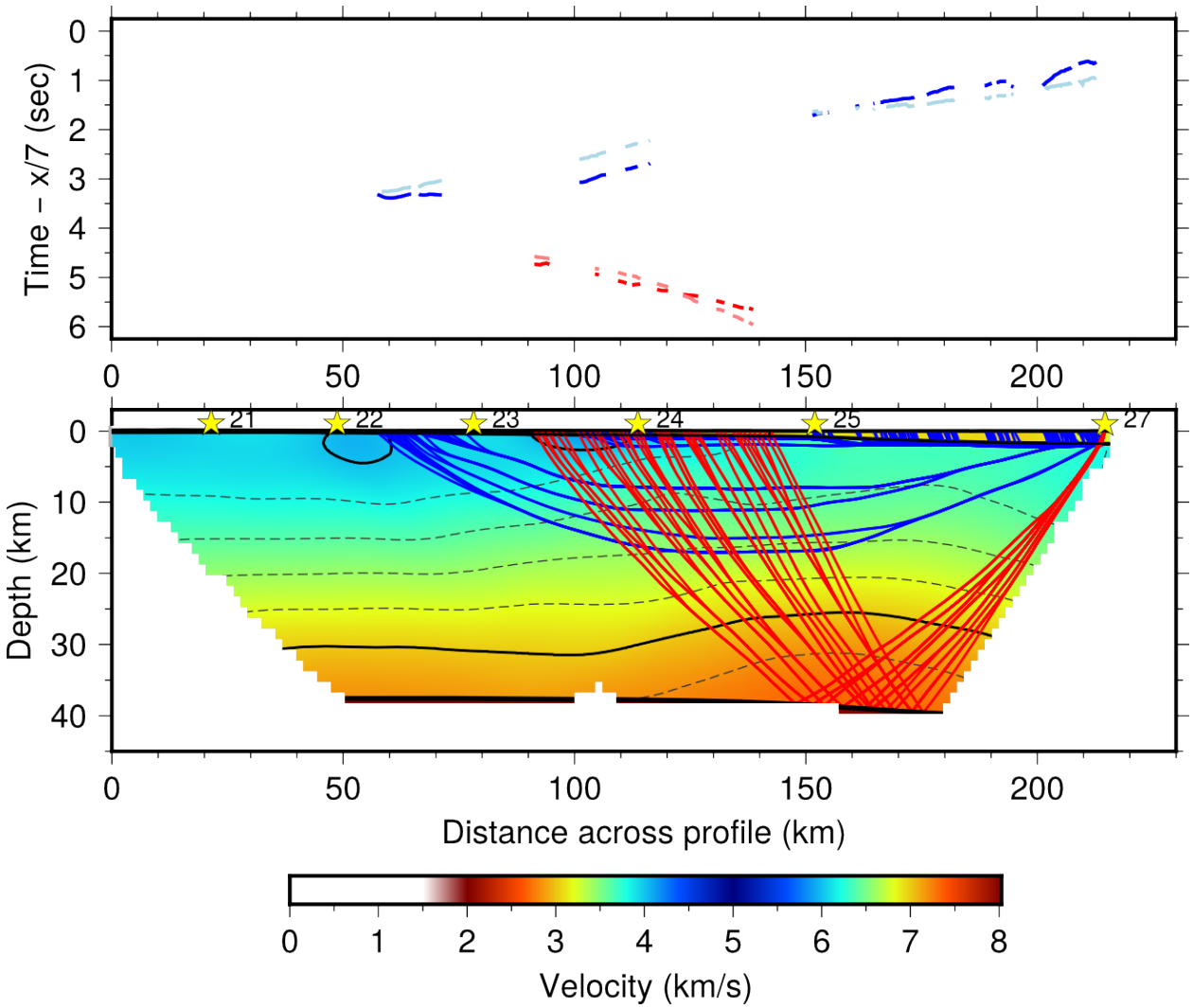
Time – x/7 (sec)
0
1
2
3
4
5
6
0
50
100
150
200
21
22
23
24
25
27
Depth (km)
0
10
20
30
40
0
50
100
150
200
Distance across profile (km)
0
1
2
3
4
5
6
7
8
Velocity (km/s)

11 Appendix B: Resolution test results

11.1 Line 1

Resolution of seismic velocity variations and layer boundary depth at varying scales for Line 1. Stars represent shot points and numbers. (Top) Elliptical model features that measure 10x5 km are well resolved in the upper 10 km of the crust across the profile, with moderate resolution below 15 km in the middle of the profile and poor resolution below 10 km on the sides and 30 km in the middle of the model. (Middle) Elliptical model features that measure 20x10 km are well resolved in the upper 10 km of the crust across the profile, with moderate resolution below 20 km in the middle of the profile. (Bottom) Elliptical model features that measure 30x15 km are well resolved in throughout the model, except around 35 km depth in the middle of the model and between 15 km and 30 km in the eastern portion of the model.

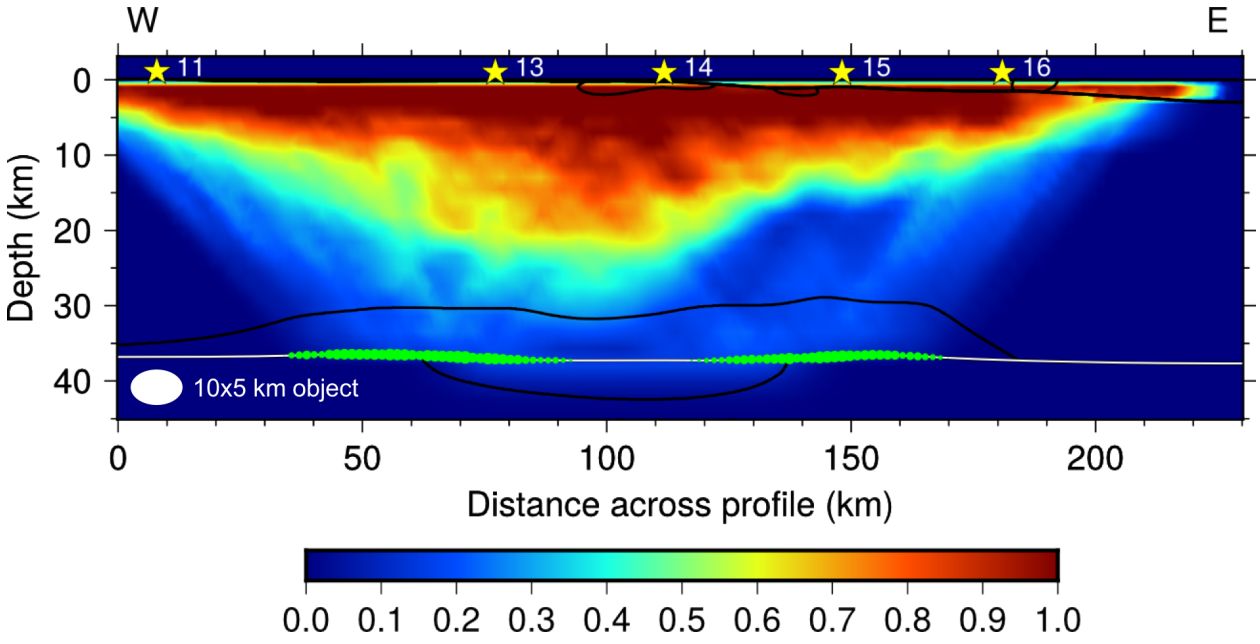

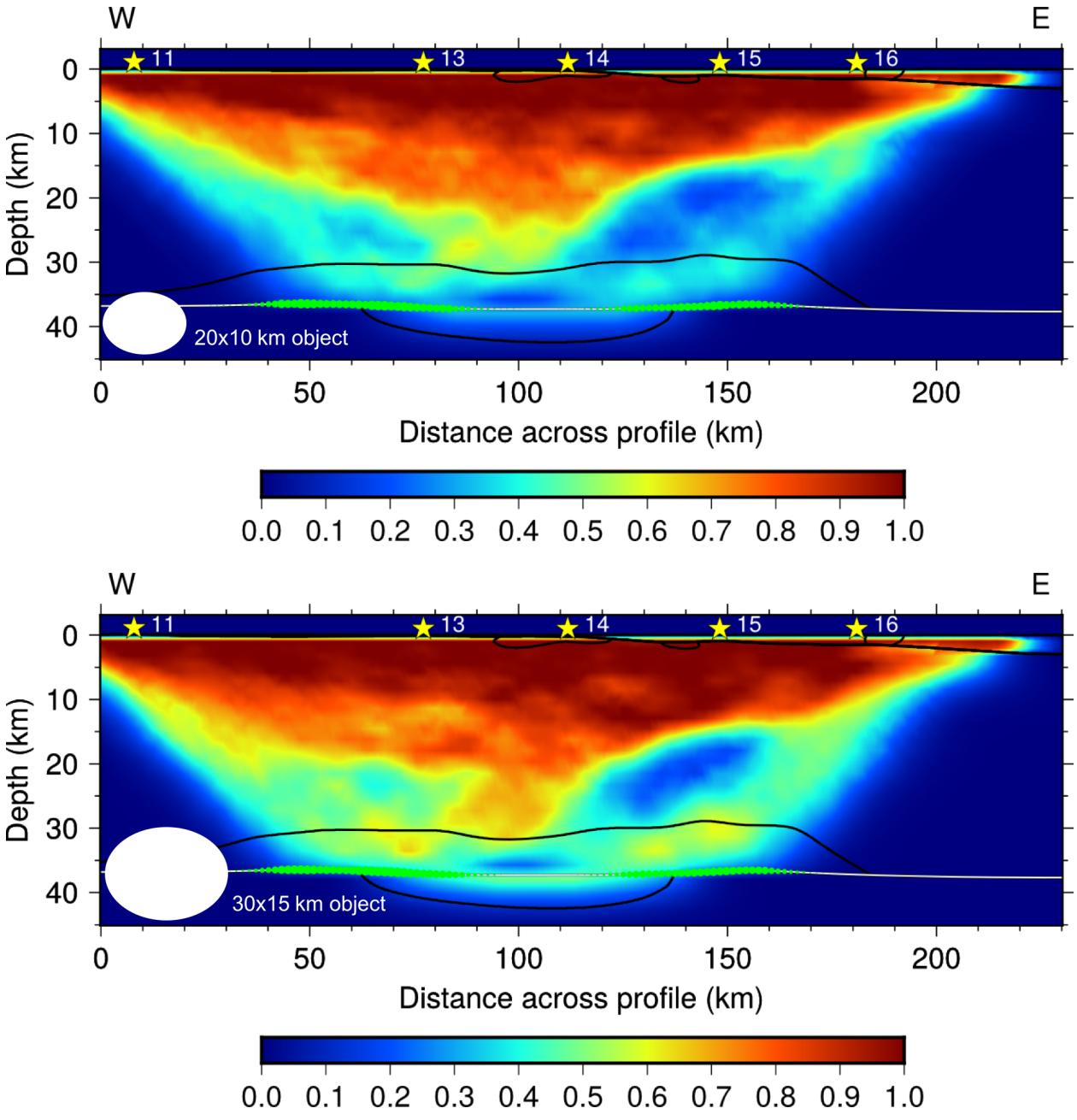
W
E
11
13
14
15
16
Depth (km)
0
10
20
30
40
20x10 km object
0
50
100
150
200
Distance across profile (km)
0.0 0.1 0.2 0.3 0.4 0.5 0.6 0.7 0.8 0.9 1.0
W
E
11
13
14
15
16
Depth (km)
0
10
20
30
40
30x15 km object
0
50
100
150
200
Distance across profile (km)
0.0 0.1 0.2 0.3 0.4 0.5 0.6 0.7 0.8 0.9 1.0

11.2 Line 2

Resolution of seismic velocity variations and layer boundary depth at varying scales for Line 2. Stars represent shot points and numbers. (Top) Elliptical model features that measure 10x5 km are well resolved in the upper 10 km of the crust across the profile, with moderate resolution below 15 km in the middle of the profile and poor resolution below 10 km on the sides and 30 km in the middle of the model. (Middle) Elliptical model features that measure 20x10 km are well resolved in the upper 10 km of the crust across the profile, with moderate resolution below 20 km in the middle of the profile. (Bottom) Elliptical model features that measure 30x15 km are well resolved in throughout the model, except at ~35 km near the middle of the model, around 20 km to 30 km in the western portion of the model, and 15 km to 25 km in the eastern portion of the model.

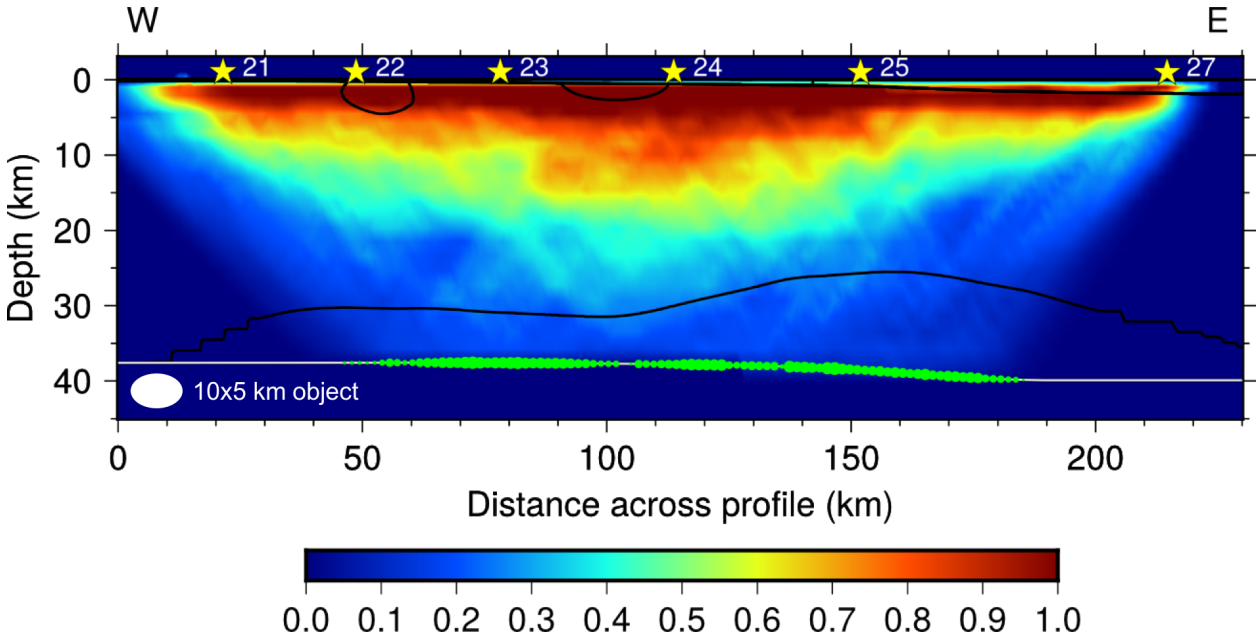

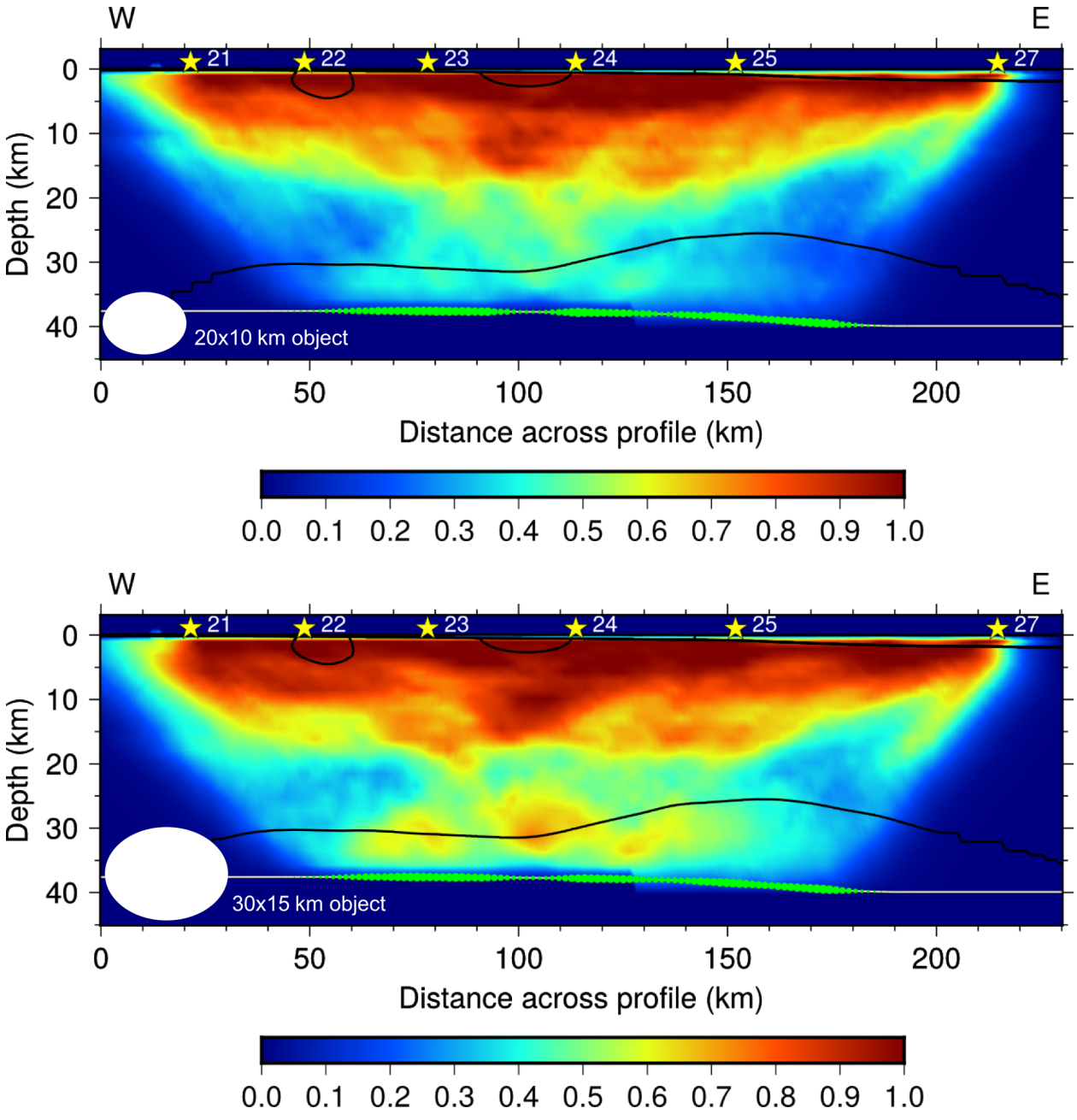
W
E
21
22
23
24
25
27
0
10
20
30
40
Depth (km)
20x10 km object
0
50
100
150
200
Distance across profile (km)
0.0 0.1 0.2 0.3 0.4 0.5 0.6 0.7 0.8 0.9 1.0
W
E
21
22
23
24
25
27
0
10
20
30
40
Depth (km)
30x15 km object
0
50
100
150
200
Distance across profile (km)
0.0 0.1 0.2 0.3 0.4 0.5 0.6 0.7 0.8 0.9 1.0